

THERMODYNAMICS AND DYNAMICS OF SELF
ASSEMBLED MESOPHASES OF MULTI-FACETED
AND MULTI-LOBED PARTICLES

A Dissertation

Presented to the Faculty of the Graduate School

of Cornell University

in Partial Fulfillment of the Requirements for the Degree of

Doctor of Philosophy

by

Umang Agarwal

May 2012

© 2012 Umang Agarwal
ALL RIGHTS RESERVED

THERMODYNAMICS AND DYNAMICS OF SELF ASSEMBLED
MESOPHASES OF MULTI-FACETED AND MULTI-LOBED PARTICLES

Umang Agarwal, Ph.D.

Cornell University 2012

This work aims at developing a fundamental understanding of how shape of nano/micro-particles affects their thermodynamic phase behavior and dynamic properties. Anisotropic interaction fields encoded in nanoparticles of non-spherical shape can drive their assembly into many complex, ordered or partially ordered structures ("mesophases"). Some of these self-assembled 'phases' are highly desirable for their distinctive electronic, physical and optical properties and are very sensitive to the entropic interactions of their building blocks and other external driving fields. To understand the basic principles controlling formation of these assemblies, we performed systematic simulation studies to explore the effect of 'shape' or excluded volume interactions on the equilibrium mesophase behavior and on selected non-equilibrium mechanical properties of these systems. Monte Carlo simulations performed on a class of space-filling polyhedral shapes predict formation of various novel liquid-crystalline (LC) and plastic-crystalline phases. By correlating these results with particle anisotropy and rotational symmetry, guidelines for predicting phase behaviour of polyhedral particles are proposed. The effect of quenched size polydispersity on the phase behavior of polyhedral particles is also elucidated by carrying out extensive compression Monte Carlo simulation for polydisperse systems of three distinct shapes. High polydispersities are found to lead to an increased stability of mesophases and the formation of jammed states at high densities. To

investigate the effect of anisotropy on dynamics, we performed non-equilibrium molecular dynamics simulations to chart the yielding and shear induced melting behavior of mixed crystalline assemblies of spherical and dimer-shaped particles. Important differences in microstructure, dislocations and stress relaxation behavior emerge with introduction of this shape perturbation (dimer particles), which manifests as non-monotonic yield stress values and a two-stage shear melting behavior. Altogether this work makes some inroads toward a general understanding and taxonomy of the effect of particle shape on the thermophysical properties of colloidal assemblies.

BIOGRAPHICAL SKETCH

Umang Agarwal was born in Bareilly, Uttar Pradesh in India. He went to elementary, middle and high school in this city and moved to Kanpur for his undergraduate education in July of 2003. In 2007, he completed his Bachelor's degree in Chemical Engineering from Indian Institute of Technology, Kanpur. During his stay at Kanpur, he pursued some projects in mathematical modeling and simulations, which got him interested in the field of mathematical modeling. In August of 2007, he joined the Department of Chemical Engineering at Cornell University, Ithaca, to pursue graduate studies in this field.

To my parents, friends and loved ones for their utmost support throughout my
academic career.

ACKNOWLEDGEMENTS

I would sincerely like to thank my advisor, Professor Fernando A. Escobedo, for his persistent support and guidance during my stay at Cornell for the past five years. The completion of this work as well would not be possible without the valuable discussions with him, his encouragement and optimism. I am indebted to him for all the time he devoted to the discussions with me that has helped me develop academically and will help me greatly in my future career. I would also like to sincerely thank Professor Lynden Archer and Professor Chekesha Liddell Watson for their roles on my Special Committee. I am also indebted to a very helpful and friendly research group which helped me throughout with the work and made the stay very enjoyable. I would like to thank various staff members in the department Shelby, Breana, Olivia, Carol for helping me out with all the small and big issues, and Steve Thompson for managing the computational resources. I acknowledge financial support from U.S. National Science Foundation Grant No. CBET 1033349 , KAUST-CU center and by the U.S. Department of Energy, Office of Basic Energy Sciences, Division of Materials Sciences and Engineering under award Grant No. ER46517.

TABLE OF CONTENTS

Biographical Sketch	iii
Dedication	iv
Acknowledgements	v
Table of Contents	vi
List of Figures	viii
1 Mesophase behaviour of polyhedral particles	1
1.1 Abstract	1
1.2 Methods	22
Bibliography	25
2 Mesophase behaviour of polyhedral particles: Tools and Additional Results	28
2.1 Potential of mean force	28
2.2 Translational order parameters	30
2.2.1 Bond-order orientational parameters	30
2.2.2 Local bond-order parameters	31
2.2.3 Translational mobility coefficients	33
2.3 Orientational order parameters	33
2.3.1 Cubatic order parameters	35
2.3.2 Rotational auto-correlation function	37
2.4 Distribution Functions	40
2.4.1 Particle distribution functions	40
2.4.2 Orientational distribution function	42
2.4.3 Orientational correlation function	43
2.5 Direct coexistence simulation of triangular prisms	45
2.6 Hysteresis in equations of state	48
2.7 Case Study A: Hexagonal Prisms of different aspect ratios	50
2.7.1 Aspect ratio 0.5	50
2.7.2 Aspect ratio 2.0	54
2.8 Case Study B: Triangular Prisms of different aspect ratios	56
2.8.1 Aspect ratio 0.5	56
2.8.2 Aspect ratio 2.0	56
Bibliography	57
3 Effect of quenched size polydispersity on the phase behavior of polyhedral particles	58
3.1 Abstract	58
3.2 Introduction	60
3.3 Methods	64
3.4 Results and Discussions	70

3.5	Conclusions	86
3.6	Acknowledgement	89
3.7	Supplementary Information	90
	Bibliography	96
4	Yielding and shear induced melting of 2D mixed crystals of spheres and dimers	99
4.1	Abstract	99
4.2	Introduction	100
4.3	Model and Simulation Methods	101
4.4	Results	105
4.5	Conclusions	118
	Bibliography	120

LIST OF FIGURES

1.1	Effect of shape anisotropy on hard-particle mesophase order. (a) Possible states at intermediate volume fractions; partial loss of order in particular degrees of freedom in SFP crystals can lead to mesophases. (b) Approximate roadmap for phase behaviour of hard polyhedral shapes. LC= liquid crystal, AR = aspect ratio; the phases shown in red are expected to be stable for prisms of similar AR.	4
1.2	Summary of equilibrium structures for different SFPs. Snapshots for the various mesophases, and crystalline states for the six shapes (a) Truncated Octahedrons, (b) Rhombic Dodecahedron, (c) Hexagonal Prisms, (d) Cubes, (e) Triangular Prisms and (f) Gyrobifastigiums, obtained from expansion and coexistence runs. The states are depicted from left to right in increasing order of volume fractions and the six shapes are arranged from top to bottom in increasing order of anisotropy. Particle colours are used for visual effect and to detect mixing of the initial crystal layers.	7
1.3	Phase behaviour of shapes with low anisotropy and high symmetry. Translational (Q_4 and Q_6) and orientational ($\langle \overline{P}_4 \rangle$) order parameters (top) and equation of state (bottom) with marked phase boundaries for truncated octahedrons (TO) and rhombic dodecahedrons (RD).	9
1.4	Phase and structural behaviour of hexagonal prisms. Translational mobility coefficient D , orientational order parameters I_2 and I_4 (top) and equation of state (bottom) with marked phase boundaries for hexagonal prisms.	12
1.5	Phase and structural behaviour for cubes. Translational mobility coefficient D , orientational order parameter $\langle \overline{P}_4 \rangle$ (top) and equation of state (bottom) with marked phase boundaries for cubes.	15
1.6	Phase behaviour for shapes with high anisotropy and low symmetry. a) Equation of state curves for triangular prisms (TP) and gyrobifastigium (GB); (b) Illustration of the geometrical calculations for the degree of expansion required for regular packing to accommodate rotation of a particle (a TP in this case) at its centre. Polygon with dotted lines correspond to the original orientation of the central particle.	18
2.1	Potential of mean force for the SFPs considered in this work.	29
2.2	Probability distribution of locally averaged bond orientational order parameters (q_4 and q_6) for the FCC, BCC and HCP crystals, liquid state of hard spheres and for rotator phase of truncated octahedrons at $\phi = 0.594$	32

2.3	Rotational autocorrelation function against number of MC cycles for various concentrations (ϕ) around the rotator-crystal transition in a) truncated octahedrons and b) rhombic dodecahedrons. Some fitted exponential decay curves are shown as dashed lines with their corresponding values of the time constants for decay (τ).	34
2.4	(a) Particle distribution function and (b) Orientational distribution function for RPS phase of hexagonal prisms at $\phi = 0.619$. The unit vectors along blue particle axes are used to plot the orientational distribution function.	36
2.5	Particle distribution functions for cubatic-like phases of (a) hexagonal prisms and (b) cubes.	38
2.6	Results for triangular prisms:(a) Orientational distribution with respect to the transverse axes at $\phi = 0.59$. The unit vectors along blue particle axes are used to plot the orientational distribution function.(b) Number density profile against the z-axis of the simulation box, in units of height of the prism (Inset: Evolution of the total volume fraction) of the inhomogeneous system comprised of coexisting crystalline and isotropic phases of triangular prisms, obtained from direct NpT simulations at different pressure values.	39
2.7	Orientational correlation functions at various volume fractions for (a) truncated octahedrons and (b) rhombic dodecahedrons.	41
2.8	Complete equations of state from compression and expansion runs for (a) truncated octahedrons and (b) cubes.	44
2.9	Results for hexagonal prisms of aspect ratio 0.5: (a) Snapshot of the columnar phase at $\phi=0.57$: front view (left) and top view (right) (b) Equation of state (bottom frame) obtained from expansion and compression NpT runs and translational mobility coefficients (top frame) along and perpendicular to the columnar phase director (particle axes) (c) Particle distribution function for the columnar phase at $\phi=0.57$	47
2.10	Results for hexagonal prisms of aspect ratio 2.0: (a) Snapshot of the smectic-like phase at $\phi=0.59$: front view (left) and top view (right); (b) Equation of state obtained from expansion and compression NpT runs; (c) Particle distribution function for the smectic phase at $\phi=0.59$	49
2.11	Snapshots of the metastable cubatic-like phase observed in compression runs of hexagonal prisms of aspect ratio (a) 0.5 and (b) 2.0, showing stacks of particles on top of each other for the 0.5 aspect ratio and sideways for the 2.0 aspect ratio. (c) and (d) Snapshots obtained from longer runs showing gradual development of more ordered but still defective mesophases.	51

2.12	Results for triangular prisms of aspect ratio 0.5: (a) Snapshot of the columnar phase at $\phi=0.56$: front view (left) and top view (right) (b) Equation of state (bottom frame) obtained from expansion and compression NpT runs and translational mobility coefficients (top frame) along and perpendicular to the columnar phase director (particle axes) (c) Particle distribution function for the columnar phase at $\phi=0.56$	53
2.13	Results for triangular prisms of aspect ratio 2.0: (a) Snapshot of the smectic-like phase at $\phi=0.59$: front view (left) and top view (right) (b) Equation of state obtained from expansion and compression NpT runs (c) Particle distribution function for the smectic phase at $\phi=0.59$	55
3.1	Nanocrystal shapes synthesized at different growth stages of the modified polyol process. The snapshots show the simulated mesophases at the order-disorder transition point (particle colors are used to highlight layering behavior).	62
3.2	Different translational and orientational order parameters for assemblies of 8000 cubes at various volume fractions (obtained by sampling over 200 independent configurations from constant density simulations). Dashed lines enclose region of putative cubatic phase character.	71
3.3	Polydisperse cubes for $0 \leq \delta \leq 0.3$. Top: Mobility coefficients (D) and cubatic orientational order parameter $\langle P_4 \rangle$ vs. pressure. Middle: Equation of state curves showing overlap and no first-order transition density gap for $\delta \geq 0.18$. Bottom: Translational ($\langle G_{global} \rangle$) and orientational ($\langle P_4 \rangle$) order parameters vs. volume fraction ϕ ; the peak in $\langle G_{global} \rangle$ around $\phi = 0.6$ indicates conditions that favor structures with cubic symmetry.	74
3.4	Snapshots for cubes at various pressure state points (around the order-disorder transition points, which is significantly different for higher δ systems and higher pressures) for $\delta = 0.10, 0.16, 0.18$ and 0.20 . The particles are color coded from red to green, depending on their local bond orientational order parameter value $\bar{q}_4(i)$	77
3.5	Polydisperse truncated octahedrons with $0 \leq \delta \leq 0.3$. Top: Mobility coefficients (D) and global bond orientational order parameter Q_6 plotted against pressure. Bottom: Equation of state curves showing overlap and no first order transition density gap for $\delta \geq 0.14$	80

3.6	Equilibrated snapshots for truncated octahedrons at various pressure state points (around the order-disorder transition and higher pressures) for $\delta = 0.08, 0.12, 0.14$ and 0.20 . The particles are color coded from red to green, depending on their local bond orientational order parameter value $\bar{q}_4(i)$	81
3.7	Polydisperse cuboctahedrons for $0 \leq \delta \leq 0.20$. Top: Mobility coefficients (D) and global bond orientational order parameter Q_6 plotted against pressure for $\delta = 0.0$ (reference lines), 0.06 and 0.12 . Bottom: Equation of state curves showing overlap and have no first order transition density gap for $\delta \geq 0.08$	84
3.8	Snapshots for cuboctahedrons at various pressure state points (around the order-disorder transition and higher pressures) for a) $\delta = 0.06$ and b) 0.08 . The particles are color coded from red to green, depending on their local bond orientational order parameter value $\bar{q}_4(i)$	85
3.9	Phase behavior of monodisperse truncated cubes. Top: Orientational order parameter (P_4) and snapshots illustrating the presence of a cubatic-like LC phase in between the crystal and isotropic phases. Bottom: Equation of state from expansion and compression runs.	90
3.10	Phase behavior of monodisperse cuboctahedrons. Top: Translational (Q_4 and Q_6) and orientational (P_4) order parameters from expansion runs. Bottom: Equation of state from expansion and compression runs, showing two first-order transitions separating the crystalline, rotator and isotropic phases.	91
3.11	Equation of states from expansion and compression for polydisperse cubes for $\delta \sim 0.20 (> \delta_t)$. The curves overlap each other pretty closely indicating absence of any hysteresis in the translational jamming behavior.	92
3.12	Equation of state curves for polydisperse cubes with $\delta \sim 0.10$ from different initial Gaussian size distribution configurations. The close agreement among curves indicates that the system size used (1728 particles) is sufficiently large to properly sample polydispersity effects.	93

3.13	<p>Orientational distribution functions for polydisperse (a) truncated octahedrons and (b) cuboctahedrons at different pressures (P^*) and volume fractions (ϕ); the dots show the orientation of the unit vectors perpendicular to the square facets so that the most clustered they are the highest the extent of orientational order. In all cases, systems with higher polydispersity (δ) have less orientational order for either the same pressure or the same volume fraction. As an example, for the truncated octahedrons a similar rotator-like order occurs for $\{\delta, P^*, \phi\} = \{0.06, 3.4, 0.58\}, \{0.12, 4.5, 0.62\},$ and $\{0.14, 11.2, 0.69\}$. Note that the approximate range of occurrence of the rotator phase for the monodisperse systems is $P^* = 2.5-4.5, \phi = 0.52-0.70$ for truncated octahedrons and $P^*=4.0-5.4, \phi = 0.5-0.58$ for cuboctahedrons. . . .</p>	94
3.14	<p>Bond orientational order diagrams for monodisperse ($\delta = 0.0$) and polydisperse ($\delta = 0.02, 0.04$ and 0.06) cuboctahedrons. The ordered states have distorted BCC symmetry, while on reducing pressure the peaks become more diffuse due to higher vibrational freedom at these lower densities. On increasing polydispersity, bond orientational order decreases; i.e., it is lost for $\delta = 0.04$ and 0.06 at $P^* = 4.53$ and the peaks are more diffuse at the higher pressures.</p>	95
4.1	<p>a) Average yield stress values (with error bars) for different dimer compositions of the mixed crystals. The inset shows the instantaneous shear rate values for simulations at different constant stresses in the system with dimer fraction = 0.08. The minimum stress value which leads to a non-zero average shear rate is marked as the yield stress of the crystal (1.71 in the inset). b) Stress vs. strain rate for different dimer composition mixed crystals. The agreement between the yield stress values and the plateau of each stress-strain rate curve obtained from independent simulations is shown for two different compositions (horizontal dashed lines across frames 'a' and 'b').</p>	106
4.2	<p>The average number of dislocation/disclination sites and vacancies in the sheared crystals at a constant shear rate of 0.005 for different dimer compositions. The average was obtained from 1000 independent configurations for each composition.</p>	107

4.3	a) Variance of the global bond-orientational ψ_6 order parameters obtained from 1000 configurations against shear rate for 5 different mixed crystal compositions (lines are drawn to guide the eye). b) The bond-orientational pair correlation functions $g_6(r)$ for different shear rates for a mixed crystal with dimer fraction of 0.7. The plots also mark the different shear rate regimes for solid, hexatic-like, and liquid phases (which exhibit qualitative differences in variance values and decay behavior of $g_6(r)$). . . .	110
4.4	ψ_6 color maps (left) and static structure factor plots (right) for the three distinct phases of a mixed crystal with a dimer fraction of 0.7. a) Solid phase at $\dot{\gamma} = 0.002$, b) hexatic-like phase at $\dot{\gamma} = 0.016$, and c) liquid phase at $\dot{\gamma} = 0.04$. The legend on top indicates the color ascribed to the limiting local bond orientational vectors; color maps are obtained for configurations obtained at a regular interval of 103 time units ($= 10^6$ time steps).	113
4.5	Instantaneous stress and variance in the local bond orientational order parameter plotted against time for the solid phase (left) at a shear rate of 0.004 and the hexatic-like phase (right) at a shear rate of 0.02, for a mixed crystal system with dimer fraction of 0.5. The ψ_6 color maps for the configurations at the crest and troughs of the stress profile are shown on top, along with their orientation vectors relative to the strain direction.	117

CHAPTER 1
MESOPHASE BEHAVIOUR OF POLYHEDRAL PARTICLES

1.1 Abstract

Translational and orientational excluded-volume fields encoded in particles with anisotropic shapes can lead to purely entropy-driven assembly of morphologies with specific order and symmetry. To elucidate this complex correlation, we performed detailed Monte Carlo simulations of six convex space-filling polyhedrons, namely, truncated octahedrons, rhombic dodecahedrons, hexagonal prisms, cubes, gyrobifastigiums, and triangular prisms. Simulations predict the formation of various novel liquid-crystalline and plastic-crystalline phases at intermediate volume fractions. By correlating these findings with particle anisotropy and rotational symmetry, simple guidelines for predicting phase behaviour of polyhedral particles are proposed: high rotational symmetry is in general conducive to mesophase formation, with low anisotropy favouring plastic-solid behaviour and intermediate anisotropy (or high uniaxial anisotropy) favouring liquid crystalline behaviour. It is also found that dynamical disorder is crucial in defining mesophase behaviour, and that the apparent kinetic barrier for the liquid-mesophase transition is much lower for liquid crystals (orientational order) than for plastic solids (translational order).

Currently a major focus in material science is to engineer particles with anisotropic shapes and interaction fields which can be self-assembled into target complex structures [1],[2]. Assemblies of anisotropic particles undergo order-disorder transitions involving changes in both translational and orientational degrees of freedom and can lead to phases with partial structural order or mesophases [3], [4]. These ordered assemblies have distinctive electronic, optical, and dynamical properties [4],[5] and are highly desirable for fabrication of advanced electronic, photonic, and rheological devices [6],[7]. Although numerous theoretical [8]-[13] and experimental studies [14],[15] on mesophase behaviour of particles with anisotropic shapes have been reported, a roadmap marking out the most probable mesophases that could be formed by constituent particles with particular geometrical features is still incomplete. Exploring such relations will translate into a deeper understanding of the phase behaviour of colloidal systems with different particle shapes; e.g., Jiao et al.[16] reported that unlike ellipsoids, convex superballs can be optimally packed in dense Bravais lattices because they are less symmetric but more isotropic than the former. Similarly, Torquato et al.[17] recently conjectured that amongst all Platonic and Archimedean solids, only those having central symmetry can pack into Bravais lattices.

The present study focuses on an important and well defined set of shapes, viz., regular space-filling polyhedrons (SFPs) [18] which has only 5 convex members, namely: truncated octahedron, hexagonal prism, cube, triangular prism, and gyrobifastigium. Note that while non-SFPs (like tetrahedra) may have a non-trivial solid ordering and densest packing [19],[20], SFPs have the advantage of always having a priori known, perfect crystalline order. The key question this work addresses is depicted in Fig. 1.1a: how is the SFP solid order

lost as the concentration decreases? Rather than losing all order at once (in a crystal-to-isotropic transition), we hypothesized that disordering would likely happen in stages, giving rise to meso-phases where, e.g., only orientational order is lost (as in plastic or rotator crystals) or just positional order is lost (as in liquid crystals). More than one intermediate mesophase could also be observed. Note also that mesophases are expected to lower the isotropic-to-crystal barrier and hence serve as conduits that catalyze the assembly of crystalline order from isotropic states. An approximate roadmap illustrating the various possibilities is presented in Fig. 1.1b, which will be discussed in full detail later in the article. Briefly, we identified two key parameters, asphericity [17] of the particles (measure of anisotropy) and orientational symmetry [22],[23] as global descriptors of these particle fields, and show that their relative values are good indicators to predict mesophase behaviour.

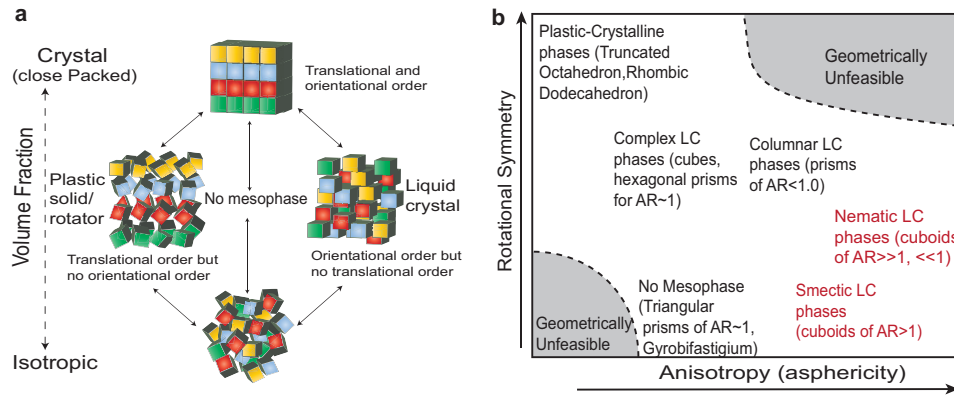


Figure 1.1: Effect of shape anisotropy on hard-particle mesophase order. (a) Possible states at intermediate volume fractions; partial loss of order in particular degrees of freedom in SFP crystals can lead to mesophases. (b) Approximate roadmap for phase behaviour of hard polyhedral shapes. LC= liquid crystal, AR = aspect ratio; the phases shown in red are expected to be stable for prisms of similar AR.

The six shapes used in this study are cubes (Platonic solid), truncated octahedrons TO (Archimedean solid), rhombic dodecahedrons RD (Catalan Solid), gyrobifastigiums GB (Johnson solid), hexagonal prisms HP and triangular prisms TP (prisms and antiprisms). The aspect ratio ($= \frac{a}{b}$) of a prism is defined as the ratio of its height (a) to twice the inradius of its polygonal face (b). The aspect ratio for HP and TP was set to 1 for which at close packing, the nearest neighbors of a particle have equal lattice vectors in all three directions. Moreover HP and TP of aspect ratio $\frac{1}{2}$ and 2 were also studied and the results presented as case studies A and B in the SI. Our model particles resemble the various inorganic and organic multi-faceted nano-colloidal particles that have been synthesized recently[24]-[27]. The anisotropy is quantified using the asphericity values (ratio of the circumradius to the inradius) while the symmetry of the shapes is estimated by using the order of direct symmetry and a continuous parameter[23]

$$q = 1 - \frac{(\sum_{i < j} (\lambda_i^2 - \lambda_j^2))^2}{(\sum_i (\lambda_i^2))^2} \quad (1.1)$$

that combines the eigen values (invariants) λ_i of the particle inertia tensor I_{ij} . The asphericity values are 1.291, 1.414, 1.528, 1.732, 2.236 and 2.309 for TO, RD, HP, cubes, TP, and GB, respectively. The order of direct symmetry[22] (number of distinct rotations reproducing the same orientation) is 24 for TO, RD, and cubes, 12 for HP, 6 for TP, and 3 for GB; the continuous symmetry parameter[23] q is 1.000 for TO, RD, and cubes, 0.992 for HP, 0.967 for TP and 0.897 for GB. Clearly, the order of direct symmetry and the q parameter rank the symmetry of the shapes in the same order but the latter is a more robust descriptor as small perturbations in particle geometry do not lead to abrupt changes in its value (e.g., for a distorted cube with one side 1% larger than the others, the q value is

decreased by less than 0.01% from the ideal value).

Extensive expansion and compression NpT MC runs for truncated octahedrons (TOs) and rhombic dodecahedrons (RDs) indicate the presence of a plastic crystalline mesophase for volume fractions in between the crystalline and isotropic phase regimes. The crystalline phases, which have a BCC structure for TO and FCC structure for RD (Fig. 1.2a and 1.2b), undergo continuous transitions to plastic crystalline (rotator) phases, which in turn melt into isotropic phases via first-order transitions. In the rotator phases (shown in Fig. 1.2a and 1.2b), the positional order is maintained but the short-ranged anisotropic orientation allows particles to rotate around their lattice positions.

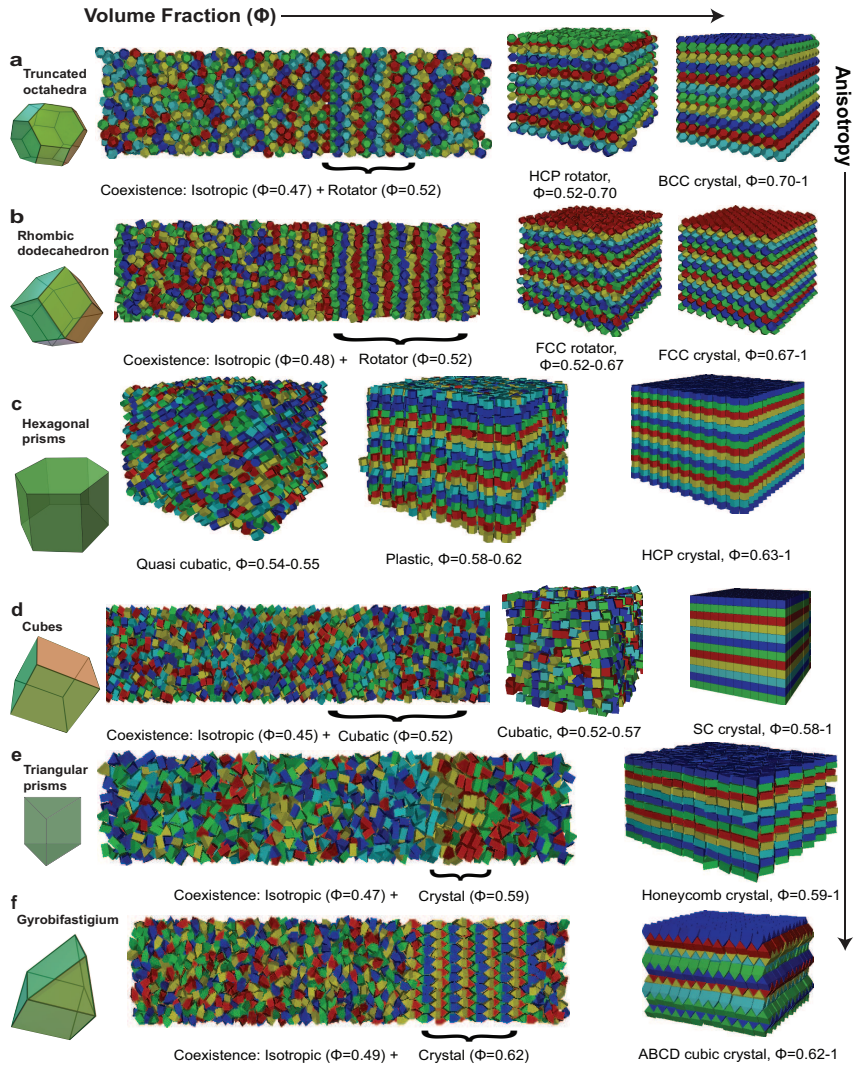


Figure 1.2: Summary of equilibrium structures for different SFPs. Snapshots for the various mesophases, and crystalline states for the six shapes (a) Truncated Octahedrons, (b) Rhombic Dodecahedron, (c) Hexagonal Prisms, (d) Cubes, (e) Triangular Prisms and (f) Gyrobifastigiums, obtained from expansion and coexistence runs. The states are depicted from left to right in increasing order of volume fractions and the six shapes are arranged from top to bottom in increasing order of anisotropy. Particle colours are used for visual effect and to detect mixing of the initial crystal layers.

The presence of appreciable hysteresis in compression and expansion runs precludes pinpointing therefrom the coexistence points for the isotropic-rotator phase transitions. Hence, we carried out additional direct interfacial NpT simulations (details in Methods) which yield estimates of the coexistence densities as $\phi_{rotator}=0.52$ and $\phi_{isotropic}=0.47$ for TO and $\phi_{rotator}=0.52$ and $\phi_{isotropic}=0.48$ for RD. Using these values we plotted the equations of state shown in Fig. 1.3 using only the expansion run results for the crystal and rotator phase branches, and the compression run results for the isotropic phase branches. To identify the boundary for the rotator-crystal phase transition we devised an autocorrelation function for the orientation vectors of particles (details in Sec. 3.2 of *SI*), whose decay over simulation time (while using pseudo-dynamic MC moves) indicates loss of orientational order. The density at which this autocorrelation function starts decaying exponentially (as opposed to linearly, for higher densities) is marked as the approximate boundary for crystal-rotator transition, establishing $0.52 < \phi < 0.70$ and $0.52 < \phi < 0.68$ as the ranges for rotator phase stability for TO and RD, respectively.

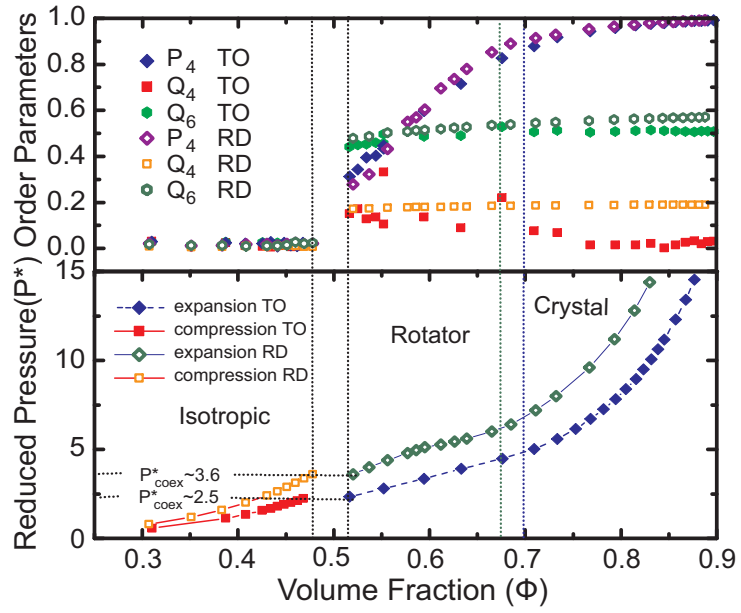


Figure 1.3: Phase behaviour of shapes with low anisotropy and high symmetry. Translational (Q_4 and Q_6) and orientational ($\langle \overline{P_4} \rangle$) order parameters (top) and equation of state (bottom) with marked phase boundaries for truncated octahedrons (TO) and rhombic dodecahedrons (RD).

To further characterize the structure of various phases, the orientational order in the system was measured using the cubatic order parameter $\langle \overline{P_4} \rangle$ [13], while translational order was assessed via the bond-order orientational parameters Q_4 and Q_6 [27] (for ideal BCC packing $Q_4=0.036$ and $Q_6=0.511$, for ideal FCC packing $Q_4=0.191$ and $Q_6=0.575$). The plot in Fig. 1.3 suggests that while there is low orientational order in states between $\phi \approx 0.52$ and $\phi \approx 0.70$; the translational order is still maintained (high values of Q_6). For TO, the slightly-off Q_4 values in this region suggests a disturbance of BCC order. This supports the idea that a reduced orientational entropic bonding field imparts sphere-like behaviour to the particles, whereby they maximize their packing entropy by reorganizing in structures akin to a HCP (ideal $Q_4 = 0.1$) or FCC (ideal $Q_4 = 0.19$) lattice (more stable for spheres[28]). To elucidate the structure of this intermediate mesophase, we followed Lechner et al.[29] to obtain the distribution of averaged local bond order parameters $\overline{q_4}$ and $\overline{q_6}$ for various reference structures (BCC, FCC, HCP crystal lattices and liquid phase) and for the rotator structure obtained at $\phi = 0.594$ (details in Sec. 2.2 of *SI*). The fractions of each of these reference structures[30] in the rotator phase of TO were found to be $f_{bcc} = 0.001$, $f_{fcc} = 0.140$, $f_{hcp} = 0.859$ and $f_{liq} = 0$, confirming the reorganization of the BCC structure. The snapshots of Fig. 1.2a and 1.2b show that the colours ascribed to different layers of the original BCC and FCC structures remain unperturbed for the rotator phases, illustrating preservation of translational order.

Simulations for hexagonal prisms (HPs) show existence of two different mesophases, a high density restricted plastic solid (RPS) and a cubatic-like liquid crystalline phase, in between the HCP crystal and the isotropic phase. The hysteresis effects across the transition points between expansion and compression runs in this system are rather small, hence coexistence densities for the

cubic to isotropic transition were estimated straightforwardly as $\phi_{cubic} = 0.54$ and $\phi_{isotropic} = 0.49$. The RPS phase is similar to the intermediate phase that Blaak and Frenkel[31] obtained for a system of hard cylinders, in which particles are either oriented along the director or are rotated in a plane normal to the director along one of the four-fold degenerate orientations (Fig. 1.2c). Of course, HP (and n-gonal prisms with $n > 6$) are expected to approach the behaviour of hard cylinders of comparable aspect ratio at low-to-intermediate concentrations. The RPS phase has high translational order (solid-like) and discrete (six-fold) orientational disorder (or restricted' plastic character). On further expansion a cubic-like phase is observed for a very narrow range of densities. While this phase also has a moderate amount of layering (as shown by the particle distribution functions shown in Fig. 2.5a), the particles have high translational mobility as indicated by the intermingling of their colours (assigned to layers in the original crystal, see Fig. 1.2c) and the moderate values of translational mobility coefficients in Fig. 1.4. The cubic phase is only observed when using very small pressure changes in compression and expansion runs, which suggests that it could be a metastable intermediate state between the crystalline and isotropic phases.

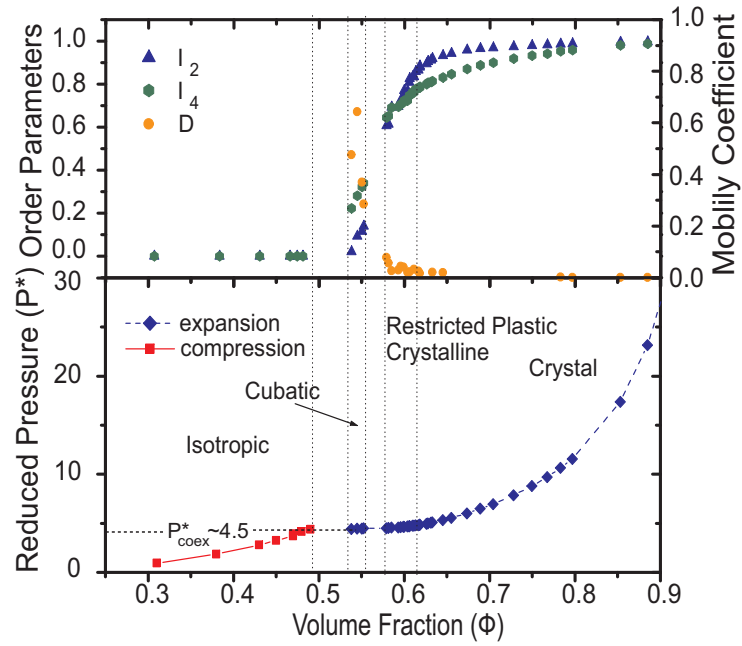


Figure 1.4: Phase and structural behaviour of hexagonal prisms. Translational mobility coefficient D , orientational order parameters I_2 and I_4 (top) and equation of state (bottom) with marked phase boundaries for hexagonal prisms.

We calculated the translational mobility coefficients (D) and rotationally invariant orientational order parameters I_2 and I_4 [13],[31] (details in *SI*) to mark the approximate boundaries of these transitions. Fig. 1.4 shows the equation of state (obtained by combining the expansion run for the meso- and crystalline phases, and compression run for the liquid phase) and the evolution of I_2 , I_4 , and D with volume fraction. It can be observed that at $\phi = 0.54$ and 0.55 there are two first order transitions in the equation of state as well as transitions in both I_2 and I_4 values, which separate the isotropic, cubatic, and RPS phases. For $0.54 < \phi < 0.55$ the small value of I_2 (≈ 0.1) compared to I_4 (≈ 0.3) is indicative of cubatic-like order; however, the modest I_4 value reveals a somewhat weak orientational alignment. Further, significantly higher values of mobility coefficients compared to those for the RPS phase indicate a dynamical translational disorder in this phase. For the $\phi > 0.62$ region, $I_4 > 0.8$ and $I_2 > 0.9$, reflecting development of perfect alignment between particles and hence a crystalline morphology. For the crossover region of $0.58 < \phi < 0.62$, the values of I_2 and I_4 are intermediate and comparable, and D values correspond to a solid-like phase; this combination of features defines the approximate boundaries for the RPS phase. Note that although cylinders showed a similar RPS phase, they did not exhibit a phase with cubatic order[31] like the HPs. This difference can be attributed to packing entropy; a particle with an orientation perpendicular to its neighbors can pack its flat ends (top and bottom) more efficiently against the side facets of the prisms than against the round surface of cylinders.

Cubes have intermediate amount of anisotropy between HP and TP but the highest orientational symmetry (the same as TO). Cubes show a cubatic mesophase (Fig. 1.2d), which is bounded by a seemingly continuous transition from the simple-cubic crystalline phase (Fig. 1.2d) at higher densities and by a

first-order transition from the isotropic phase at lower densities. The equation of state from expansion and compression runs is shown in Fig. 1.5 with phase boundaries marked by transitions in order parameter values. While cubes and other tetragonal parallelepipeds have already been studied extensively by John and Escobedo[11]-[13], our new analysis reveals (see below) that early observations regarding the structure of the cubatic phase and the location of the cubatic-crystal phase boundary needed to be revisited.

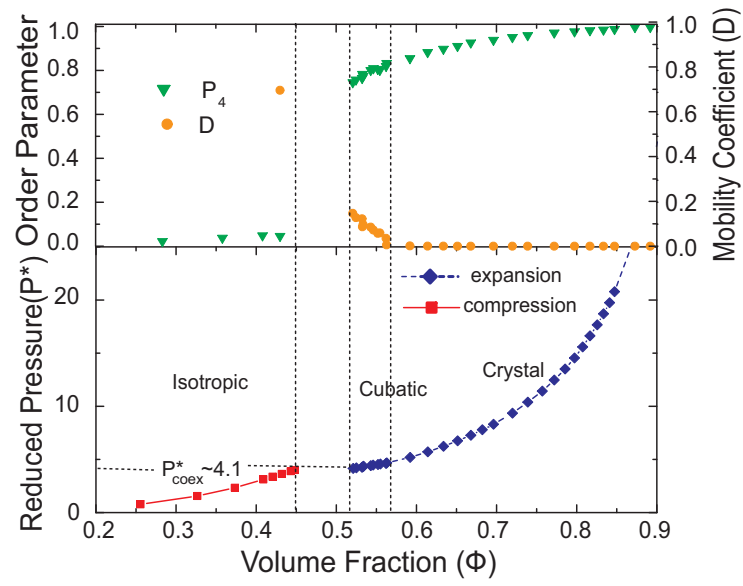


Figure 1.5: Phase and structural behaviour for cubes. Translational mobility coefficient D , orientational order parameter $\langle \overline{P_4} \rangle$ (top) and equation of state (bottom) with marked phase boundaries for cubes.

The cubatic phase is a liquid crystalline phase characterized by high orientational order along all the three possible directors and by no long-range translational order. To mark the approximate boundaries of the two transitions, we measured the cubatic orientational order parameter $\langle \overline{P}_4 \rangle$ and the mobility coefficients D . As observed in Fig. 1.5, the orientational order parameter $\langle \overline{P}_4 \rangle$ shows a transition at $\phi = 0.52$ with high values for $\phi > 0.52$. The D values are significantly higher for $0.52 < \phi < 0.57$ compared to those in the crystalline region. Thus state points with $0.52 < \phi < 0.57$ meet the criteria that define a cubatic phase, with crystalline phase stable for $\phi > 0.58$ and isotropic phase for $\phi < 0.45$. The higher rotational symmetry of cubes relative to hexagonal prisms may have played a role in stabilizing the cubatic phase over a comparatively wider range of densities. In contrast to earlier conjectures[11]-[13], we now find clear evidence of layering in the cubatic phase (also observed in [32]) which becomes visible in our redefined particle distribution functions (see details in SI). While the finite size of our system prevents us from ascertaining the range of such a positional order, the appreciable D values observed at these densities indicates that the system has liquid-like behaviour and there is sufficient translational disorder for layers to rearrange dynamically. This is corroborated by the intermingling of the colours ascribed to different layers of the original crystal in snapshots obtained at these densities (Fig. 1.2d). The interfacial simulations unveiled another peculiar behaviour: the interface between the isotropic and cubatic phases is very difficult to stabilize (leading to more interfaces as the simulation progresses), suggestive of a very low interfacial free energy.

The triangular prisms (TPs) and gyrbfastigiums (GBs) are distinctly anisotropic and the least symmetric shapes in the class of SFPs. Expansion runs for both of these shapes show a direct first-order melting transition and

the absence of any mesophase between the crystalline solid and the isotropic phases. Further, compression runs failed to nucleate defect-free crystalline phases from the isotropic phase due to a large free-energy barrier and non-ergodic configurational sampling. We determined the coexistence conditions for the isotropic-crystal phase transitions from direct simulation of the inhomogeneous systems[33], composed of solid and liquid phases separated by an interface. The equations of state are plotted in Fig. 1.6a, by combining these coexistence density values with the expansion-run branches for $\phi_{solid} > 0.59$ and compression-run branch for $\phi_{liquid} < 0.47$ for TP and $\phi_{solid} > 0.62$ and $\phi_{liquid} < 0.49$ for GB.

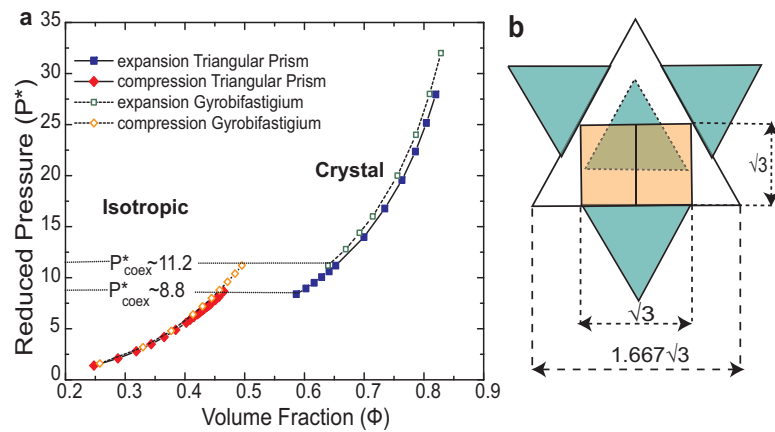


Figure 1.6: Phase behaviour for shapes with high anisotropy and low symmetry. a) Equation of state curves for triangular prisms (TP) and gyrobifastigium (GB); (b) Illustration of the geometrical calculations for the degree of expansion required for regular packing to accommodate rotation of a particle (a TP in this case) at its centre. Polygon with dotted lines correspond to the original orientation of the central particle.

The absence of a mesophase for TPs and GBs can be rationalized as follows. To form a mesophase with translational disorder in even one-direction (columnar-like phase), particles belonging to different columns would need to be able to move along their axes simultaneously. The particle interdigitation in the GB crystal, however, hinders the formation of a mesophase with partial spatial order. In the TP crystal, particles have a very low in-plane symmetry and even slight rotations about any of the axes would cause a large mismatch and disrupt the columnar structure (though it may be attainable for TPs of lower aspect ratios due to reduced losses in packing entropy along the short axis). A rotator mesophase is also precluded because rotation of particles out of the director's plane (layers) is restricted, as revealed by the orientational distribution function of one of the transverse axes for TP (see Fig. 2.6a) near the transition point ($\phi = 0.546$). Due to the low symmetry of TPs and GBs, the packing of the crystals is such that flipping of any particle to a perpendicular plane will require neighboring particles to be separated by a relatively large distance which would cause local melting and promote the isotropization transition, preempting formation of a plastic phase.

To better characterize the particle flip-ability' idea introduced above, we calculated the flip factors (a_{flip}) by which the regular closed packing of each shape has to be expanded to allow one particle at its centre to flip to a perpendicular plane (Fig. 1.6b). These a_{flip} values are 1.0, 1.0, 1.367, 1.0, 1.667 and 1.732 for TO, RD, HP, cubes, TP, and GB respectively. To get an estimate of the propensity for rotation of particles to locally melt the crystal, we used a Voronoi construction to calculate the average distances between neighboring particles (a_{liq}) at their highest-density liquid states. The values for a_{liq} obtained by averaging over several configurations are 1.41, 1.37, 1.46, 1.58, 1.75 and 1.49 for TO, RD, HP,

cubes, TP and GB, respectively. The ratios a_{flip}/a_{liq} are consistent with the observed phase behaviours in that cubes, RD and TO can rotate normal to their lattice plane over a wide range of densities well above their isotropic densities, the range is very narrow for HP and TP, while it is less than 1 for GB precluding out-of-plane rotations for densities above their isotropic density.

We also calculated the expansion factors for free in-plane rotation of these particles (a_{planar}), which should now be indicative of the ease with which particles form mesophases with in-plane rotational disorder like in-plane rotator phases or smectic phases. These a_{planar} factors are 1.118, 1.154, 1.154, 1.414, 2.0 and 1.414 for TO, RD, HP, cubes, TP and GB, respectively. While the interdigitations at close packing of TO (and all Archimedean solids), RD (Catalan solids), and GB (Johnson solids) will prevent formation of liquid crystalline phases with partial spatial order (smectic and columnar phase), we expect and observe (see Ref. [13] and Case Studies A and B in the *SI*) formation of some of these phases for cuboids and HP and TP of certain aspect ratios. These phases arise from the disparity in translational and packing entropy values along different directions and hence they appear only at aspect ratios significantly greater or less than 1. Indeed, as density decreases, the growing amplitude of spatial vibrations in the crystal lattice will tend to destroy first translation order along the axis aligned with the smallest inter-particle spacing (thus producing a liquid crystal); this effect would be stronger for shapes with disparate dimensions (large asphericity).

The emerging picture as charted in Fig. 1.1b is that: (i) shapes with low anisotropy and high orientational symmetry (TO and RD) are more likely to form plastic crystalline phases, (ii) shapes with intermediate anisotropy and high symmetry (cubes and HP of aspect ratio ≈ 1) are more prone to exhibit

complex liquid crystalline mesophases; e.g., a cubatic-like phase, (iii) shapes with high anisotropy and low symmetry (GB and TP of aspect ratio ≈ 1) have no mesophase and show a direct isotropic-crystal phase transition, and (iv) sufficiently oblate prisms exhibit columnar phases while sufficiently prolate prisms can exhibit smectic phases. Additionally, any shape in the limit of aspect ratio tending to zero or infinity are expected to approach the behaviour of disks or long rods which exhibit nematic phases. Other SFPs[34]-[35] and polyhedral particles are expected to conform with these qualitative trends.

Very high hysteresis is observed across the first order transition from the liquid to translationally ordered phases for TO, RD, GB, and TP, while negligible hysteresis is seen for transitions from liquid to orientationally ordered phases for HPs and cubes. This suggests that it may always be easier to nucleate (lower free energy barrier) orientational order than translational order from a liquid phase. Also, when a mesophase occurs, the mesophase-crystal transition appears to be continuous, a rather remarkable result for a cubatic phase. As illustrated by the case of TOs, a rotator phase for any particle with low anisotropy and high rotational symmetry may always have translational order with dominant HCP/FCC symmetry, irrespective of the native densest-packing lattice (Bravais for centrally symmetric polyhedrons[17]). Regarding the cubatic phases observed (for cubes and HP), their significant layering underscores the importance of distinguishing between static vs. dynamic order. Indeed, our calculations of mobility coefficients indicate that “time” or dynamics is a key consideration in characterizing the liquid crystalline character of phases that otherwise possess a significant degree of ‘static’ positional order. While 2D ordered assemblies have been experimentally observed for cubes[36] and HP[37], experimental verification of the various structures predicted in this study is yet

to be achieved.

1.2 Methods

For outlining the phase behaviour for each of the SFP shapes under study, extensive isothermal-isobaric NpT ensemble Monte Carlo simulations were performed. The number of particles used in these simulations depended on the geometry of the packing specific to particle shape, such that a perfect crystal (space filling) configuration can be obtained to start the simulation for expansion runs. To account for finite size effects, we simulated systems of 1024, 2000 and 3456 particles for each of the particle shapes except for cubes for which we used 512, 1000 and 1728 particles and for GB for which we used 2916 particles. The methodology involved equilibrating the system at a particular osmotic pressure P^* using translation, rotation and anisotropic volume moves. The dimensionless osmotic pressure P^* was defined as $P^* = Pa^3/\epsilon$, where a' is the radius of the circumscribing sphere (specific to each particle geometry) and ϵ' is an arbitrary energy parameter (set to 1). We also incorporated flip moves [31], that attempt to rotate a chosen particle to a random orientation in the plane perpendicular to its current orientation. All moves were accepted or rejected according to the Metropolis criterion which in this case involves overlap checks using the separating axes theorem[38].

Expansion/compression runs were performed in a stepwise manner by expanding the perfect solid crystal structure at decreasing/increasing values of pressure. The volume moves were anisotropic to allow the simulation box shape to change for the solid-phase and mesophase branches, while only isotropic

volume moves were allowed at pressures corresponding to the liquid region (to avoid highly distorted box shapes). Each pressure run consisted of 3×10^6 Monte Carlo cycles for both equilibration and production, where each cycle has on average N translational, N rotational, $N/10$ flip, and 1 volume move attempts. Because of the large free energy barriers, nucleation of an ordered phase from an isotropic phase required longer and slower compression runs. Hence, smaller pressure steps size and more numerous MC cycles (up to 2×10^7 MC cycles) were often used. The equilibration of each phase was checked by recording the volume of the simulation box against the number of cycles and by the consistency of various order parameters measured at key state points for configurations periodically saved during the production runs. In case of appreciably hysteresis across a first order transition, direct interfacial *NVT* simulations were carried out to get the coexistence densities of the two phases. The initial configuration for the two-phase interfacial system was built using volume fractions at the transition points obtained from expansion runs (as initial estimates). At the start, the two boxes with perfect crystalline phases are placed next to each other, the second region is further expanded along the z-axis to match the lower density of the liquid region. Following this, the liquid region and solid regions are separately equilibrated using 2×10^7 MC cycles each. The resulting heterogeneous system was then equilibrated with 3×10^7 MC cycles to obtain an equilibrated two-phase state. The coexistence densities are calculated by plotting the particle density along the z axes and using the plateau region of this density profile for the two phases. All phases obtained in this study were further analyzed using various translational and orientational order parameters, mobility coefficients, plots for orientational distribution functions, particle distribution functions, and visual inspection of snapshots at all state points. A detailed ac-

count of these methods is given in *SI* along with some additional plots.

Correspondence and requests for materials should be addressed to F.E.

Acknowledgement

This work was supported by a Department of Energy Basic Energy Science Grant ER46517. This publication is based on work supported in part by award no. KUS-C1-018-02, made by King Abdullah University of Science and Technology (KAUST).

BIBLIOGRAPHY

- [1] Whitesides GM, Boncheva M (2002) Beyond molecules: Self-assembly of mesoscopic and macroscopic components. *Proc Natl Acad Sci* 99:4769-4774.
- [2] Glotzer SG, Solomon MJ (2007) Anisotropy of building blocks and their assembly into complex structures. *Nat Mater* 6:557-562.
- [3] Frenkel D (2002) Soft Condensed Matter. *Physica A* 313:1-31.
- [4] Burda C, Chen X, Narayanan R, El-Sayed M (2005) Chemistry and properties of nanocrystals of different shapes. *Chem Rev* 105:1025-1102.
- [5] Tuteja A, Mackay ME, Narayanan S, Asokan S, Wong MS (2007) Breakdown of the continuum Stokes-Einstein relation for nanoparticle diffusion. *Nano Lett* 7:1276-1281.
- [6] Gudixen MS, Lauhon LJ, Wang J, Smith DC, Lieber CM (2002) Growth of nanowire superlattice structures for nanoscale photonics and electronics. *Nature* 415:617-620.
- [7] Lee YS, Wetzel ED, Wagner NJ (2003) The ballistic impact characteristics of kevlar woven fabrics impregnated with a colloidal shear thickening fluid. *J Mater Sci* 38:2825-2833.
- [8] Veerman JAC, Frenkel D (1992) Phase-behavior of disk-like hard-core mesogens. *Phys Rev A* 45:5632-5648.
- [9] Camp PJ, Allen MP (1997) Phase diagram of the hard biaxial ellipsoid fluid. *J Chem Phys* 106:6681-6689.
- [10] Zhang Z, Tang Z, Kotov NA, Glotzer SC (2007) Simulations and analysis of self-assembly of CdTe nanoparticles into wires and sheets. *Nano Lett* 7:1670-1675.
- [11] John BS, Stroock A, Escobedo FA (2004) Cubatic liquid-crystalline behavior in a system of hard cuboids. *J Chem Phys* 120:9383-9389.
- [12] John BS, Escobedo FS (2005) Phase behavior of colloidal hard tetragonal parallelepipeds (cuboids): A Monte Carlo simulation study. *J Phys Chem B* 109:23008-23015.

- [13] John BS, Escobedo FA (2008) Phase behavior of colloidal hard perfect tetragonal parallelepipeds. *J Chem Phys* 128:044909.
- [14] Yin JS, Wang ZL (1997) Ordered Self-Assembly of Tetrahedral Oxide Nanocrystal. *J Chem Phys* 129:114707.
- [15] Maeda H, Maeda Y (2003) Liquid crystal formation in suspensions of hard rodlike colloidal particles: direct observation of particle arrangement and self-ordering behavior. *Phys Rev Lett* 90:018303.
- [16] Jiao Y, Stillinger FH, Torquato S (2009) Optimal packing of superballs. *Phys Rev E* 79:041309.
- [17] Torquato S, Jiao Y (2009) Dense packings of the platonic and archimedean solids. *Nature* 460:876-879.
- [18] Steinhaus H (1999) *Mathematical Snapshots*. (Oxford University Press, New York).
- [19] Chen E. R., Engel M., Glotzer S. C. (2010) Dense crystalline dimer packings of regular tetrahedral. *Discrete Comput. Geom* 44:253-280.
- [20] Torquato S, Jiao Y (2010) Exact constructions of a family of dense periodic packings of tetrahedral. *Phys. Rev. E* 81, 041310.
- [21] Miller W (1972) *Symmetry Groups and their Applications*. (Academic Press, New York).
- [22] Miller W. L., Bozorgui B., Cacciuto A. (2010) Crystallization of hard aspherical particles. *J. Chem. Phys.* 132, 134901.
- [23] Barnard AS, Lin XM, Curtiss LA (2005) Equilibrium morphology of face-centred cubic gold nanoparticles \approx 3 nm and the shape change induced by temperature. *J Phys Chem B* 109:24465-24472.
- [24] Liu et al. (2006) ZnO hexagonal prisms grown into p-Si(1 1 1) substrate from poly(vinylpyrrolidone) assisted electrochemical assembly. *J Crys Growth* 290:405-409.
- [25] Sun YG, Xia YN (2002) Shape-controlled synthesis of gold and silver nanoparticles. *Science* 298:2176-2179.

- [26] Millstone JE, Hurst SJ, Métraux GS, Cutler JI, Mirkin CA (2009) Colloidal gold and silver triangular nanoprisms. *Small* 5:646-664.
- [27] Steinhardt PJ, Nelson DR, Ronchetti M (1983) Bond-orientational order in liquids and glasses. *Phys Rev B* 28:783-805.
- [28] Mau S-C, Huse DA (1999) Stacking entropy of hard-sphere crystals. *Phys Rev E* 59:4396:4401.
- [29] Lechner W, Dellago C (2008) Accurate determination of crystal structure based on averaged local bond order parameters. *J Chem Phys* 129:114707.
- [30] ten Wolde PR, Ruiz-Montero MJ, Frenkel D (1995) Numerical evidence for bcc ordering at the surface of a critical fcc nucleus. *Phys Rev Lett* 75:2714-2717.
- [31] Blaak R, Frenkel D, Mulder BM (1999) Do cylinders exhibit a cubatic phase? *J Chem Phys* 110:11652-11659.
- [32] Batten R.D., Stillinger F.H., Torquato S. (1999) Phase behavior of colloidal superballs: Shape interpolation from spheres to cubes *Phys. Rev. E* 81, 061105.
- [33] Noya EG, Vega C, Miguel E (2008) Determination of the melting point of hard spheres from direct coexistence simulation methods. *J Chem Phys* 129:114707.
- [34] Inchbald G (1996) Five space-filling polyhedral. *The Mathematical Gazette* 80:466.
- [35] Goldberg M (1976) Several new space-filling polyhedral. *Geometriae Dedicata* 5:517.
- [36] Choi SY, Lee YJ, Park YS, Ha K, Yoon KB (2000) Monolayer assembly of zeolite crystals on glass with fullerene as the covalent linker. *J Am Chem Soc* 122:5201-5209.
- [37] Zhang HT, Wu G, Chen XH (2005) Large-scale synthesis and self-assembly of monodisperse hexagon Cu₂S nanoplates. *Langmuir* 21:4281-4282.
- [38] Golshtein EG, tretyakov NV (1996) Modified Lagrangians and monotone maps in optimization. (Wiley, New York).

CHAPTER 2
MESOPHASE BEHAVIOUR OF POLYHEDRAL PARTICLES: TOOLS AND
ADDITIONAL RESULTS

2.1 Potential of mean force

A complementary metric for the degree of anisotropy, besides asphericity, is the potential of mean force [1] obtained from:

$$PMF(r) = -\beta^{-1} \ln(\langle e^{-\beta U(r)} \rangle) \quad (2.1)$$

Where $\beta = 1/kT$ (with k =Boltzmann constant and T =temperature) and $U(r)$ is the potential energy of interaction of two particles whose centers of mass are at a distance r . The calculations involve placing a particle at a random position and orientation with centre to centre distance r from a fixed particle. The calculation is repeated for 10^5 different positions for each value of r and 10^3 different orientations for each position, checking for overlaps using the separating axes method. A histogram for the number of times the particle does not overlap with the fixed particle is maintained for different values of r ; this information is used to calculate the average Boltzmann's factors needed in Eq. 2.1. The results are shown in Fig. 2.1 where we set $r=1$ for the closest distance. The decay range of PMF (smallest r value for which $PMF=0$) indicate, in agreement with the asphericity values reported earlier, that the truncated octahedrons (and rhombic dodecahedrons) have the least degree of "anisotropy". The hexagonal prisms and cubes have intermediate degree of anisotropy while gyrobifastigiums (and triangular prisms) have the longest range of anisotropy. These PMFs are useful to estimate properties of the dilute suspensions (like second virial coefficients) [2], which are also easily measurable experimentally.

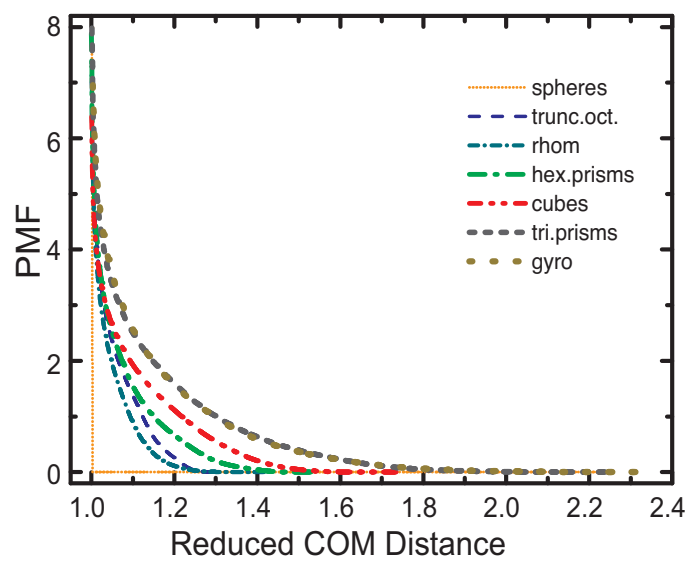


Figure 2.1: Potential of mean force for the SFPs considered in this work.

2.2 Translational order parameters

2.2.1 Bond-order orientational parameters

We used the Q_4 and Q_6 bond-order orientational parameters proposed by Steinhart et al. [3] to probe translational order in configurations of truncated octahedrons (and rhombic dodecahedrons). The values for these order parameters are generally sensitive to the crystal structure. However the Q_6 value increases monotonically with growing size of the crystal nucleus, irrespective of the type of structure [4]. Hence, we used Q_6 values to mark the boundaries of order-disorder transitions in translational order, while Q_4 values give additional information about the type of crystalline structure present in the system. These bond-order orientational parameters are defined as

$$Q_l = \left[\frac{4\pi}{2l+1} \sum_{m=-l}^l |\bar{Q}_{lm}(\vec{r})|^2 \right]^{\frac{1}{2}} \quad (2.2)$$

where $\bar{Q}_{lm}(\vec{r})$ is given by

$$\bar{Q}_{lm}(\vec{r}) = \frac{1}{N_b} \sum_{m=\text{bonds}} Y_{lm}(\vec{r}) \quad (2.3)$$

and the summation is over all the bonds (total number N_b) present in the system. Two particles are defined to be bonded if they are separated by a distance less than 1.2 times the position of the first peak in radial distribution function $[g(r)]$. And Y_{lm} are spherical harmonics for the neighboring particles position vectors \vec{r} , the angles that each such position vector makes (i.e., Θ and Φ) are defined with respect to an arbitrary laboratory frame.

2.2.2 Local bond-order parameters

To further analyze the structure of the plastic crystalline phase observed in truncated octahedrons, we used distributions of two local bond-order orientational parameters \bar{q}_4 and \bar{q}_6 which have a slightly modified definitions proposed by Lechner et al. [5].

$$\bar{q}_l(i) = \left[\frac{4\pi}{2l+1} \sum_{m=-l}^l |\bar{q}_{lm}(i)|^2 \right]^{\frac{1}{2}} \quad (2.4)$$

where,

$$\bar{q}_{lm}(i) = \frac{1}{\bar{N}_b(i)} \sum_{k=0}^{\bar{N}_b(i)} q_{lm}(k) \quad (2.5)$$

Thus, the complex vectors $q_{lm}(i)$ (with similar definition as in Eq. 2.2) of particle i and all its $\bar{N}_b(i)$ neighbors are averaged now to obtain the complex vectors $\bar{q}_{lm}(i)$, which make the distributions more disjoint for the various possible crystalline structures. These local order parameters are then used to calculate fractions of various possible crystalline orders in the rotator phase of truncated octahedrons. The probability vectors (\widehat{v}) for the distribution histograms [4] are obtained for the possible reference structures and the rotator phase and the fractions are obtained by minimizing Δ^2 with a constraint:

$$\Delta^2 = [\widehat{v}_{rot} - (f_{bcc}\widehat{v}_{bcc} + f_{fcc}\widehat{v}_{fcc} + f_{hcp}\widehat{v}_{hcp} + f_{liq}\widehat{v}_{liq})]^2$$

with, $f_{bcc} + f_{fcc} + f_{hcp} + f_{liq} = 1$ (2.6)

Using the vectors formed by concatenating both \bar{q}_4 and \bar{q}_6 distributions for the reference BCC, FCC, HCP, and liquid structures and the rotator phase at $\phi = 0.594$ (\widehat{v}_{bcc} , \widehat{v}_{fcc} , \widehat{v}_{hcp} , \widehat{v}_{liq} , and \widehat{v}_{rot}) we obtained the fractions for this mesophase as $f_{bcc}=0.001$, $f_{fcc}= 0.140$, $f_{hcp}=0.859$ and $f_{liq}=0$

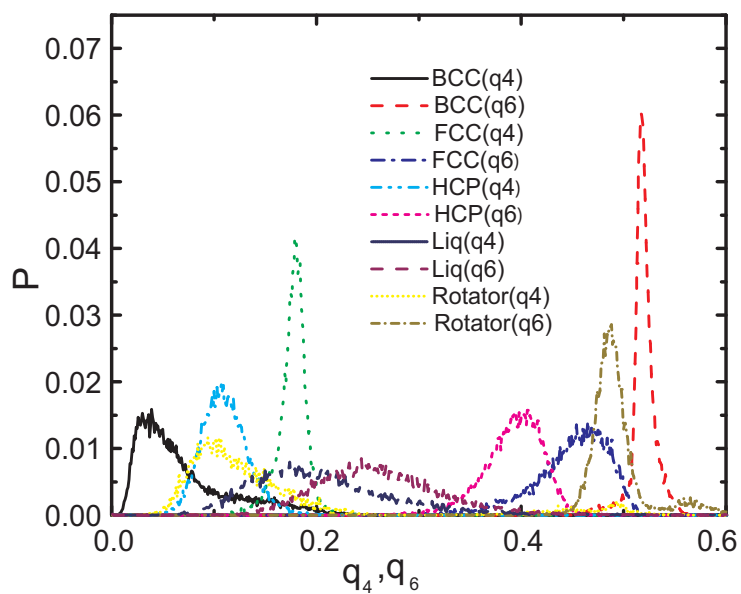


Figure 2.2: Probability distribution of locally averaged bond orientational order parameters (q_4 and q_6) for the FCC, BCC and HCP crystals, liquid state of hard spheres and for rotator phase of truncated octahedrons at $\phi = 0.594$.

2.2.3 Translational mobility coefficients

To characterize liquid crystalline phases with respect to translational mobility (disorder) of its particles as in cubes and hexagonal prisms, the mean squared displacements were calculated by carrying out NvT simulations of the equilibrated phases with a fixed move set consisting of particle translations and rotations. These moves were “pseudo dynamic” as only small perturbative translations and rotations (values obtained from previous NpT simulation in which acceptance probability P_{acc} is kept constant) were allowed to mimic the diffusive motion. The use of these particular values for controlling translational and rotational moves at various volume fractions promotes average motions at various state points that are similar in the sense of ‘time’ per MC cycle. The mean square displacement over a pseudo time of N_s MC cycles is given by the equation

$$R_s = \frac{\sum_{i=1}^N \sum_{j=0}^{N_{MC}-N_s} |\Delta r_{(j+s),j}^i|^2}{N(N_{MC} - N_s)} \quad (2.7)$$

where $\Delta r_{(j+s),j}^i$ is the displacement of the centre of mass of the i^{th} particle between the j^{th} and $(j + s)^{th}$ MC cycles and N_{MC} is the total number of MC cycles in the simulation. By determining the rate of change of this displacement with time (number of MC cycles) a quantity defined as mobility coefficient (D) is obtained. Although the physical interpretation of this quantity is difficult, as there is no direct correlation between MC cycles and time, the coefficient gives a good relative measure of the mobility of particles in different phases.

2.3 Orientational order parameters

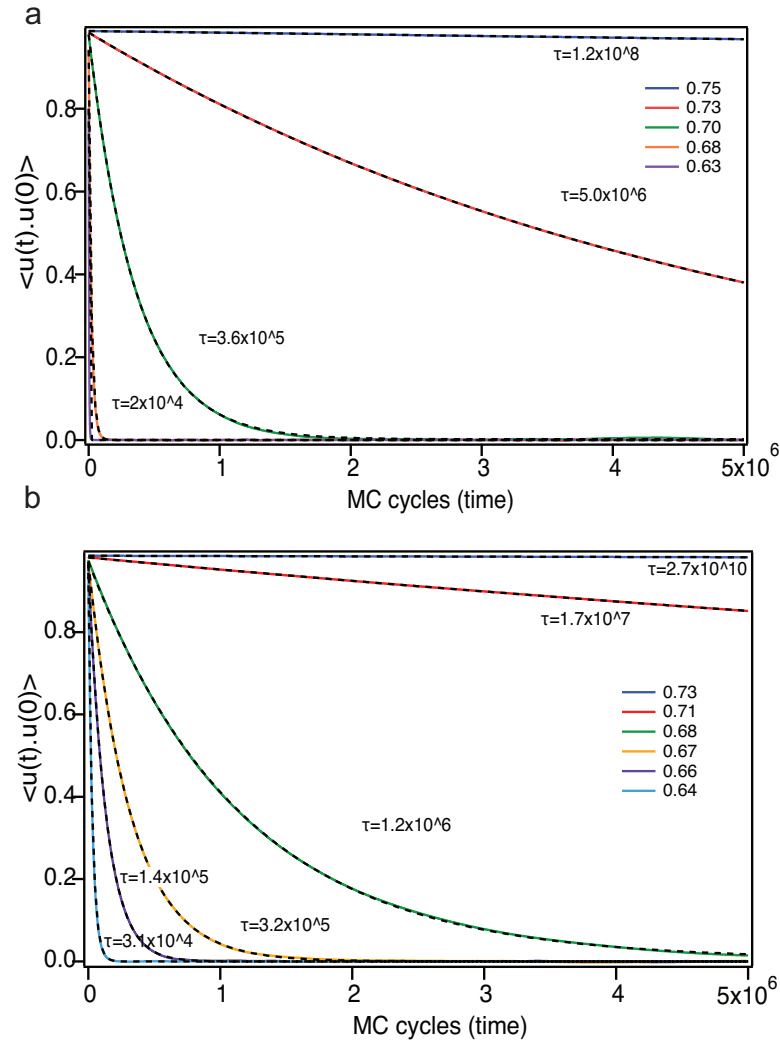


Figure 2.3: Rotational autocorrelation function against number of MC cycles for various concentrations (ϕ) around the rotator-crystal transition in a) truncated octahedrons and b) rhombic dodecahedrons. Some fitted exponential decay curves are shown as dashed lines with their corresponding values of the time constants for decay (τ).

2.3.1 Cubatic order parameters

To measure the orientational order in phases having particles with cubic symmetry (truncated octahedrons, rhombic dodecahedrons and cubes) or exhibiting a mesophase with cubatic order, we used a cubatic order parameter $\langle \bar{P}_4 \rangle$ defined as:

$$\begin{aligned} \langle \bar{P}_4 \rangle &= \max_{\hat{n}} \frac{3}{14N} \sum_i P_4(\hat{u}_i \cdot \hat{n}) \\ &= \max_{\hat{n}} \frac{3}{14N} \sum_i (35 \cos^4 \theta_i(\hat{n}) - 30 \cos^2 \theta_i(\hat{n}) + 3) \end{aligned} \quad (2.8)$$

where \hat{u}_i is the unit vector along a relevant particle axis and \hat{n} is a director unit vector which maximizes $\langle \bar{P}_4 \rangle$. To find the director unit vector \hat{n} and the value of maximum order parameter, we used an approximate numerical recipe detailed in [6]. This recipe yields the director vectors \hat{n}_1 and \hat{n}_2 and the corresponding values of order parameters $[\langle \bar{P}_4 \rangle]_1$ and $[\langle \bar{P}_4 \rangle]_2$, such that \hat{n}_1 and \hat{n}_2 are most orthogonal to each other with maximum possible values for $[\langle \bar{P}_4 \rangle]_1$ and $[\langle \bar{P}_4 \rangle]_2$.

Another set of rotationally invariant orientational order parameters which can be used to measure orientation order are I_2 and I_4 [6],[7]. These parameters are defined by combination of spherical harmonics quite similar to the bond order orientational parameters discussed in the translational order parameter section:

$$I_l = \left\langle \frac{4\pi}{2l+1} \sum_{m=-l}^l |\bar{Q}_{lm}(\vec{r}')|^2 \right\rangle \quad (2.9)$$

where $\bar{Q}_{lm}(\vec{r}')$ is calculated with a relation similar to Eq. 2.3, but rather than using the neighboring particles vectors for \vec{r}' , one considers the longitudinal axial vectors for all the particles (with respect to an arbitrary coordinate frame).

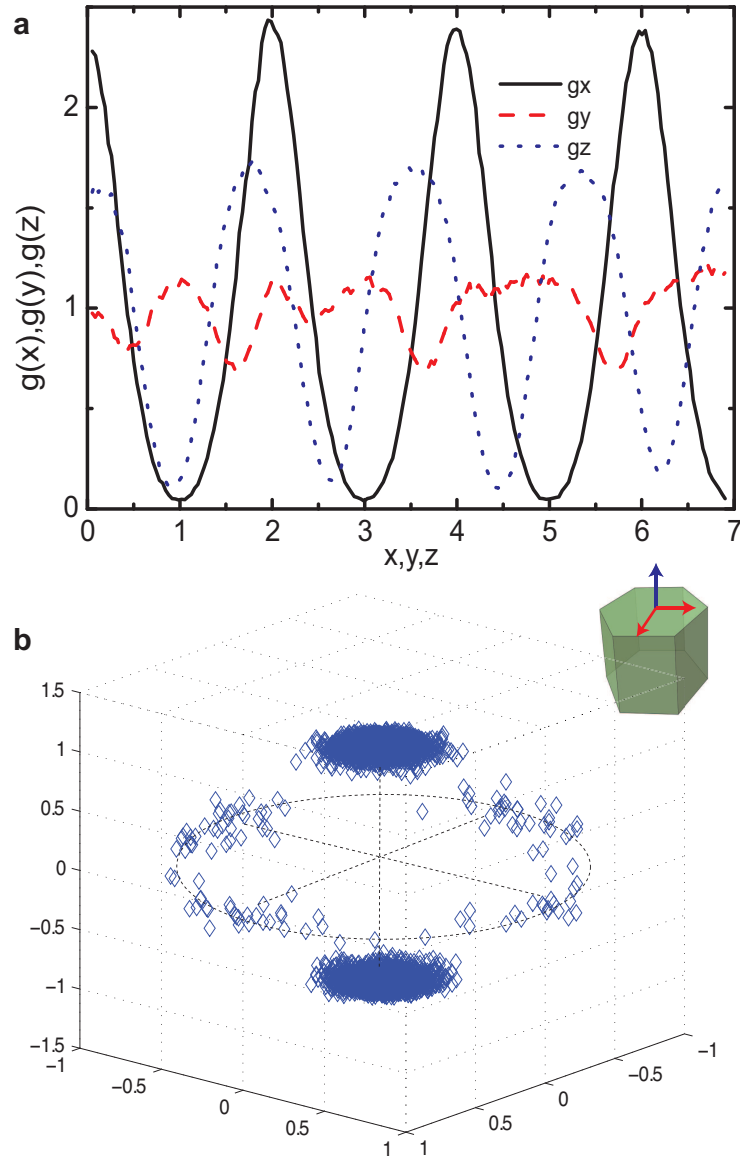


Figure 2.4: (a) Particle distribution function and (b) Orientational distribution function for RPS phase of hexagonal prisms at $\phi = 0.619$. The unit vectors along blue particle axes are used to plot the orientational distribution function.

2.3.2 Rotational auto-correlation function

To capture plastic crystalline behaviour in mesophases we used a simple auto-correlation function which measures the degree of alignment of particle orientation vectors over time. The function is given by

$$A_s = \frac{\sum_{i=1}^N \sum_{j=0}^{N_{MC}-N_s} |\widehat{\mathbf{u}}_{(j)}^i \cdot \widehat{\mathbf{u}}_{(j+s)}^i|^2}{N(N_{MC} - N_s)} \quad (2.10)$$

Where $\widehat{\mathbf{u}}$ are the unit vectors along the particle axes, N_{MC} is the total number of Monte Carlo cycles and N_s is the time equivalent number of MC cycles over which the alignment autocorrelation is measured. Fig. 2.3 shows the autocorrelation function against MC cycles for different densities around the crystal-rotator phase transition in a) truncated octahedrons and b) rhombic dodecahedrons. We see a change of behaviour from a roughly linear decay (weak exponential with large time constants) to a fast exponential decay for A_s over a narrow density range around $\phi = 0.70$ in truncated octahedrons and around $\phi = 0.68$ in rhombic dodecahedrons, which hence are marked as the approximate boundaries for the crystal-rotator transitions.

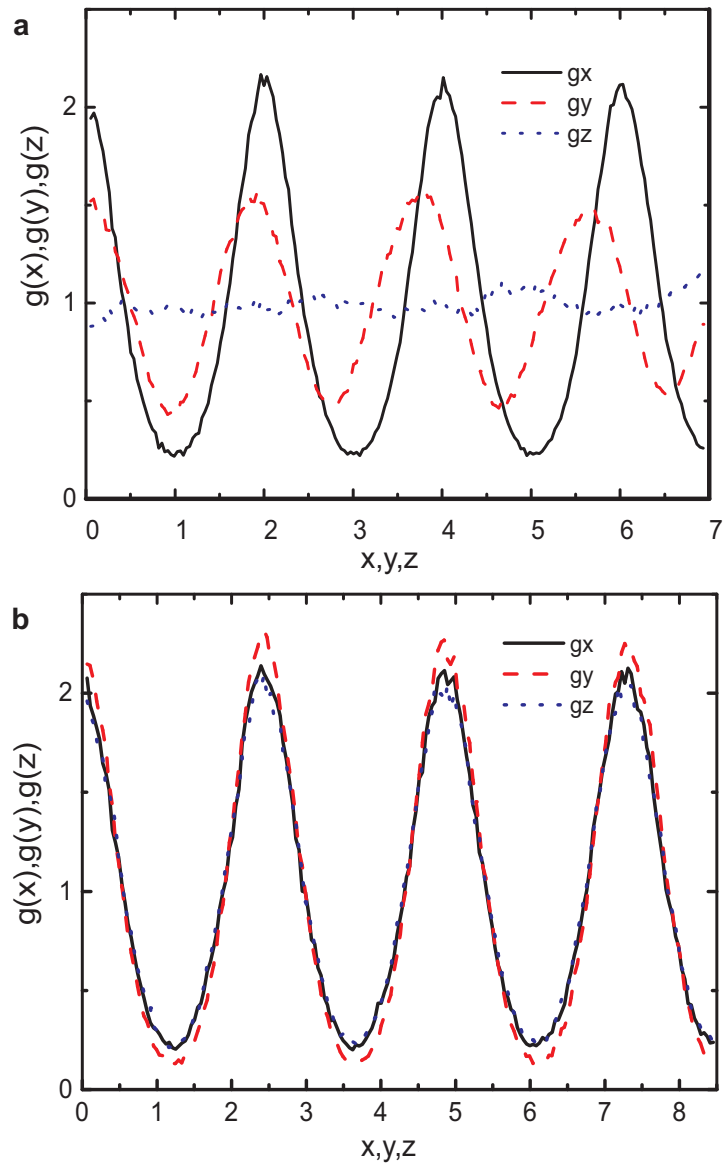


Figure 2.5: Particle distribution functions for cubatic-like phases of (a) hexagonal prisms and (b) cubes.

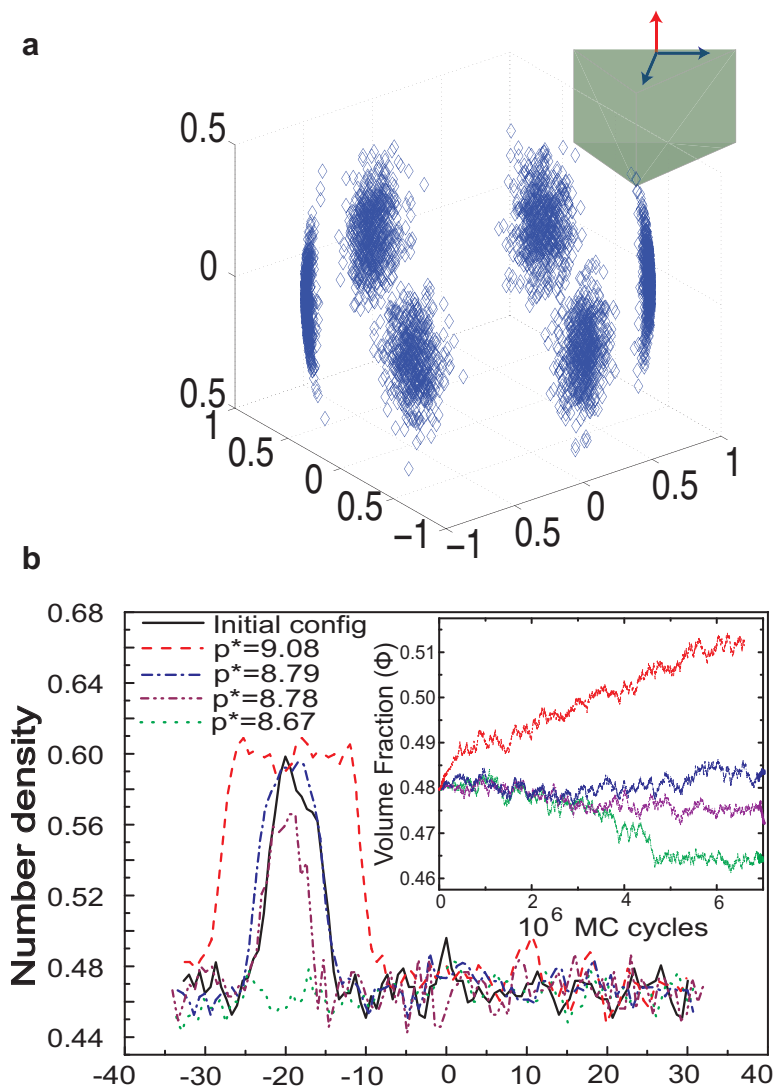


Figure 2.6: Results for triangular prisms:(a) Orientational distribution with respect to the transverse axes at $\phi = 0.59$. The unit vectors along blue particle axes are used to plot the orientational distribution function.(b) Number density profile against the z-axis of the simulation box, in units of height of the prism (Inset: Evolution of the total volume fraction) of the inhomogeneous system comprised of coexisting crystalline and isotropic phases of triangular prisms, obtained from direct NpT simulations at different pressure values.

2.4 Distribution Functions

2.4.1 Particle distribution functions

Particle density distribution functions are useful to unveil translational order in the form of layering of particles; these are often calculated along the simulation box axes [6]. However, for some of the configurations obtained from expansion runs and for most of those obtained from compression runs, the molecular axes are not aligned with the coordinate axes of the simulation box. Therefore, we used a modified definition of the particle correlation functions, which is now based on distances of particles calculated along the three orthogonal axes obtained as director vectors (\widehat{n}_1 and \widehat{n}_2) for maximizing the cubatic order parameters ($[\langle \overline{P}_4 \rangle]_1$ and $[\langle \overline{P}_4 \rangle]_2$) described in section 3.1 above and from their cross product ($\widehat{n}_3 = \widehat{n}_1 \times \widehat{n}_2$).

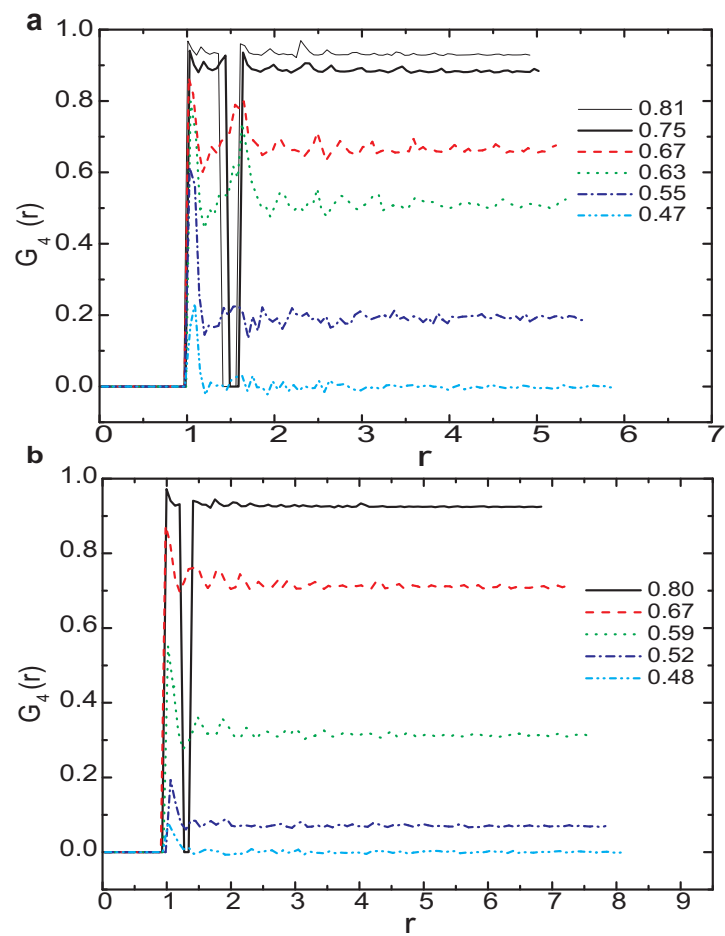


Figure 2.7: Orientational correlation functions at various volume fractions for (a) truncated octahedrons and (b) rhombic dodecahedrons.

The particle distribution functions obtained for crystalline phases of all the SFPs show perfect positional order (in the form of pronounced non-decaying peaks), and liquid phases show flat distributions, as should be expected. Interestingly, for the liquid crystalline phases observed for cubes and hexagonal prisms, these functions reveal that there is significant amount of layering in these phases. The particle distribution functions for the plastic crystalline of hexagonal prisms is shown in Fig. 2.4 and for the cubatic phase of hexagonal prisms and cubes in Fig. 2.5. These distributions bring out the significant layering present in cubatic phases, even though the translation mobility calculations indicate a dynamic translational disorder in these systems; the precise mechanism for particle motion in these mesophases is still unclear and currently under investigation.

2.4.2 Orientational distribution function

For getting a qualitative idea of the orientational order in mesophases, we used orientational distribution functions obtained by plotting the unit vectors for relevant particle axes on a unit sphere. Fig. 2.4b shows the six-fold discrete orientational disordering of particles in restricted plastic crystalline phase of hexagonal prisms. Similarly, Fig. 2.6a shows the orientational distribution function of the lowest density crystal phase of triangular prisms with respect to their transverse axes, elucidating the restriction on rotation of particles out of their original plane.

2.4.3 Orientational correlation function

To compare the local modes of order in the different phases of truncated octahedrons and rhombic dodecahedrons, we used the P_4 orientational correlation function. This function measures mutual alignment of particles separated by a distance ' r ' and is defined by

$$G_4(r) = \frac{3}{14} \langle 35 [\widehat{u}_{ai}(0) \cdot \widehat{u}_{bi}(\vec{r})]^4 - 30 [\widehat{u}_{ai}(0) \cdot \widehat{u}_{bi}(\vec{r})]^2 + 3 \rangle \quad (2.11)$$

where the ensemble average is over all particle pairs ' a ' and ' b ' and all nine combinations of the axes. The correlation function is plotted at different volume fraction values for truncated octahedrons and rhombic dodecahedrons in Fig 2.7a and S7b, respectively. In all cases, the first peak at the contact distance reveals that orientation correlations are stronger among nearest neighbors. In the crystalline phases the function plateaus at relatively high values (for $\phi > 0.70$ for truncated octahedrons and for $\phi > 0.68$ for rhombic dodecahedrons). The alignment is reduced in the rotator phase as indicated by shortening of the first peak and plateau values (the latter reflecting the global values of $\langle \overline{P}_4 \rangle$ already reported in the main text) which keep diminishing with volume fraction. The isotropic phase for $\phi < 0.47$ has only slight orientation correlations among first neighbors and no long-range order.

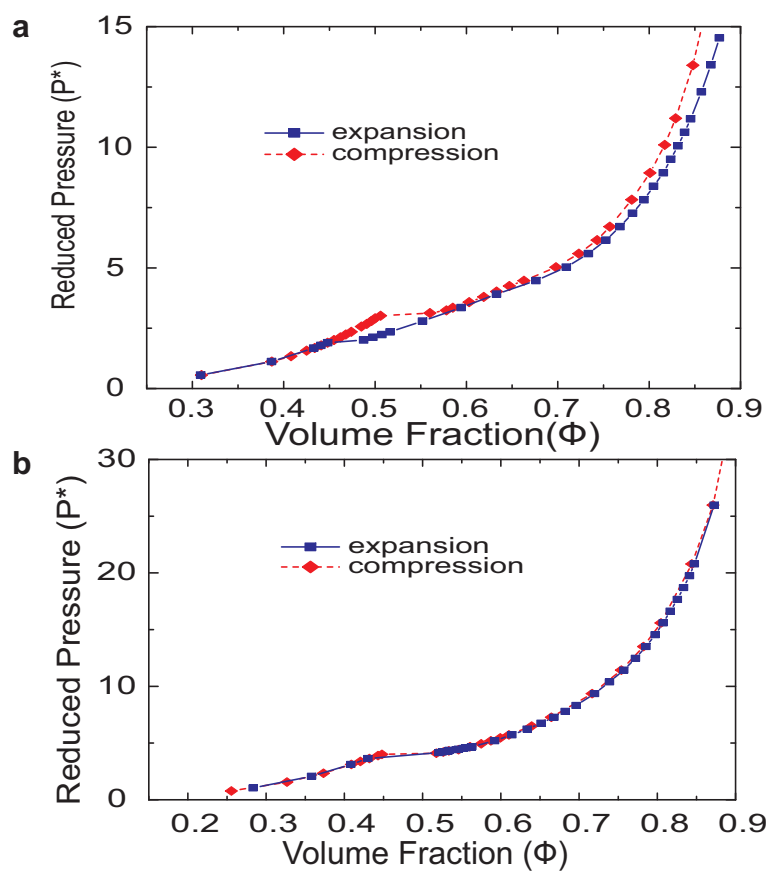


Figure 2.8: Complete equations of state from compression and expansion runs for (a) truncated octahedrons and (b) cubes.

2.5 Direct coexistence simulation of triangular prisms

For determining the coexistence conditions for solid-liquid transition of triangular prisms we used a direct simulation of inhomogeneous phase method, which was recently shown by Noya et. al. [8] to generate coexistence properties for hard spheres in excellent agreement with those obtained from free energy calculations. The initial two-phase system is built by performing direct interfacial NVT simulations (described in *Methods* of main text) using the solid-liquid coexistence density estimates from the expansion runs. Though the final configuration obtained has a larger liquid region because of the starting density values being skewed towards the liquid region (hysteresis effect), it can already be used to estimate the coexistence densities from the density profiles along the box long axes (as in Fig. 2.6b). To confirm these data and obtain a direct estimation of the coexistence pressure P_{melt}^* , we used this “crystal-nucleated liquid-rich” phase (shown in Fig. 1.2f of main text) as the initial configuration for a series of NpT ensemble simulations at different values of the dimensionless osmotic pressure (P^*) from $P^* = 8.67$ to $P^* = 9.08$. The crystal nucleus (and overall density) is expected to grow if $P^* > P_{melt}^*$, while it is expected to melt (and the density to decrease) if $P^* < P_{melt}^*$. The inset of Fig. 2.6b shows how the overall density evolves during the simulation for different values of P^* ; it increases with simulation time for $P^* > 8.79$ while it decreases for $P^* < 8.78$, hence these values bracket the estimate of P_{melt}^* . As visible in Fig. 1.6b, for $P^* > P_{melt}^*$ the peak in the number density profile broadens, indicating an increase in the crystalline region (toward becoming 100% crystalline), while for $P^* < P_{melt}^*$ the density peak disappears signaling the melting of the initial solid nucleus. For P_{melt}^* , the peak widens very slowly but allows estimation of the coexistence densities as $\phi_{solid}=0.59$ and

$\phi_{liquid}=0.47$ (values consistent with those for the initial *NVT* configuration).

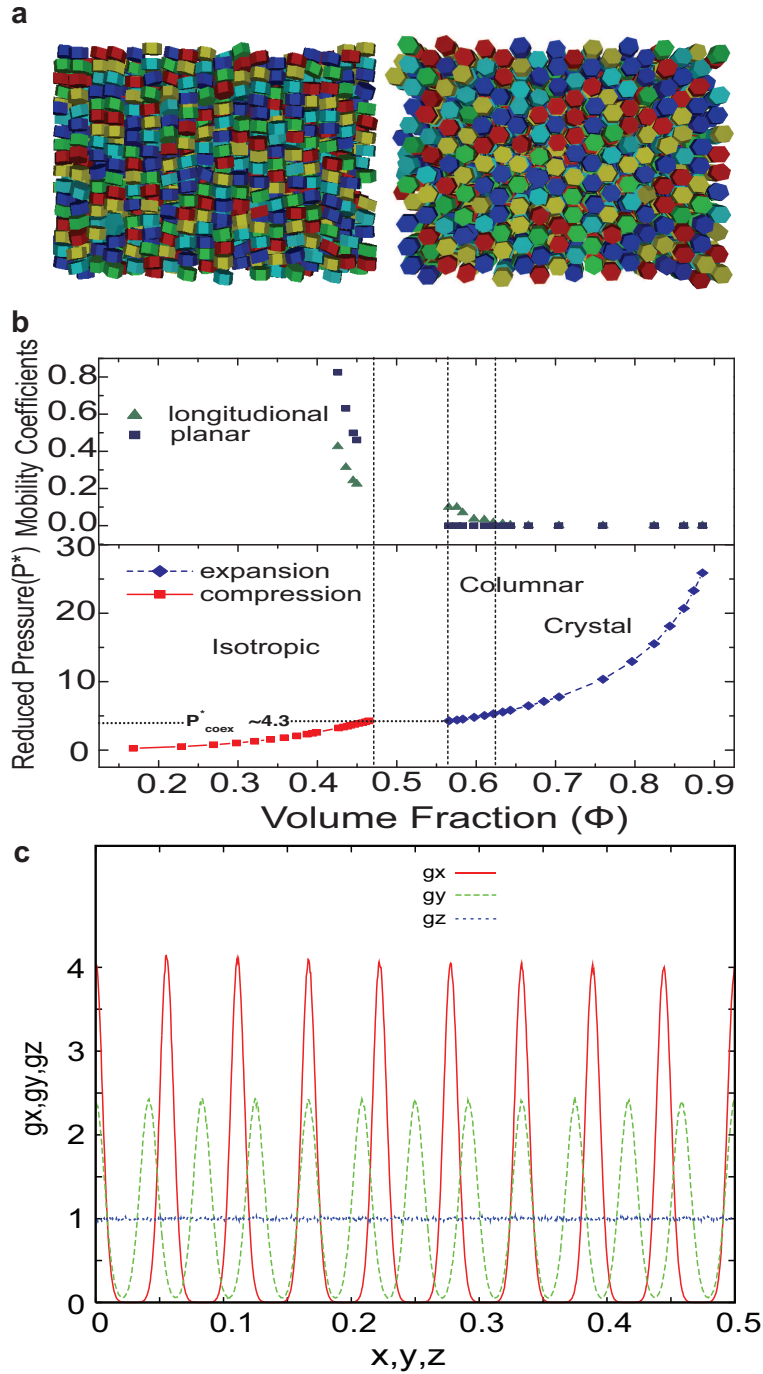


Figure 2.9: Results for hexagonal prisms of aspect ratio 0.5: (a) Snapshot of the columnar phase at $\phi=0.57$: front view (left) and top view (right) (b) Equation of state (bottom frame) obtained from expansion and compression NpT runs and translational mobility coefficients (top frame) along and perpendicular to the columnar phase director (particle axes) (c) Particle distribution function for the columnar phase at $\phi=0.57$.

2.6 Hysteresis in equations of state

Hysteresis effects across a first-order melting transition were observed to be larger for translationally ordered phases than for orientationally ordered phases. To illustrate this effect, Fig. 2.8 shows the complete equations of state obtained by independent compression and expansion runs for truncated octahedron (Fig. 2.8a) and cubes (Fig. 2.8b). As it can be seen, while there is a large hysteresis across the transition for truncated octahedrons, it is almost negligible for cubes.

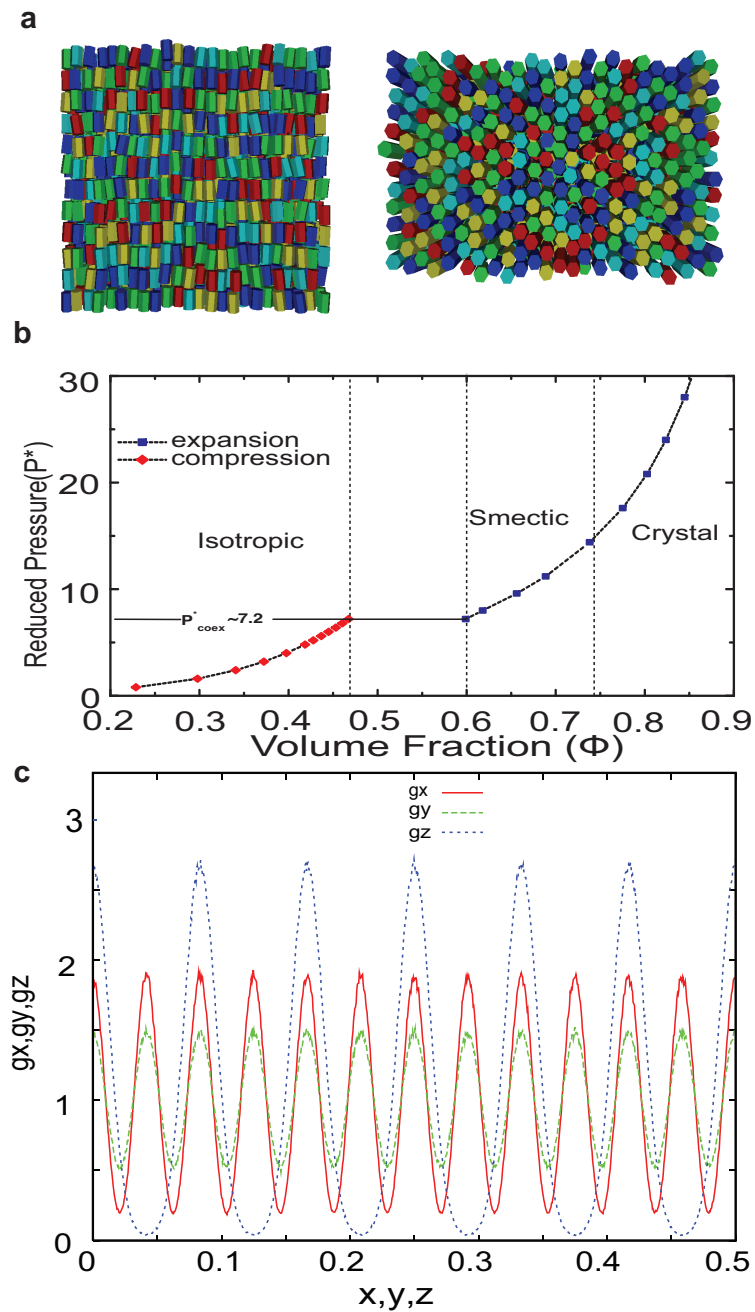


Figure 2.10: Results for hexagonal prisms of aspect ratio 2.0: (a) Snapshot of the smectic-like phase at $\phi=0.59$: front view (left) and top view (right); (b) Equation of state obtained from expansion and compression NpT runs; (c) Particle distribution function for the smectic phase at $\phi=0.59$.

2.7 Case Study A: Hexagonal Prisms of different aspect ratios

2.7.1 Aspect ratio 0.5

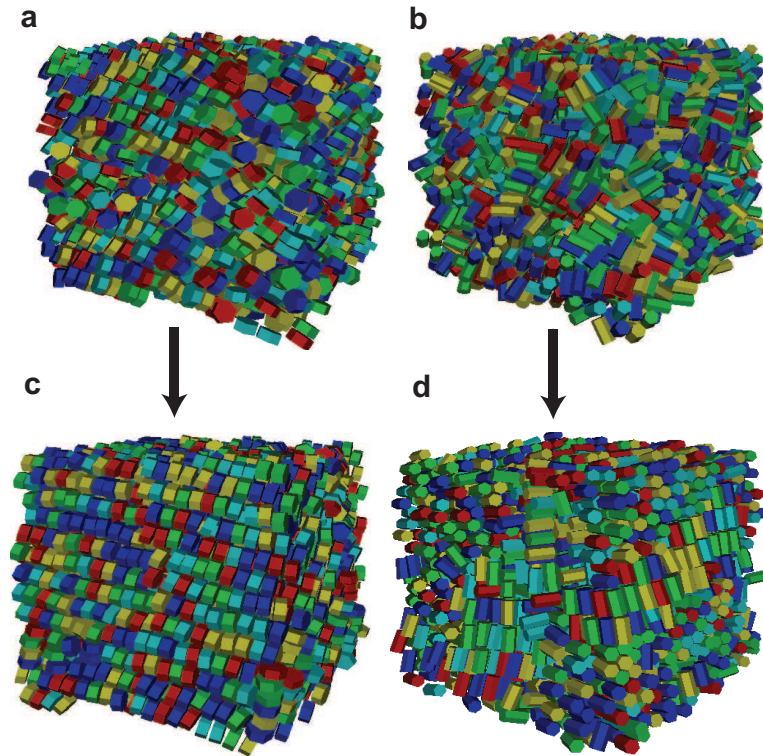


Figure 2.11: Snapshots of the metastable cubatic-like phase observed in compression runs of hexagonal prisms of aspect ratio (a) 0.5 and (b) 2.0, showing stacks of particles on top of each other for the 0.5 aspect ratio and sideways for the 2.0 aspect ratio. (c) and (d) Snapshots obtained from longer runs showing gradual development of more ordered but still defective mesophases.

Expansion and compression runs for hexagonal prisms of aspect ratio = 0.5 indicate presence of a columnar phase (Fig. 2.9a) at intermediate densities, bounded by a continuous transition from the HCP crystalline phase at higher densities and by a first-order transition from the isotropic phase at lower densities. The equation of state obtained by combining results from expansion and compression runs is shown in Fig. 2.9b with the approximate phase boundaries marked. The columnar phase has high amount of translational order in two directions; i.e., the prisms pack in a hexagonal lattice laterally, but remain disordered along the third direction as indicated in the particle distribution function plot (at $\phi=0.57$) shown in Fig. 2.9c.

Because of the high amount of hysteresis in the expansion and compression runs, we used direct coexistence simulations to mark out the phase boundaries for the isotropic-columnar phase transition, which came out to be $\phi_{columnar}=0.57$ and $\phi_{liquid}=0.47$. The columnar-crystal phase transition was detected by the translational mobility coefficient calculations (along the longitudinal direction). The plot shown in the top frame of Fig. 2.9b indicates that at $\phi = 0.63$ the mobility coefficient values along the main axes exhibit an order of magnitude jump (while the ones along the planar axes remain almost constant) indicating the transition to a columnar phase. Hence, the stability region for the columnar phase is approximately $0.57 < \phi < 0.63$.

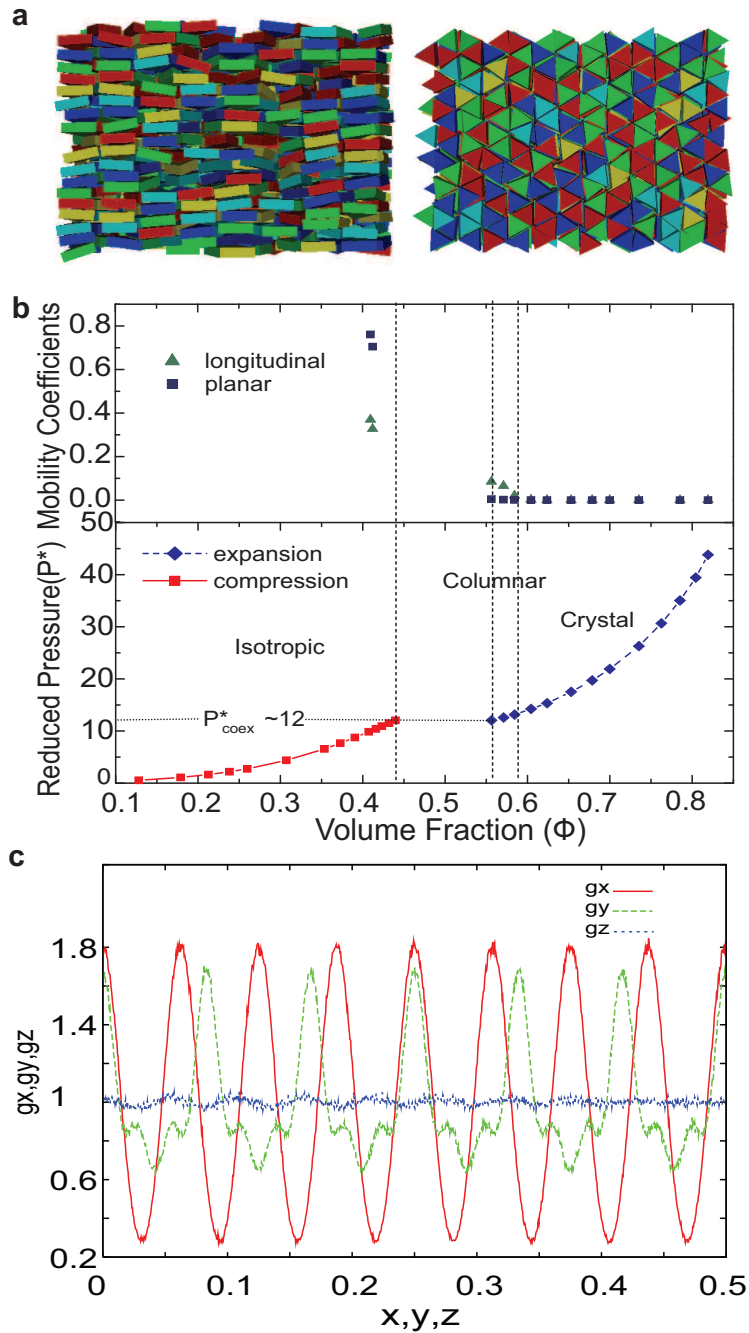


Figure 2.12: Results for triangular prisms of aspect ratio 0.5: (a) Snapshot of the columnar phase at $\phi=0.56$: front view (left) and top view (right) (b) Equation of state (bottom frame) obtained from expansion and compression NpT runs and translational mobility coefficients (top frame) along and perpendicular to the columnar phase director (particle axes) (c) Particle distribution function for the columnar phase at $\phi=0.56$.

2.7.2 Aspect ratio 2.0

The aspect ratio 2.0 hexagonal prisms show a smectic-like phase (Fig. 2.10a) at densities between the crystalline and isotropic phases. The equation of state obtained from expansion and compression runs is plotted in Fig. 2.10b. The intermediate phase looks like a precursor to the smectic A phase with distinct layers being formed, which are laterally shifted with respect to each other, but unlike the smectic phase, each layer has substantial translational and orientational order (i.e., within a layer plane). If not for the motion associated with the interlayer shifts (which is the only source of translational disorder), this intermediate phase could have been regarded as a loose solid. The coexistence densities for smectic-like and isotropic phase transition are estimated to be $\phi_{smectic}=0.59$ and $\phi_{liquid}=0.47$ by direct coexistence simulations while the boundary between smectic-like and crystal phase is roughly estimated to be at $\phi \approx 0.75$ by visual inspection of equilibrated snapshots trying to detect the onset of interlayer shifts.

It is noted that for both aspect ratios 0.5 and 2.0, the prisms sometimes form a metastable cubatic phase in the compression runs (instead of the equilibrated columnar and smectic phases), as shown in Fig. 2.11a and 2.11b, similar to the hard cut spheres ($L/D=0.1$) in [9]. With 3×10^6 MC cycles at the transition point the particles form short stacks (or layers) which are packed orthogonally to each other and the overall order appears to be like that of a cubatic phase. These stacks, however, tend to rotate in a very slow process; e.g., even with 2×10^7 MC the expected crystalline phase obtained has some defects (Fig. 2.11c and 2.11d). The cubatic phase, which is only observed in compression runs, is therefore regarded as a metastable precursor (a jammed state) of a columnar/smectic phase.

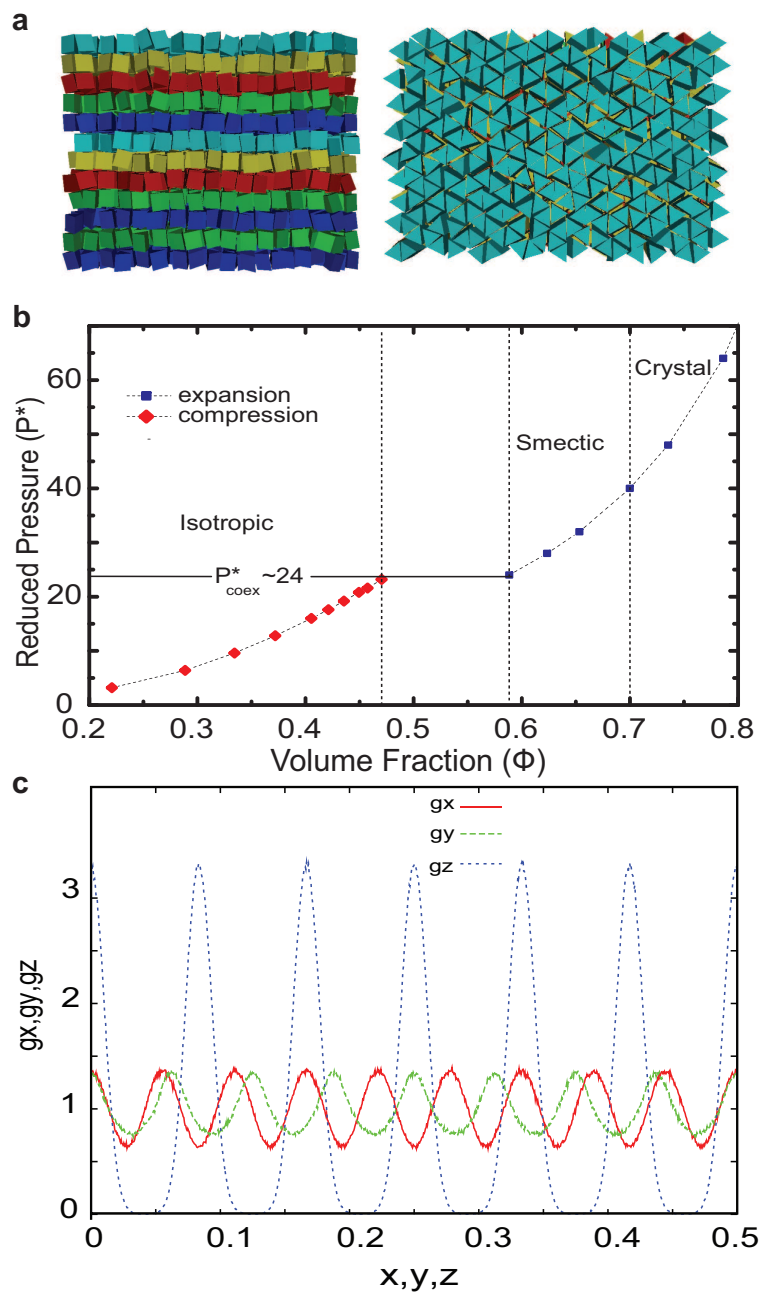


Figure 2.13: Results for triangular prisms of aspect ratio 2.0: (a) Snapshot of the smectic-like phase at $\phi=0.59$: front view (left) and top view (right) (b) Equation of state obtained from expansion and compression NpT runs (c) Particle distribution function for the smectic phase at $\phi=0.59$.

2.8 Case Study B: Triangular Prisms of different aspect ratios

2.8.1 Aspect ratio 0.5

Similar to hexagonal prisms, expansion and compression runs for triangular prisms of aspect ratio 0.5 also indicate presence of a columnar phase (Fig. 2.12a) at intermediate densities. The equation of state obtained by combining the expansion run branch for the ordered phases and compression run for the isotropic phase is shown in (Fig. 2.12b). The coexistence densities for the first order mesophase to liquid phase transition are estimated by direct coexistence simulations to be $\phi_{columnar}=0.56$ and $\phi_{liquid}=0.44$. The columnar-crystal phase transition was estimated by the translational mobility coefficient calculations (top frame Fig. 2.12b) which show transition at $\phi=0.58$ for the coefficients along the particle axes, establishing $0.56 < \phi < 0.58$ as the region for columnar phase stability.

2.8.2 Aspect ratio 2.0

Triangular prisms of aspect ratio 2.0 also show a smectic-like phase (Fig. 2.13a) similar to the one observed for hexagonal prisms. The equation of state obtained from expansion and compression runs is plotted in Fig. 2.13b. The coexistence densities for smectic-like and isotropic phase transition are estimated to be $\phi_{smectic}=0.59$ and $\phi_{liquid}=0.47$ by direct coexistence simulations, while the boundary between smectic and crystal phases (estimated by visual detection of interlayer shifting) is $\phi \approx 0.70$.

BIBLIOGRAPHY

- [1] McQuarrie DA (1975) *Statistical Mechanics*. (Harper and Row, New York).
- [2] Hill TL (1987) *An introduction to statistical thermodynamics* (Donev Publications Inc., New York)
- [3] Steinhardt PJ, Nelson DR, Ronchetti M (1983) Bond-orientational order in liquids and glasses. *Phys Rev B* 28:783-805.
- [4] ten Wolde PR, Ruiz-Montero MJ, Frenkel D (1995) Numerical evidence for bcc ordering at the surface of a critical fcc nucleus. *Phys Rev Lett* 75:2714-2717.
- [5] Lechner W, Dellago C (2008) Accurate determination of crystal structure based on averaged local bond order parameters. *J Chem Phys* 129:114707.
- [6] John BS, Escobedo FA (2008) Phase behaviour of colloidal hard perfect tetragonal parallelepipeds. *J Chem Phys* 128:044909.
- [7] Blaak R, Frenkel D, Mulder BM (1999) Do cylinders exhibit a cubatic phase? *J Chem Phys* 110:11652-11659.
- [8] Noya EG, Vega C, Miguel E (2008) Determination of the melting point of hard spheres from direct coexistence simulation methods. *J Chem Phys* 129:114707.
- [9] Duncan PD, Dennison M, Masters AJ, Wilson MR (2009) Theory and computer simulation for the cubatic phase of cut spheres. *Phys Rev E* 79: 031702.

CHAPTER 3
EFFECT OF QUENCHED SIZE POLYDISPERSITY ON THE PHASE
BEHAVIOR OF POLYHEDRAL PARTICLES

3.1 Abstract

Monodisperse polyhedral nanocrystals with O_h (octahedral) symmetry are expected to self-assemble into various mesophases and crystal structures at intermediate and high packing densities. In this work, the effect of size polydispersity on phase and jamming behavior has been studied via molecular simulations for three representative O_h polyhedral shapes; namely, cubes, cuboctahedrons and truncated octahedrons. Polydispersity is quantified via the parameter δ , which gives the standard deviation of an underlying Gaussian distribution of particle sizes, and is quenched in that it is fixed in a given uniphase sample. Quenched polydisperse states are relevant to: (i) equilibrium behavior for small enough polydispersities when phase segregation does not occur, and (ii) actual experimental behavior for arbitrary polydispersity when dense states are reached at a rate faster than the relaxation of slow diffusion-driven fractionation modes. Space-filling polyhedrons (cubes and truncated octahedrons) are found to be more robust with respect to the nucleation of orientational and translational order at high polydispersities compared to the non space-filling cuboctahedron, with the former shapes exhibiting an onset of jamming behavior at a critical polydispersity δ_c that is about twice larger than that for the latter ($\delta_c \approx 0.08$). Further, the orientational ordering in cubes is found to be highly resilient to polydispersity values as high as $\delta=0.30$, leading to the formation of a novel high-volume-fraction ($\phi \sim 0.83$) orientationally aligned and translation-

ally jammed state. Both space-filling polyhedrons also show local fractionation of particles into coexisting solid and liquid clusters at intermediate polydispersity values just above δ_t . Overall, increasing size polydispersity enhances the range of pressures where the mesophases occur.

3.2 Introduction

Recent advances in nanocrystal synthesis [1, 2] have made possible the formation of a wide variety of polyhedral shapes belonging to diverse symmetry groups and having varying degrees of anisotropy. Non-spherical nanoparticles can arrange themselves into extended superlattices[3]-[5] and can also form mesophases with partial order at intermediate packing densities[6, 7]. These assemblies exhibit vastly different optical, electronic, physical and chemical properties[8, 9] depending on nanocrystal size and shape and their superstructure symmetry. Synthesis of colloidal nanoparticles typically results in size polydispersity[10], which may affect the assembly of superstructures in non-trivial ways. For instance, size polydispersity in hard sphere systems results in formation of glasses[11, 12] or fractionation into several coexisting solids[13] with spatially varying average diameter distributions. In length polydisperse rods, partitioning of components and orientational order takes place between the isotropic and nematic phases[14]: In the nematic phase the longer rods concentrate and align but short rods remain orientationally disordered, while in the isotropic phase the longer rods are dilute but form small bundles. Since polyhedrons have both orientational and translational degrees of freedom, polydispersity-induced jamming or segregation may occur with respect to either or both of these kinds of order. To the best of our knowledge, the effect of polydispersity on the phase behavior of polyhedral nanocrystals and its dependence on particle geometry remains unexplored (polydisperse cubes have been studied but only when constrained to be parallel or on a lattice[15, 16, 17]). The present study aims at obtaining a basic understanding of the changes in phase behavior of different polyhedral shapes brought about by the introduction of in-

creasing amounts of quenched polydispersity in their particle size distribution.

A class of polyhedral nanocrystals with O_h symmetry has become readily synthesizable by controlling the growth step in a modified polyol process for the formation of gold nanocrystals[18]-[20]. The assemblies of these Au nanocrystals have a wide range of applications such as in biosensing, photovoltaics, surface plasmonics, and photo thermal therapy[22]-[25]. The different polyhedral shapes formed at specific growth stages in the formation of cubic Au/Ag nanocrystal vary from that of an octahedron to a truncated octahedron, cuboctahedron, truncated cube and cube in increasing order of size (as shown in Fig 3.1)[18]. The phase behavior of the two space-filling members of this class (cubes and truncated octahedrons) has already been established[6, 7], while the phase behavior of other non space-filling members agrees closely with the guidelines suggested in ref. 6 regarding the correlation between mesophase type and the two geometry defining parameters: particle shape asphericity and rotational symmetry. It should be pointed out, however, that the liquid-crystal character of a putative cubatic mesophase for cubes at concentrations near the order-disorder transition has recently been called into question[26]. This is based on the observation of an extent of translational order that would be consistent with crystal order (this issue will be revisited later in light of our results).

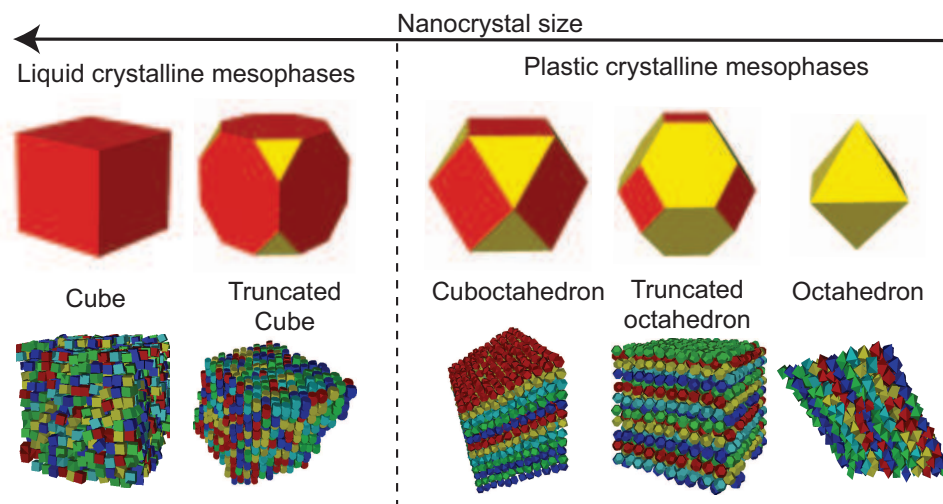


Figure 3.1: Nanocrystal shapes synthesized at different growth stages of the modified polyol process. The snapshots show the simulated mesophases at the order-disorder transition point (particle colors are used to highlight layering behavior).

As marked in Fig. 3.1, truncated cubes show a phase behavior that is very similar to that of the cubes (results shown in Fig. 3.9 of the Supplementary Information). Cuboctahedrons and octahedrons show similar phase behavior as truncated octahedrons[6] with cuboctahedrons showing two first order transitions (instead of one, as in truncated octahedrons[6]) separating the three phases: an isotropic liquid phase, a rotator or plastic crystalline phase (with translational order but no orientational order) and a crystalline solid phase with both kinds of order (Fig. 3.10 in the SI). Size polydispersity is expected to have a non-trivial effect on the ordered phases of these polyhedra because it will tend to weaken the directional "entropic bonds" [27] responsible for bringing particles together with complementary facets in parallel alignment (thus optimizing packing and maximizing translational entropy) at high concentrations[6, 7]

We chose three shapes: cubes, cuboctahedrons and truncated octahedrons (which encompass three distinct types of phase behavior) to investigate the effects of quenched polydispersity on the nucleation of orientational and translational order in polyhedral assemblies. The comparison of cubes (that form a liquid crystal mesophase) vs. the other two shapes (that form a plastic crystal mesophase) will address the question: how does size polydispersity affect the establishment of different types of mesophases? The comparison of cuboctahedrons (whose monodisperse densest packing does not tessellate space) vs. truncated octahedrons (whose monodisperse densest packing tessellates space) will address the question: how does size polydispersity affect the establishment of the same types of order (mesophase and crystal) when the original particle shape is either non-space filling or space filling? In this work we are only concerned with quenched size polydisperse, wherein the size of any given particle remains fixed throughout (as opposed to being periodically sampled from an

underlying distribution), and particles can only locally (pseudo-dynamically) diffuse, and hence no macrophase separation could be detected for the system sizes employed here. As such, our simulations will not capture thermodynamic behavior at conditions where phase partitioning could occur (e.g., for large polydispersities), but will be representative of an experimental scenario where dense states are reached at a rate faster than the relaxation of slow diffusion-driven fractionation modes.

3.3 Methods

Compression runs were used to obtain the phase behavior of each shape for different degrees of polydispersity. Expansion runs for cubes show no hysteresis and the two curves overlap each other as shown Fig. 3.11 of the SI; for truncated octahedrons and cuboctahedrons a small amount of hysteresis is observed around any first-order order-disorder transition (as in the monodisperse cases). Isothermal-isobaric NpT Monte Carlo simulations were carried out to obtain the equilibrated structure at each pressure state point. Each shape was simulated for 12 different polydispersity values ($\delta = 0.02, 0.04, \dots, 0.20, 0.25, 0.30$) with the polydispersity parameter δ defined as $\delta = \sqrt{\langle (r_i - 1)^2 \rangle}$

where r_i is the particle-size scaling factor. The desired polydispersity was introduced in the starting random configuration by selecting the size of each particle randomly from a Gaussian distribution with a mean $\langle r_i \rangle = 1.0$ and standard deviation $\sigma = \delta$. For each polydispersity, reported results are based on simulations for five independent initial configurations generated this way (agreement between independent runs for cubes is shown in Fig. 3.12 of the SI). The com-

pression runs were carried out in small increments of osmotic pressure value P^* with increased sampling (smaller pressure steps) near the transition points. The dimensionless osmotic pressure P^* was defined as $P^* = Pa^3/\epsilon$, where a is the radius of the circumscribing sphere (specific to each particle geometry) for a unit scaling ratio $r_i = 1$ and ϵ is an arbitrary energy parameter (set to 1). The equilibration at each pressure value is accomplished using translation, rotation and anisotropic volume moves (which for ordered phases involve changes of the simulation box volume and triclinic shape). Additional 'flip' moves[27] that attempt to rotate a chosen particle to a random orientation in a plane perpendicular to its current orientation were also used to increase configurational sampling efficiency. Each Monte Carlo cycle consists of N translation, N rotation, $N/10$ flip and 1 volume moves, where N is the total number of particles (which ranged from 1728 to 4096). All moves were accepted or rejected according to the Metropolis criterion, which in this case involves overlap checks using the separating axes theorem[28].

Each pressure run consisted of 3×10^6 Monte Carlo cycles for both equilibration and production. The equilibration at each pressure value was monitored by recording the volume fraction ϕ of the system against simulation cycles, and by checking the convergence of various orientational and translational order parameters measured for configurations periodically saved during the production runs. The phase characterization and analysis of different phases was subsequently done using various translational and orientational order parameters, mobility coefficients, and visual inspection of local order in color-coded snapshots.

The orientational order for cubes was measured using the cubatic order pa-

parameter $\langle P_4 \rangle$ defined as:

$$\begin{aligned}
 \langle P_4 \rangle &= \max_{\hat{n}} \frac{3}{14N} \sum P_4(\hat{u}_i \cdot \hat{n}) \\
 &= \max_{\hat{n}} \frac{3}{14N} \sum (35 \cos^4 \theta_i(\hat{n}) - 30 \cos^2 \theta_i(\hat{n}) + 3)
 \end{aligned}
 \tag{3.1}$$

where \hat{u}_i is the unit vector along a relevant particle axis and \hat{n} is a director unit vector which maximizes $\langle P_4 \rangle$. To find \hat{n} and the value of maximum order parameter, we used an approximate numerical recipe detailed in [7]. This recipe yields the director vectors \hat{n}_1 and \hat{n}_2 which maximize the corresponding values of order parameters $[\langle P_4 \rangle]_1$ and $[\langle P_4 \rangle]_2$ while being maximally orthogonal to each other. The orientational order for truncated octahedrons and cuboctahedrons was estimated via orientational distribution functions as described in the Supplementary Information of Ref. 6. To quantify changes in translational order we used various spherical-harmonics-based bond order parameters. The long range order was measured using the global parameters Q_4 and Q_6 proposed by Steinhardt et. al.[29], while to identify local clusters and capture the fractionation of assemblies in different coexisting solid and jammed phases, local parameters[30] $\bar{q}_4(i)$ and $\bar{q}_6(i)$ were used. Both definitions use a rotationally invariant summation over the spherical harmonics of bond vectors formed by the first neighboring shell of particles. The definitions are given by equation sets 3.2 and 3.3 respectively,

$$Q_l = \left[\frac{4\pi}{2l+1} \sum_{m=-l}^l |\bar{Q}_{lm}(\vec{r})|^2 \right]^{\frac{1}{2}}$$

with,

$$\bar{Q}_{lm} = \frac{1}{\sum_i N_b(i)} \sum_i \sum_{N_b(i)} Y_{lm}(\vec{r})$$

(3.2)

and,

$$\bar{q}_l(i) = \left[\frac{4\pi}{2l+1} \sum_{m=-l}^l |\bar{q}_{lm}(i)|^2 \right]^{\frac{1}{2}}$$

with,

$$\begin{aligned} \bar{q}_{lm} &= \frac{1}{N_b(i)} \sum_{k=0}^{N_b(i)} q_{lm}(k) \\ \bar{q}_{lm}(k) &= \frac{1}{N_b(k)} \sum_{N_b(k)} q_{lm}(k) Y_{lm}(\vec{r}) \end{aligned}$$

(3.3)

where $N_b(i)$ is the number of neighbors of particle i , identified as particles which are at a distance of less than 1.2 times the first peak distance in the radial distribution function $g(r)$, and Y_{lm} are spherical harmonics for the neighboring particles position vector \vec{r} (the angles θ and ϕ that each of such position vector makes are defined with respect to an arbitrary laboratory frame).

To explore differences in dynamic properties of the assemblies at various pressure values and to capture the jamming behavior of the particles we used a mobility coefficient D , which serves as an effective diffusion constant suitable

for Monte Carlo (MC) simulations. The coefficient is calculated by determining the rate of change of the mean squared displacements of particles measured in independent constant-density simulations of the equilibrated phase. The simulations are carried out with a fixed set of translation and rotation "pseudo dynamic" moves for which small perturbative translation and rotation step sizes are predefined (to maintain constant acceptance probabilities) based from the previous NpT simulations. This helps maintaining equivalent frequency of translational and rotational changes at various state points, such that the average extent of motion can be compared over "time" periods in units of MC cycles. The mean square displacement R_s over a pseudo time of N_s MC cycles is given by

$$R_s = \frac{\sum_{i=1}^N \sum_{j=0}^{N_{mc}-N_s} |\Delta r_{(j+s,j)}^i|^2}{N(N_{mc} - N_s)} \quad (3.4)$$

where $\Delta r_{j+s,s}^i$ is the displacement of the centre of mass of i^{th} particle between the j^{th} and $(j + s)^{th}$ MC cycle and N_{MC} is the total number of cycles in the MC simulation.

To better characterize the translational order in systems with cubic order, we developed a new order parameter, which is similar in spirit to the Lindemann parameter[31]. This new parameter measures average deviation of particle positions from the best-fit set of lattice points defined with respect to individual particle positions, director vectors \hat{n}_1 and \hat{n}_2 (calculated from maximizing the cubic order parameter $\langle P_4 \rangle$)[7] and the optimal lattice spacing d (obtained from the first peak of the radial distribution function $g(r)$). The parameter is defined

as:

$$\Delta_{global}^2 = \min_i \frac{1}{N} \sum_{j=1}^N \min_k (\vec{r}_j - \vec{r}_{i,k}^{ref})^2$$

$$\vec{r}_{i,k}^{ref} = r_i \pm d\{k_1 \hat{n}_1 + k_2 \hat{n}_2 + k_3 \hat{n}_3\} \quad (3.5)$$

where $\hat{n}_3 = \hat{n}_1 \times \hat{n}_2$ and $k_1, k_2,$ and k_3 are integers. The \vec{r}_j 's are position vectors of the instantaneous particle positions in a given configuration while $\vec{r}_{i,k}^{ref}$ is the k^{th} lattice point defined with respect to the i^{th} particle along the three possible director vectors. The first minimization is to find the nearest lattice point for particle j among the various possible reference lattice points $\vec{r}_{i,k}^{ref}$'s. The second minimization is to find the particle i which gives most appropriate lattice vectors defined along orientation of particle i . Note that smaller Δ_{global}^2 values correspond to the most ordered states and that one could rescale it to reverse this behavior or to make it be bound between 0 and 1. Another global positional order parameter often employed [25] was also measured by averaging values over all the particles and several configurations:

$$\langle G_{global} \rangle = \left| \frac{1}{N} \sum_i \exp(iK \cdot \vec{r}_i) \right| \quad (3.6)$$

where, K is a reciprocal lattice vector of the crystal under consideration (calculated by using the \hat{n}_1 and \hat{n}_2 director vectors). It can be argued that while Eq. (3.6) and other similar global order parameters capture the regularity of the "average" particle positions, the order parameter (3.5) gives instead a sense for the "variance" of the particle positions around their mean values.

3.4 Results and Discussions

Perfect monodisperse cubes were reported to have a liquid crystalline "cubatic" mesophase at conditions near the order-disorder transition ($0.51 \leq \phi < 0.54$), characterized by high orientational order, layering along the three directors (indicative of at least intermediate-range translational order), and finite long time translational mobility[6]. A recent study for the same system concludes that the positional ordering near the bulk coexistence regime is long-ranged and indicative of a simple cubic crystal phase but with an unusually high amount of "delocalized" vacancy content ($\sim 6.4\%$)[26] which is about 3 orders of magnitude larger than that for typical crystals near the melting transition). While we had also previously quantified and detected significant translational order in such a phase[6], the finite system sizes did not allow us to ascertain its long-range character and hence the "cubatic" phase designation was adopted based on the dynamic criterion that considers its liquid-crystal-like particle mobility. We have now tried to reassess the positional order in such an unusual phase by performing *NVT* simulations for 8000 cubes at 10 different volume fraction values between $\phi = 0.3$ and $\phi = 0.8$. For the ordered systems, care was taken to ensure that the particle orientation directors had minimal rotation with respect to the cubic box axes. The equilibrated configurations were used to calculate orientational order using $\langle P_4 \rangle$ and translational order using Δ_{global}^2 and $\langle G_{global} \rangle$ as described in the Methods' Section.

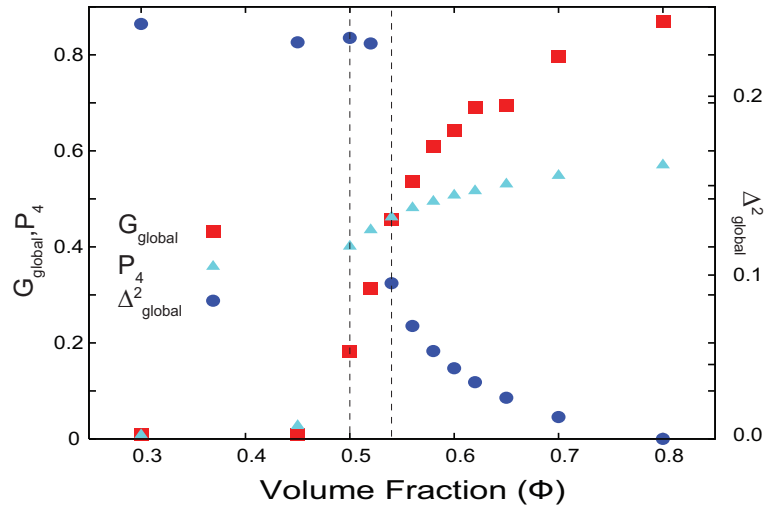


Figure 3.2: Different translational and orientational order parameters for assemblies of 8000 cubes at various volume fractions (obtained by sampling over 200 independent configurations from constant density simulations). Dashed lines enclose region of putative cubatic phase character.

For a system of 8000 cubes the ordered phase was estimated[26] to form first at $\phi = 0.5$ (a value slightly overestimated in [6] due to the smaller sizes used there and the expected finite-size effect). The results reported in Fig. 3.2 indicate that while the orientational order $\langle P_4 \rangle$ does nucleate at $\phi = 0.5$, the translational order shows a transition to solid-like values at a slightly higher densities around $\phi = 0.54$. In particular, the Δ_{global}^2 value for $\phi = 0.52$ is similar to that of an isotropic phase ($\Delta_{global}^2 = 0.23$) and about an order of magnitude larger than that for $\phi = 0.54$. This happens because $\langle G_{global} \rangle$ is a sensitive probe that detects and penalizes any transient shifts of the particle positions from their ideal lattice positions. Moreover, efforts to calculate the Lindemann parameter[31] at most of the state points (for $\phi < 0.6$) lead to large and inconsistent values as there is finite diffusion of particles indicative of liquid-like or melting behavior with respect to translational order. These results suggest that, at least for $\phi = 0.5$ and 0.52 , the phase formed is sufficiently distinct from a cubic crystal and its classification will be contingent to the criteria or threshold order parameter value adopted: while the particles adopt positions which are in average somewhat consistent with a cubic crystal (as given by the intermediate $\langle G_{global} \rangle$ values), the variance of their position fluctuations (as given by Δ_{global}^2) is liquid-like.

The effect of polydispersity in the system of cubes is investigated by performing compression runs for 1728 and 4096 cubic particles with quenched size polydispersities varying from $\delta = 0.02$ to 0.30 , where δ is the standard deviation of the Gaussian distribution of particle sizes (larger systems were used for larger δ to accommodate a representative sample of particle sizes). The single-phase equation of state (EOS) curves obtained by the compression runs are plotted for the monodisperse system ($\delta = 0$) and for systems with 5 distinct δ values in the middle frame of Fig 3.3. These are apparent EOS curves as they would refer

to metastable single-phase states in cases when the parent phase can fractionate. The curves show a density gap associated with the first order transition until a critical polydispersity value of $\delta_i = 0.18$, after which the transition becomes continuous, suggestive of a translationally jammed state (as observed in spheres[12]).

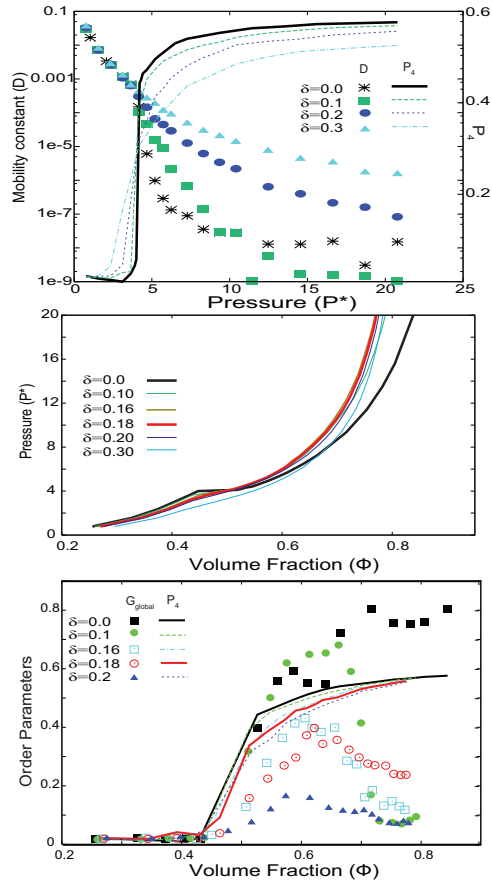


Figure 3.3: Polydisperse cubes for $0 \leq \delta \leq 0.3$. Top: Mobility coefficients (D) and cubatic orientational order parameter $\langle P_4 \rangle$ vs. pressure. Middle: Equation of state curves showing overlap and no first-order transition density gap for $\delta \geq 0.18$. Bottom: Translational ($\langle G_{global} \rangle$) and orientational ($\langle P_4 \rangle$) order parameters vs. volume fraction ϕ ; the peak in $\langle G_{global} \rangle$ around $\phi = 0.6$ indicates conditions that favor structures with cubic symmetry.

Moreover, the high-density branches of the EOS curves tend to shift left with increasing δ (signaling less efficient packing for a given pressure), and for $\delta \geq 0.18$ show significant overlap with each other, converging toward a packing fraction of $\phi \sim 0.83$ (at $P^*=103.9$) for most systems. Surprisingly, the low-density "isotropic" branches shift slightly to the right with δ , suggesting a more efficient packing for a given pressure. The mobility coefficient D and the orientational order parameter $\langle P_4 \rangle$ are plotted against the reduced pressure P^* in the top frame of Fig. 3.3 for $\delta = 0, 0.10, 0.20$ and 0.30 . For $\delta = 0.0$ and $\delta = 0.10$, the decay behavior of D shows a transition at $P^*=4.2$, with the higher density branch decaying to very low D values with pressure. For $\delta = 0.20$ and 0.30 , the decay behavior is smoother and the curves plateau (at high pressures) at a value two to three orders of magnitudes higher than that for $\delta = 0.10$, consistent with the notion that diffusion should be larger in systems with less positional order. However, the orientational order parameter $\langle P_4 \rangle$ shows almost perfect alignment for all δ values when $P^* > 4.2$ (top and bottom frames of Fig.3.3). Further, the $\langle G_{global} \rangle$ values (bottom frame of Fig. 3.3) show a non-monotonic dependence with volume fraction ϕ for different polydispersities. While for the monodisperse and low- δ systems the $\langle G_{global} \rangle$ parameter increases mostly monotonically with ϕ , for $\delta \sim 0.10 - 0.20$ it shows a distinct "broad" peak around $\phi \approx 0.6 - 0.63$. This peak is indicative of the fact that there is an optimal window of ϕ where the system is sufficiently packed for particles to orientationally align but has still enough free volume to best accommodate polydisperse cubes on a cubic lattice. Once ϕ goes above this window, then the entropic penalty to sustain a cubic translational order becomes too large for a high- δ system, as it approaches a densest packing state where particles must cram into off-lattice positions. It can also be observed that the peak narrows and drops to lower $\langle G_{global} \rangle$ values with increas-

ing δ , disappearing for $\delta > \delta_c(\sim 0.18)$. These high- δ assemblies result in a novel orientationally-ordered high density ($\phi \sim 0.83$) jammed (glass-like) phase.

The local translational order in polydisperse cubes at different state points is analyzed via color-coded snapshots, where each particle is ascribed a color from red to green based on the range of its local bond orientational parameter values $\bar{q}_4(i)$ in going from 0 to q_4^{max} (see Methods). The snapshots shown in Fig. 3.4 for $\delta = 0.18$ and 0.20, show signs of spatial fractionation of particles into solid-like and liquid-like domains (with inhomogeneous size distribution of particles). The jamming behavior at higher densities is noticeable for $\delta = 0.20$ in the form of a high amount of heterogeneities in the local bond order spatial distribution. The growing extent of heterogeneity in such high- δ systems correlates with the increasing trend observed in the D plateau values with δ (shown in Fig. 3.3), where the liquid-like domains likely become the dominant contributors to the higher mobilities.

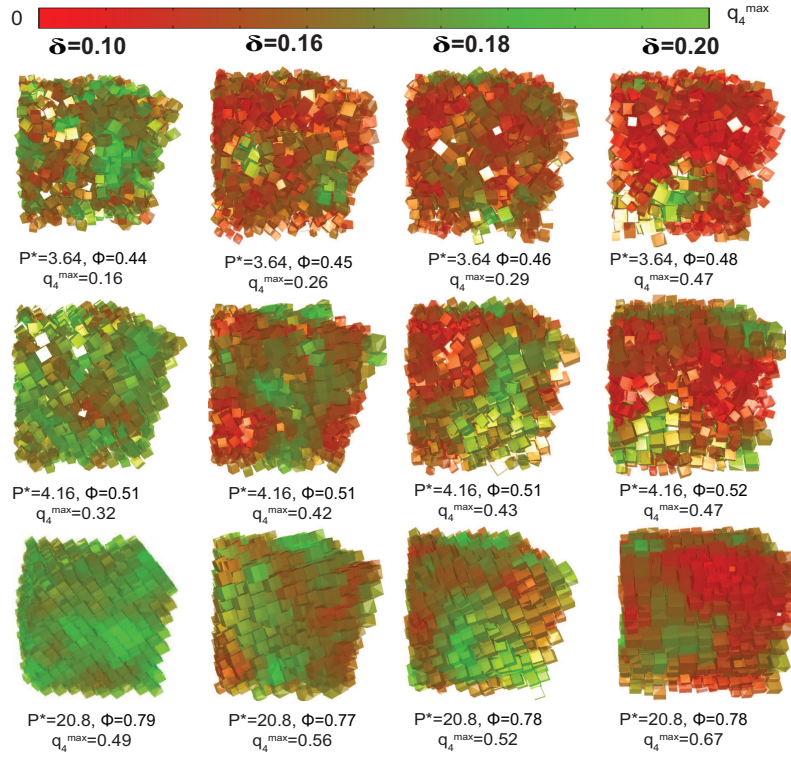


Figure 3.4: Snapshots for cubes at various pressure state points (around the order-disorder transition points, which is significantly different for higher δ systems and higher pressures) for $\delta = 0.10, 0.16, 0.18$ and 0.20 . The particles are color coded from red to green, depending on their local bond orientational order parameter value $\bar{q}_4(i)$.

Monodisperse truncated octahedrons form a plastic crystalline mesophase for $0.52 < \phi < 0.70$. The nucleation of translational order for this shape precedes that of orientational ordering; hence the effect of introducing polydispersity in these systems is expected to be similar to that for spheres. The apparent EOS curves obtained from compression runs for the monodisperse system ($\delta=0$) and systems with 8 different δ values are plotted in the bottom frame of Fig. 3.5. The leftward shift of the solid branches with increasing δ , as in the case of polydisperse cubes, signals the gradual loss of the space-filling ability of the particles. The first order density gap (separating the isotropic and rotator phases) narrows, disappearing at a critical polydispersity value of $\delta_c \approx 0.14$, above which the curves overlap with each other converging toward a packing fraction of $\phi = 0.73$ (at $P^* = 22.4$). The curves for D and the global bond orientational order parameter Q_6 for $\delta = 0, 0.10, 0.20$ and 0.30 , are plotted against the reduced pressure P^* in the top frame of Fig 3.5. For $\delta = 0$ and 0.10 , the D curve shows a transition at around $P^* = 3.9$, with mobilities decaying to very low values consistent with a crystalline phase at high pressures. For $\delta = 0.20$ and 0.30 , the rapid transition in the mobility values disappears, showing instead a continuous slowing down of the dynamics with increasing pressure, with a jamming plateau at mobility values which are three order of magnitudes higher than that for $\delta = 0.10$. For $\delta = 0$ and 0.10 , the Q_6 parameter that measures the amount of translational order in the system shows a sudden transition at $P^* \approx 3.9$ with values converging to $Q_6 \approx 0.5$ and 0.46 , respectively. For $\delta = 0.20$ and 0.30 , the Q_6 values transition over a wider range of pressure values (above $P^* = 3.9$) and converge to much lower values (around 0.14 and 0.09 respectively). Both D and Q_6 hence suggest formation of a glass-like state for systems with $\delta > 0.14$, characterized by diminishing bond orientational order and slower dynamics (though much higher than the

crystalline solid). Orientational order was estimated by plotting orientational distribution functions [6] as shown for selected δ and pressures in Fig. 3.11(a) of the SI. These functions show that systems with higher δ have less orientational order whether one compares systems at the same pressure or at the same volume fraction; hence, states having limited orientational order consistent with rotator crystals have a higher upper bound in P^* (and ϕ) as δ increases.

To investigate the local ordering and fractionation tendencies at various state points of these polydisperse systems, snapshots with particles color-coded according to their local bond order parameter $\bar{q}_6(i)$ are shown in Fig. 3.6. The sequence of structures formed around the coexistence point $P^* = 3.91$ indicates localized fractionation of the system into coexisting solid- and liquid-like domains above the critical polydispersity value of $\delta_c = 0.14$, whereas for hard spheres fractionation into multiple solid phases is reported to occur at polydispersity values of $\delta_c \approx 0.07$ [13]. Note also that the fraction of highly ordered (orientationally and translationally) coexisting solid domains decreases with δ , with negligible crystalline content for $\delta \approx 0.30$.

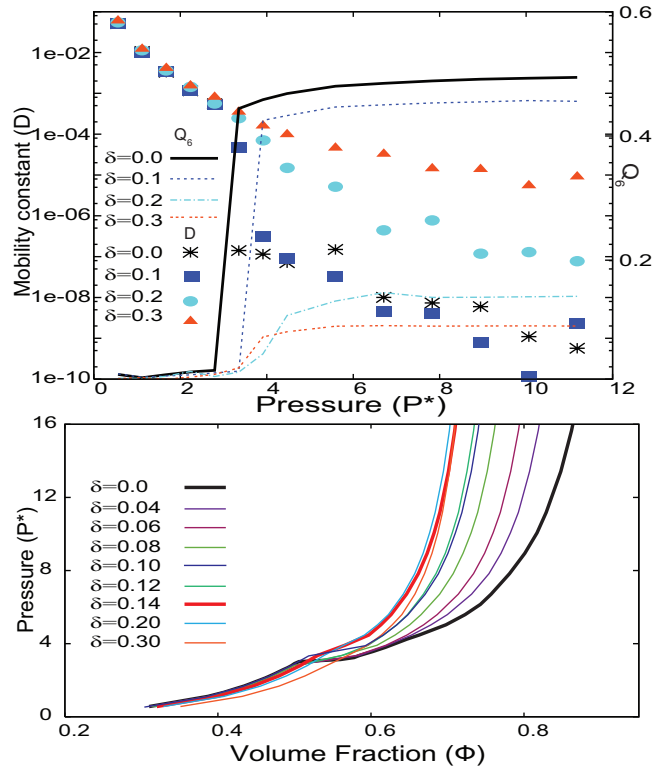


Figure 3.5: Polydisperse truncated octahedrons with $0 \leq \delta \leq 0.3$. Top: Mobility coefficients (D) and global bond orientational order parameter Q_6 plotted against pressure. Bottom: Equation of state curves showing overlap and no first order transition density gap for $\delta \geq 0.14$.

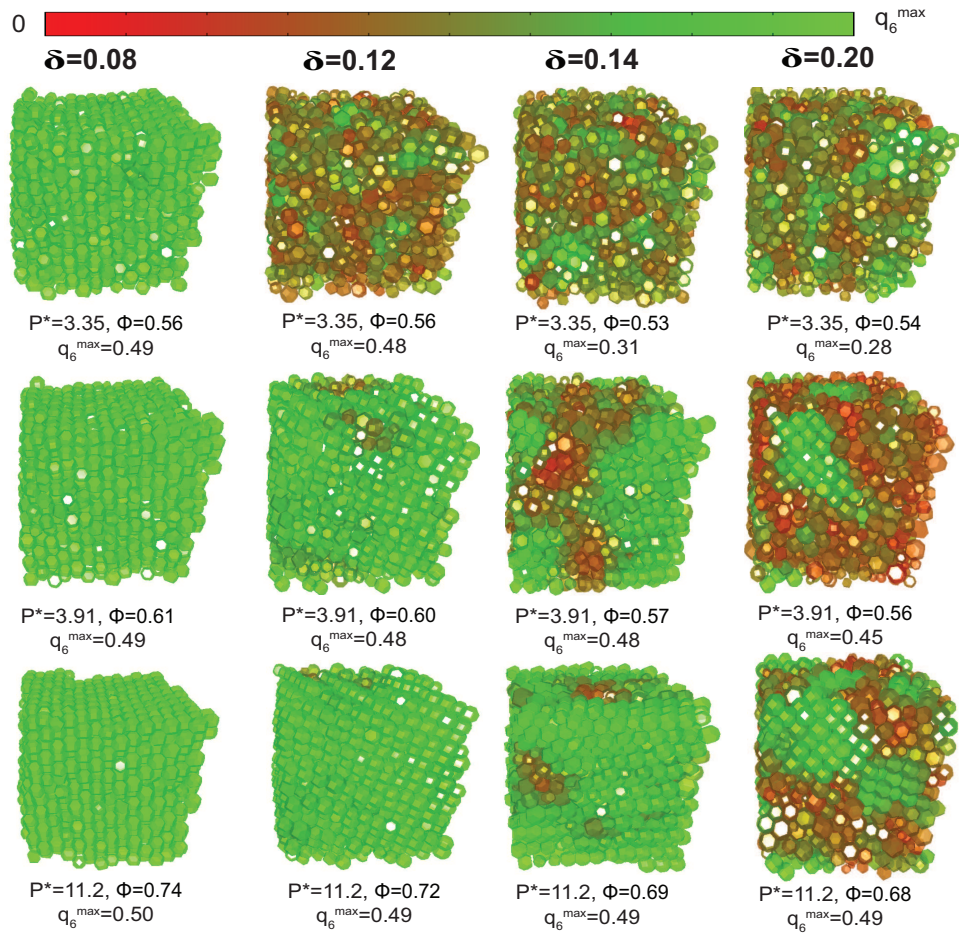


Figure 3.6: Equilibrated snapshots for truncated octahedrons at various pressure state points (around the order-disorder transition and higher pressures) for $\delta = 0.08, 0.12, 0.14$ and 0.20 . The particles are color coded from red to green, depending on their local bond orientational order parameter value $\bar{q}_4(i)$.

Monodisperse cuboctahedrons (which have a non space-filling densest packing) exhibit two first-order phase transitions (instead of one as in truncated octahedrons) at around $P^*=4.0$ and $P^*=5.4$, separating the branches for the isotropic, rotator and crystal phases (see Fig. 3.10 in the SI). The apparent single-phase EOS curves obtained from compression runs for the monodisperse case and for systems with 6 different δ values are shown in the bottom frame of Fig 3.7. The EOS curves shift to the left with increasing polydispersity, with the rotator-crystal first order transition disappearing at $\delta=0.04$ and with the isotropic-rotator transition disappearing for $\delta \geq 0.08$, where all the high-density branches overlap and converge to a packing density of 0.70 (for $P^*=33.9$). The values of D and the global bond orientational order parameters Q_6 are plotted against pressure P^* for $\delta = 0.0, 0.06$ and 0.12 in the top frame of Fig. 3.7 (bond orientational plots for $\delta \leq 0.06$ are shown in Fig. 14 in the SI). While for $\delta = 0.0$ and 0.06 the D curves exhibit a rapid decay behavior (at around $P^* \sim 6.7$), for $\delta = 0.12$ the decay behavior becomes much more gradual throughout. Moreover, the curve for Q_6 also shows a step-wise increase (rising from ~ 0.0 to 0.5) at $P^* \sim 6.7$ for the $\delta = 0.0$ and 0.06 systems, while no increase whatsoever is observed for the $\delta = 0.12$ system. The color-coded snapshots (colors ascribed based on the value of local bond orientational order parameter $\bar{q}_6(i)$) are shown in Fig. 3.8 at selected pressure state points for the $\delta = 0.06$ and 0.08 systems. While the $\delta = 0.06$ configurations at high-pressure values show a single crystal phase, the $\delta = 0.08$ configurations show particles jamming in a state with no prominent long range or local order. As with truncated octahedrons, the orientational distribution functions for polydisperse cuboctahedrons [see Fig. 3.13(b) in the SI] show that systems with higher δ have less orientational order for either the same P^* or the same ϕ (with the $\delta = 0.08$ system never attaining any minimal extent of

orientational order).

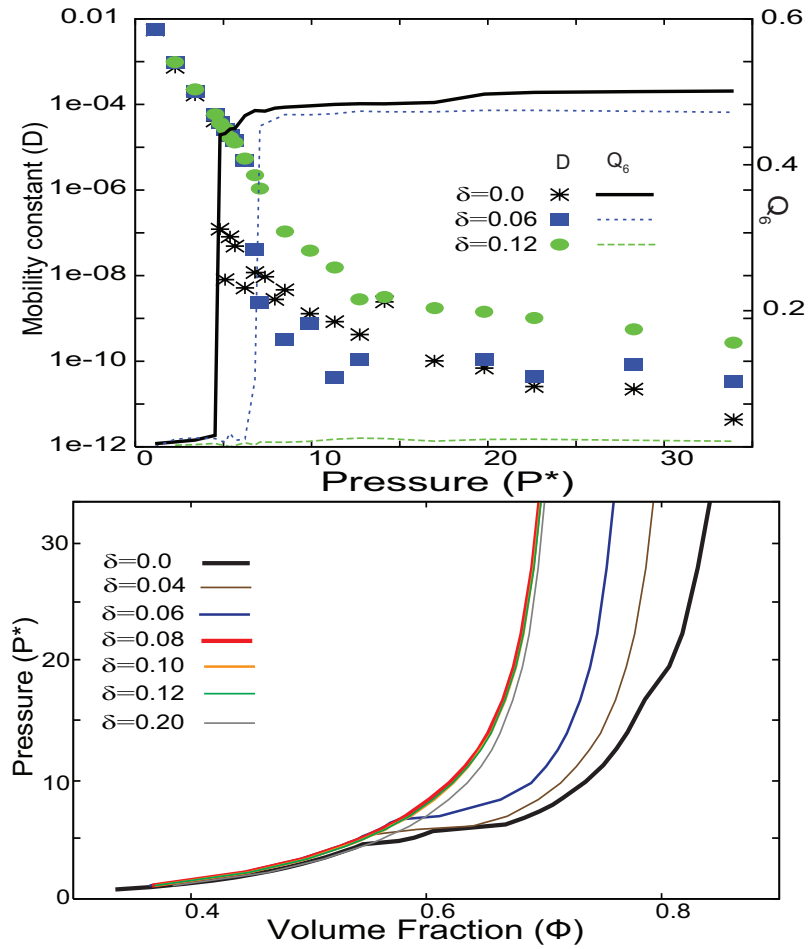


Figure 3.7: Polydisperse cuboctahedrons for $0 \leq \delta \leq 0.20$. Top: Mobility coefficients (D) and global bond orientational order parameter Q_6 plotted against pressure for $\delta = 0.0$ (reference lines), 0.06 and 0.12. Bottom: Equation of state curves showing overlap and have no first order transition density gap for $\delta \geq 0.08$.

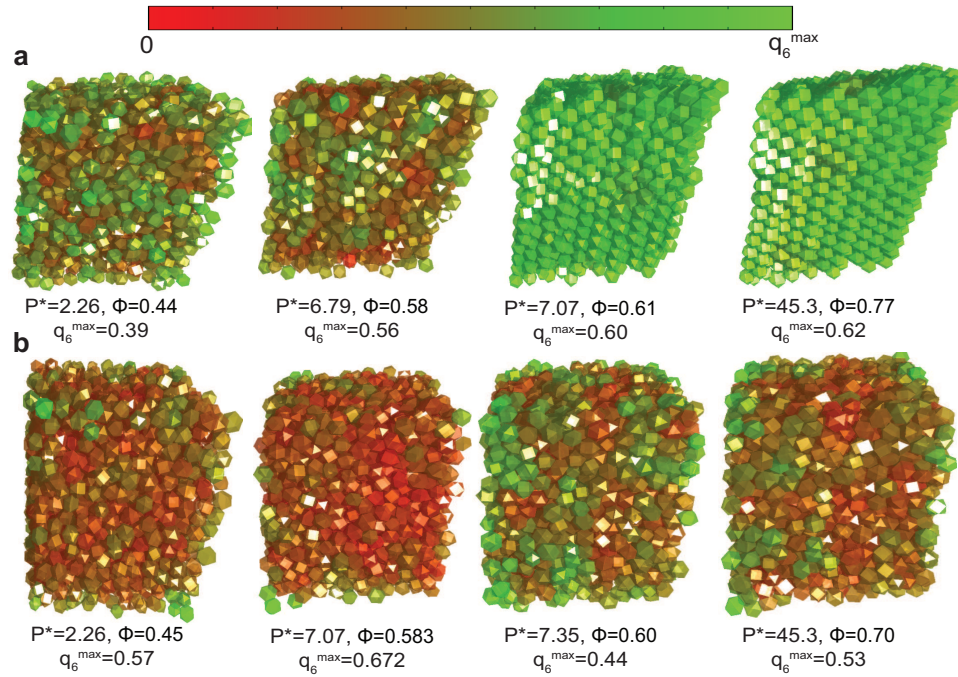


Figure 3.8: Snapshots for cuboctahedrons at various pressure state points (around the order-disorder transition and higher pressures) for a) $\delta = 0.06$ and b) 0.08 . The particles are color coded from red to green, depending on their local bond orientational order parameter value $\bar{q}_4(i)$.

Overall, compared to truncated octahedrons, cuboctahedrons have a behavior more similar to that of hard spheres which also undergo a jamming transition at $\delta_c = 0.08$ into a glassy state with no fractionation into coexisting solid phases[13]. This is unexpected since it is the truncated octahedrons that have an asphericity value (1.291) that is closer to that of spheres (1.0) than cuboctahedrons (1.414). However, a key feature appears to be that cuboctahedrons, like spheres and unlike (monodisperse) truncated octahedrons, do not tessellate space. The stronger entropic bonding associated with a space-filling polyhedron seems to provide added resilience to the structural order and better tolerance of the perturbations in regular packing brought about by size polydispersity. This is further reflected in the fact that for $\delta = 0.08$, for example, cubes and truncated octahedrons can attain denser (more efficient) packing with less jamming than cuboctahedrons at comparable high pressures.

3.5 Conclusions

The introduction of quenched size polydispersity has vastly different effects on the phase behavior (at low δ values) and dynamic arrest behavior (for high δ values) of polyhedrons with different geometries. For cubes, which exhibit an orientational ordering transition before translational ordering upon increasing concentration, the orientational order is preserved even at very high polydispersities. This leads to the formation of a novel orientationally aligned but translationally jammed high-density glassy phase. Truncated octahedrons and cuboctahedrons, which undergo translational ordering before orientational ordering with increasing concentration, form jammed states at lower packing densities and with no long-range orientational or translational order. It can be con-

jectured that the type of order (orientational or translational) that ensues first upon compression gives an indication of the dominant entropic force driving the ordering of a particular type of polyhedron and hence it will be the most resilient to fight back the disordering effect of increasing size polydispersity. To a first approximation, increasing size polydispersity has an effect that is opposite to that of increasing concentration in the monodisperse system, mainly because increasing δ weakens the packing entropy that drives order, resulting in reduced equilibrium packing fraction of the mesophase or crystal for a given pressure. Quenched polydispersity also enhances the range of conditions (e.g., pressures) where the mesophase in the monodisperse system occurs; i.e., in the limit where δ is at or slightly below δ_i , the entire ordered branch of the equation of state could be said to be a mesophase (a cubatic-like state for cubes and a "rotator" solid with limited orientational order for the truncated octahedrons and cuboctahedrons).

Cubes and truncated octahedrons, which are space filling when monodisperse, have a significantly larger critical polydispersity δ_i (above which translational order tends to vanish) than the non-space filling cuboctahedrons. This difference is especially meaningful in comparing truncated octahedrons and cuboctahedrons which exhibit a very similar monodisperse phase behavior. It can be argued that space-filling polyhedrons encode a stronger entropic driving force toward ordering and can hence better counter the "disordering" effect of polydispersity. Furthermore, cubes and truncated octahedrons have a stronger tendency than cuboctahedrons to fractionate into small solid like clusters coexisting with disordered fluid or glassy phase (at higher pressures) for polydispersity values right above δ_i . This difference in behavior can again be ascribed to the stronger driving force to pack efficiently when a cluster of similarly sized

particles of nearly space-filling geometry are in proximity; it is unclear, however, whether such local fractionation may lead to macro-phase segregation. Altogether, these observations support the tenet that space-filling polyhedrons are ideal candidates to form robust self-assembled structures[6] and would be well suited to tolerate particle size imperfections in real systems.

Regarding the ordering behavior of monodisperse cubes, our analysis suggests that a system at conditions around the $\phi = 0.52$ density constitutes a truly unusual state of matter that challenges our conventions for the classification of crystals and liquid crystals. Whether one should call it a "liquid-crystal with an unusually high positional order" or a "crystal with unusually high delocalized-vacancy content and particle mobility" seems a semantic issue that should underscore the unique nature of such a phase.

The present study constitutes a first step toward a road map that elucidates and catalogs all the possible effects that size polydispersity may have on the phase and dynamic arrest behavior of polyhedral assemblies. In this context, it is pointed out again that macrophase fractionation states are precluded in these simulations. For small δ values, it is expected that fractionation (from a fixed parent δ) will only occur in a very narrow range of pressures around phase transitions and hence the single-phase behavior simulated here captures thermodynamic behavior. For large δ (certainly above δ_i) single-phase states will likely be metastable over broad ranges of pressures (and densities). The mapping of two-phase states is the object of our ongoing studies, and entails the use of either much larger system sizes with special moves to accelerate particle diffusion, or two-box ensemble methods[11, 14]. Our purpose for probing such a broad range of quenched polydispersity values in this work was mainly to obtain approx-

imate polydispersity thresholds where structural order and mobility showed marked changes relative to the monodisperse system behavior. Also, the heterogeneous states described here are relevant to real experiments when dense states are reached at a rate faster than the slow diffusion-driven phase segregation. Further studies exploring the effects of different types of polydispersity (e.g., interpolating between two polyhedral 'shapes', or in anisotropy where distortion occurs along a particular particle axis) and more detailed calculations with semi-grand type of ensembles for size polydisperse systems[11, 14] should provide a more detailed and thorough understanding of the self-assembly process of these highly functional polyhedral nanocrystals.

3.6 Acknowledgement

This work was supported by the U.S. National Science Foundation Grant No. CBET 1033349 (in relation to polyhedral phase behavior), and by the U.S. Department of Energy, Office of Basic Energy Sciences, Division of Materials Sciences and Engineering under award Grant No. ER46517 (in relation to dynamical glassy behavior). The authors gratefully acknowledge helpful discussions with Prof. Tobias Hanrath.

3.7 Supplementary Information

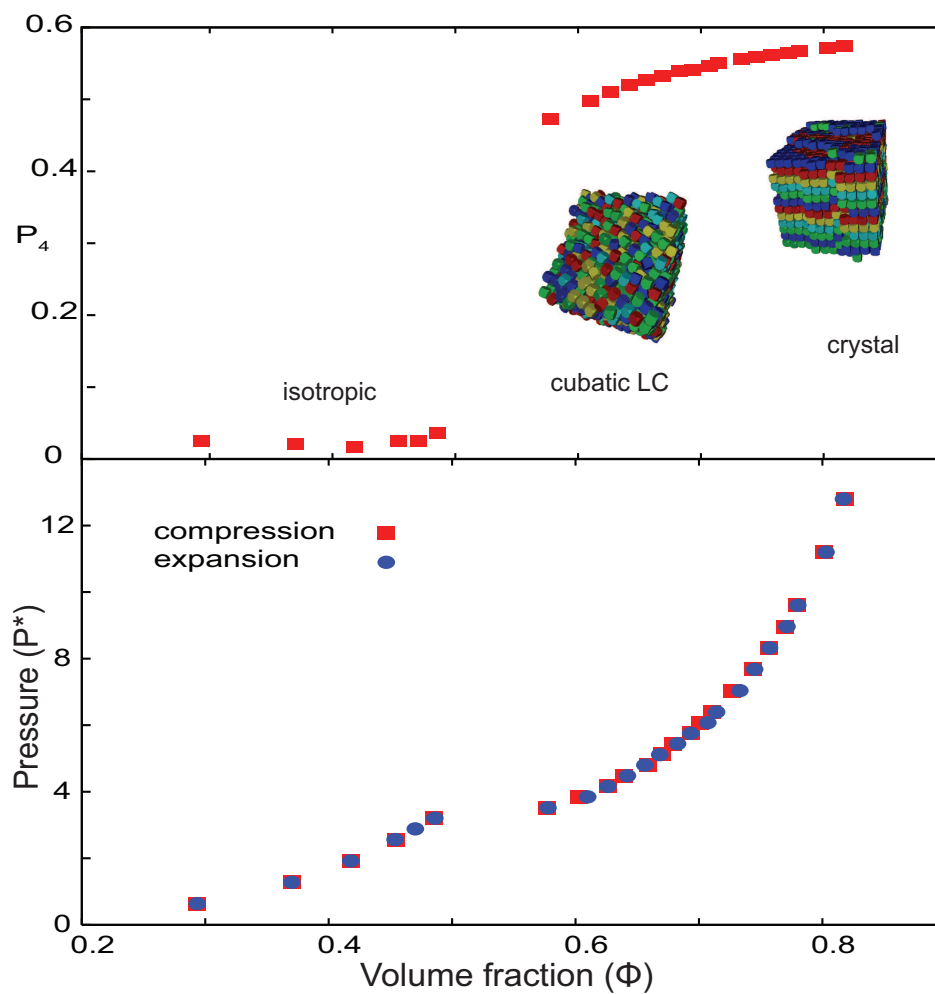


Figure 3.9: Phase behavior of monodisperse truncated cubes. Top: Orientational order parameter (P_4) and snapshots illustrating the presence of a cubatic-like LC phase in between the crystal and isotropic phases. Bottom: Equation of state from expansion and compression runs.

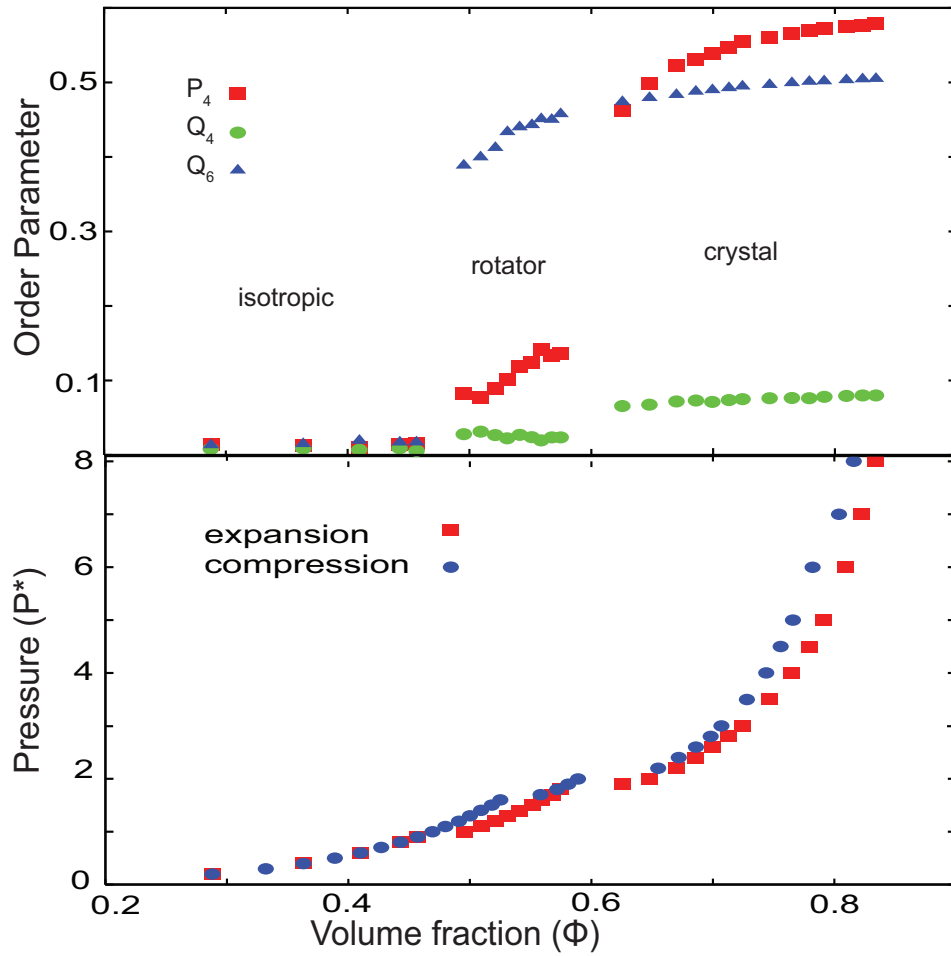


Figure 3.10: Phase behavior of monodisperse cuboctahedrons. Top: Translational (Q_4 and Q_6) and orientational (P_4) order parameters from expansion runs. Bottom: Equation of state from expansion and compression runs, showing two first-order transitions separating the crystalline, rotator and isotropic phases.

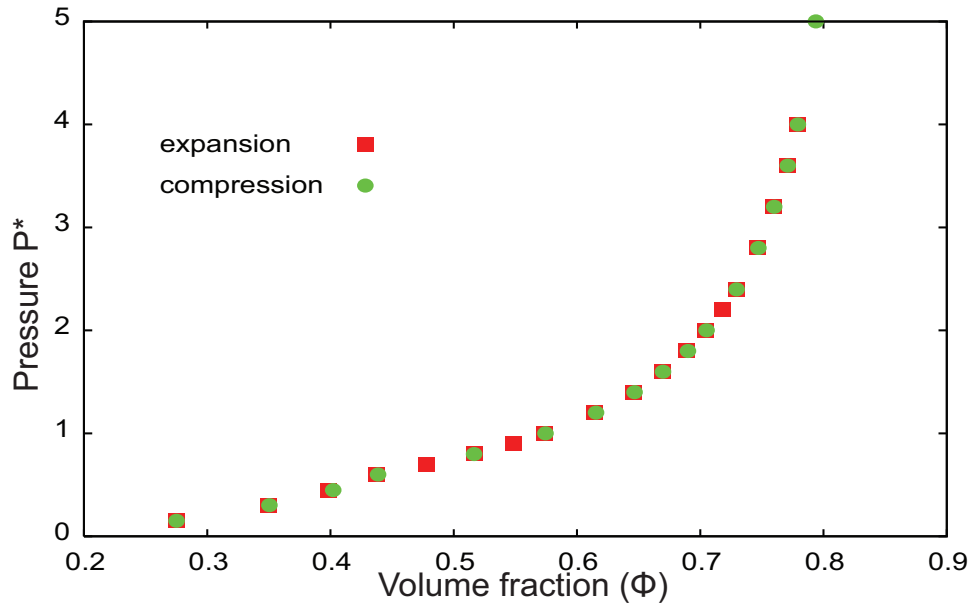


Figure 3.11: Equation of states from expansion and compression for poly-disperse cubes for $\delta \sim 0.20 (> \delta_t)$. The curves overlap each other pretty closely indicating absence of any hysteresis in the translational jamming behavior.

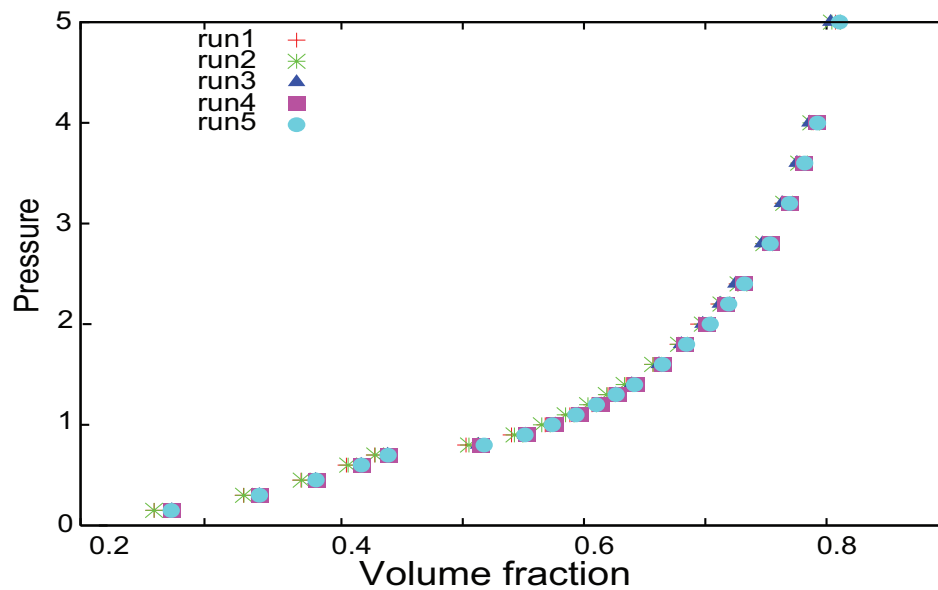


Figure 3.12: Equation of state curves for polydisperse cubes with $\delta \sim 0.10$ from different initial Gaussian size distribution configurations. The close agreement among curves indicates that the system size used (1728 particles) is sufficiently large to properly sample polydispersity effects.

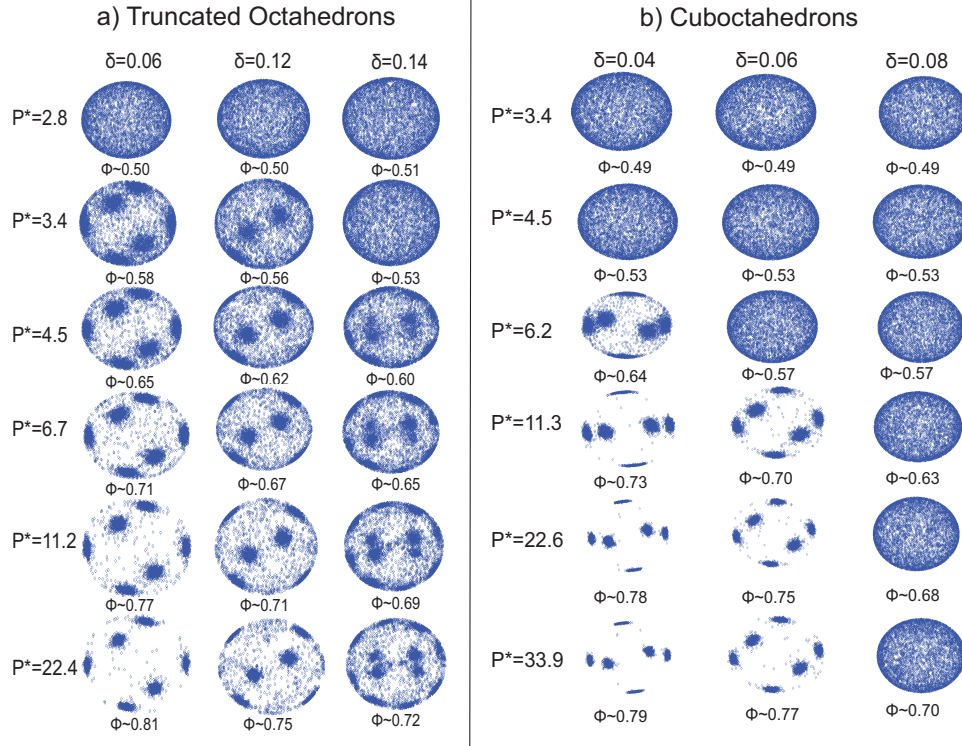


Figure 3.13: Orientational distribution functions for polydisperse (a) truncated octahedrons and (b) cuboctahedrons at different pressures (P^*) and volume fractions (ϕ); the dots show the orientation of the unit vectors perpendicular to the square facets so that the most clustered they are the highest the extent of orientational order. In all cases, systems with higher polydispersity (δ) have less orientational order for either the same pressure or the same volume fraction. As an example, for the truncated octahedrons a similar rotator-like order occurs for $\{\delta, P^*, \phi\} = \{0.06, 3.4, 0.58\}$, $\{0.12, 4.5, 0.62\}$, and $\{0.14, 11.2, 0.69\}$. Note that the approximate range of occurrence of the rotator phase for the monodisperse systems is $P^* = 2.5-4.5$, $\phi = 0.52-0.70$ for truncated octahedrons and $P^*=4.0-5.4$, $\phi = 0.5-0.58$ for cuboctahedrons.

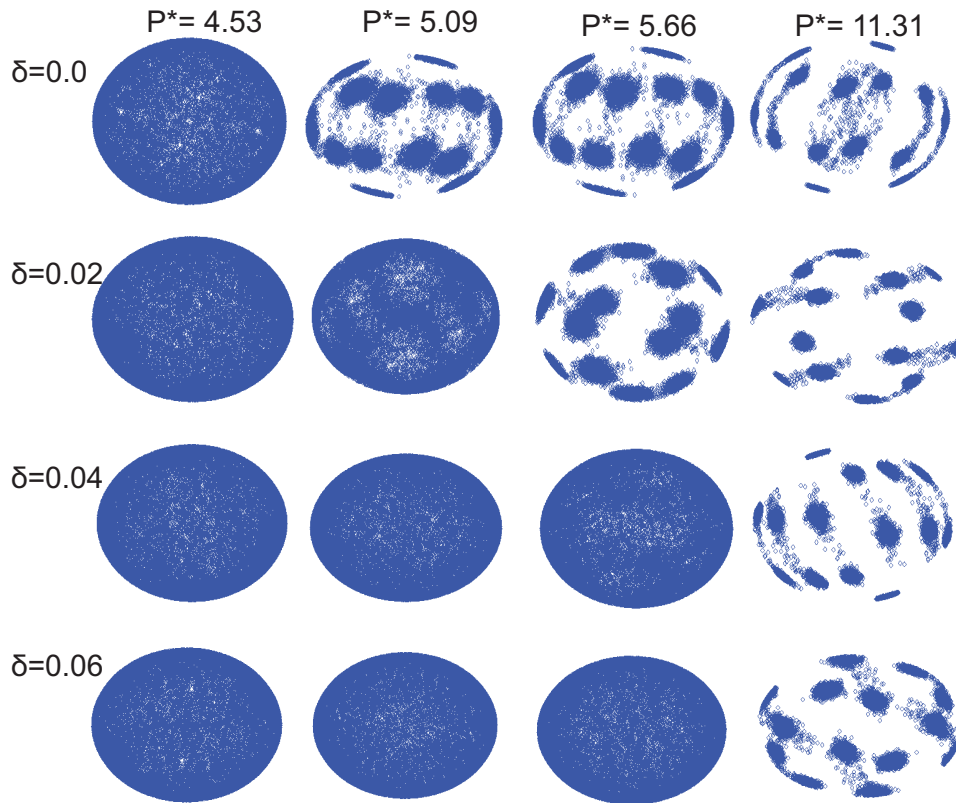


Figure 3.14: Bond orientational order diagrams for monodisperse ($\delta = 0.0$) and polydisperse ($\delta = 0.02, 0.04$ and 0.06) cuboctahedrons. The ordered states have distorted BCC symmetry, while on reducing pressure the peaks become more diffuse due to higher vibrational freedom at these lower densities. On increasing polydispersity, bond orientational order decreases; i.e., it is lost for $\delta = 0.04$ and 0.06 at $P^* = 4.53$ and the peaks are more diffuse at the higher pressures.

BIBLIOGRAPHY

- [1] Xia, Y., Xiong, Y., Lim, B., Skrabalak, S.E. (2009) Shape-Controlled Synthesis of Metal Nanocrystals: Simple Chemistry Meets Complex Physics. *Angew. Chem. Int. Ed.* 48, 60.
- [2] Sun, Y.G. and Xia, Y.N. (2002) Shape-controlled synthesis of gold and silver nanoparticles. *Science* 298, 2176-2179.
- [3] Sun, S., Murray, C.B., Weller, D., Folks, L. and Moser, A. (2000) Monodisperse FePt nanoparticles and ferromagnetic Fe Pt nanocrystal superlattices. *Science* 287, 1989.
- [4] Torquato, S. and Jiao, Y. (2009) Dense packings of the Platonic and Archimedean solids. *Nature* 460, 876-879.
- [5] Bian, K.F., Choi, J.J., Kaushik, A., Clancy, P., Smilgies, D.M. and Hanrath, T. (2011) Shape-Anisotropy Driven Symmetry Transformations in Nanocrystal Superlattice Polymorphs. *ACS Nano* 5, 2815-2823.
- [6] Agarwal, U. and Escobedo, F.A. (2011) Mesophase behavior of polyhedral particles. *Nature Materials* 10, 230-235.
- [7] John, B.S. and Escobedo, F.A. (2008) Phase behavior of colloidal hard perfect tetragonal parallelepipeds. *J. Chem Physics* 128, 044909.
- [8] Burda, C., Chen, X., Narayanan, R., El-Sayed (2005) Chemistry and properties of nanocrystals of different shapes. *Chem. Rev.* 105, 1025.
- [9] Salzemann, C., Lisiecki, I., Brioude, A., Urban, J. and Pileni, M.P. (2004) Collections of copper nanocrystals characterized by different sizes and shapes: Optical response of these nanoobjects. *J. Chem. Physics* 108, 13242.
- [10] Legrand, J., Ngo, A.T., Petit, C. and Pileni, M.P. (2001) Domain shapes and superlattices made of cobalt nanocrystals. *Adv. Mater.* 13, 58.
- [11] Kofke, D.A. and Bolhuis, P.G. (1999) Freezing of polydisperse hard spheres. *Phy. Rev.* 59, 618.
- [12] Nogawa, T., Ito, N. and Watanabe, H. (E2010) Dynamical study of a polydisperse hard-sphere system. *Phys Rev* 82, 021201.

- [13] Fasolo, M. and Sollich, P. (2003) Equilibrium phase behavior of polydisperse hard spheres. *Phys Rev Letters* 91, 068301.
- [14] Escobedo, F.A. (2003) Lyotropic isotropic-nematic transitions in polydisperse chain systems: A simulation study. *J Chem Phy* 118, 10262.
- [15] Dijkstra, M., Frenkel, D. and Hansen, J-P. (1994) Phase separation in binary hard-core mixtures. *J Chem Phy* 101, 3179.
- [16] Buhot, A. and Krauth, W. (1998) Numerical solution of hard-core mixtures. *Phy Rev Lett* 80, 3787.
- [17] Cuesta, J.A. (2002) Elusiveness of fluid-fluid demixing in additive hard-core mixtures. *Phy Rev Lett* 89, 145701.
- [18] Seo, D., Park, J.C. and Song, H. (2006) Polyhedral gold nanocrystals with O-h symmetry: From octahedra to cubes. *J. Am.Chem Soc* 128, 14863-14870.
- [19] Compton, O.C. and Osterloh, F.E. (2007) Evolution of size and shape in the colloidal crystallization of gold nanoparticles. *J. Am.Chem Soc* 129, 7793-7798.
- [20] Kim, D.Y., Im, S.H., Park, O.O. and Lim, Y.T. (2010) Evolution of gold nanoparticles through Catalan, Archimedean, and Platonic solids. *Cryst. Eng. Comm.* 12, 116-121.
- [21] Cao, Y., Jin, R. and Mirkin, C.A. (2002) Nanoparticles with Raman spectroscopic fingerprints for DNA and RNA detection. *Science* 297, 1536.
- [22] Moore, B.D., Stevenson, L., Watt, A., Flitsch, S., Turner, N.J., Cassidy, C. and Graham, D. (2004) Rapid and ultra-sensitive determination of enzyme activities using surface-enhanced resonance Raman scattering. *Nat. Biotechnol.* 22, 113.
- [23] Kneipp, K., Wang, Y., Kneipp, H., Perelman, L.T., Itzkan, I., Dasari, R.R. and Feld, M.S. (1997) Single molecule detection using surface-enhanced Raman scattering. *Phy. rev. Lett.* 78, 1667.
- [24] Haes, A.J. and Van Duyne, R.P. (2002) A nanoscale optical biosensor: Sensitivity and selectivity of an approach based on the localized surface plasmon resonance spectroscopy of triangular silver nanoparticles. *J. Am. Chem.* 124, 10596.

- [25] Smallenburg, F., Filion, L., Marechal, M. and Dijkstra, M. (2012) Vacancy-stabilized crystalline order in hard cubes. *arXiv:1111.3466v2*
- [26] Escobedo, F.A. (2006) Designing Novel Microstructured Materials via Molecular Simulation NSF Award Abstract 0553719
- [27] Blaak, R., Frenkel, D. and Mulder, B.M. (1999) Do cylinders exhibit a cubic phase? *J. Chem. Phy.* 110, 110652-11659.
- [28] Golshtein, E.G. and Tretakov, N.V. (1996) Modified Lagrangians and Monotone Maps in Optimization. *Modified Lagrangians and Monotone Maps in Optimization*, Wiley, New York.
- [29] Steinhardt, P.J., Nelson, D.R. and Rochetti, M. (1983) Bond orientational order in liquids and glasses. *Phy. Rev.* 28, 783-805.
- [30] Lechner, W. and Dellago, C. (2008) Accurate determination of crystal structures based on averaged local bond order parameters. *J. Chem. Phy.* 129, 114707.
- [31] Chakravarty, C., Debenedetti, P.G. and Stillinger, F.H. (2007) Lindemann measures for the solid-liquid phase transition. *J. Chem. Phy.* 126, 204508.

CHAPTER 4
YIELDING AND SHEAR INDUCED MELTING OF 2D MIXED CRYSTALS
OF SPHERES AND DIMERS

4.1 Abstract

Dislocation cages formed by blocking orientations of dimer particles introduce two opposing effects on the mechanical strength and rheological properties of two-dimensional mixed crystals of monomers and dimers. Upon increasing the dimer concentration, the number of dislocations and vacancies increases weakening the crystal, but also the size of dislocation cages reduces reinforcing the crystal by an effect similar to grain-boundary strengthening. In constant stress simulations, these competing effects lead to a non-monotonic dependence of yield stress on dimer fraction wherein it first drops and then increases. In constant shear simulations, the crystals exhibit a plateau region in the stress vs. strain rate curves right around the yield stress values, confirming a change in dynamical and structural behavior at these points. Solid, hexatic-like, and liquid phases emerge at different shear rates, with the hexatic-like phase (whose onset coincides with the plateau region) resulting from a dynamic balance between the rate of crystal growth (driven by thermodynamics) and the rate of melting (driven by shear). The differences in microstructures of these phases with respect to the spatial distribution and dynamics of dislocations and vacancies provide a detailed picture of the shear-induced melting. The solid and hexatic-like phases also differ with respect to their stress relaxation mechanism with the latter exhibiting a phase lag between the instantaneous stress and microstructural yielding event.

4.2 Introduction

Compared to spherical particles, assemblies and suspensions of particles of anisotropic shapes possess slower dynamics[1],[2] and exhibit widely different mechanical[3] and transport properties[4]. For colloidal crystals the nucleation and relaxation mechanism of defects (such as dislocations and vacancies) critically determines numerous macroscopic phenomena such as plasticity, melting, and work hardening[5]-[7]. Hence exploring the relationships between microscopic events (like defect nucleation and relaxation mechanisms) and the relevant macroscopic mechanical properties of colloidal crystals having varying amounts of anisotropic particles will translate into a deeper fundamental understanding of the effect of particle anisotropy on mechanical properties and rheology. Recently conducted experiments and simulations uncovered a novel glass-like dislocation relaxation behavior in crystalline assemblies of dimer particles[8],[9] that contrasts the free dislocation glide mechanism in spherical particle crystals. It was observed that certain orientations of dimer particles block the dislocation glide thus forming dislocation cages. Hence, dislocations undergo a two-stage relaxation mechanism, with an exponentially fast local relaxation and a logarithmically slow cage-hopping mechanism. Further studies of mixed crystals of dimers and spherical particles[10] indicate that vacancies play a crucial role in uncaging the dislocations via climb events and that vacancy diffusion decreases drastically with increasing dimer concentration. It was also established that dislocation cage sizes decrease monotonically with dimer concentration. Altogether, these results suggest the possibility of a glass transition composition at which the dislocation dynamics will change from being unrestricted to glass-like. In this study, we explore the effect of these microscopic

relaxation differences on macroscopic behavior by calculating the yield stresses and exploring the steady shear induced melting of mixed crystal of various compositions. Further, since these mixed crystals possess a single anisotropic element in the form of doubly lobed particles, they provide a convenient testbed to elucidate the effect of shape anisotropy on mechanical and transport properties of their ordered assemblies. We probed structural differences in these mixed crystals at various compositions and under different shear strain conditions, by calculating average number of dislocations/vacancies, static structure factors, six-fold bond orientational order parameters[11], and pair correlation functions. We unveiled dynamical differences using advanced visualization tools which, together with the structural analysis, allowed us to establish correlations between microscopic and macroscopic stress relaxation behavior and characterize the shear induced melting behavior of these mixed crystals. While studies for exploring shear induced melting behavior of spherical particles in 2D[12],[13] and 3D[14],[15] have been reported, to the best of our knowledge this is the first effort to explore shear induced melting behavior of 2D assemblies of anisotropic particles.

4.3 Model and Simulation Methods

The spherical particles and the lobes of dimer particles interact with each other via Weeks-Chandler- Andersen potential[16] given by:

$$\begin{aligned}
U(r) &= 4\epsilon \left(\left(\frac{\sigma}{r} \right)^{12} - \left(\frac{\sigma}{r} \right)^6 \right) + \epsilon \quad \text{for} & r < r_m \\
&= 0 & r > r_m
\end{aligned} \tag{4.1}$$

where r is the interparticle distance and ϵ and σ are the units for energy and length respectively (both set to 1), $r_m = 2^{1/6}\sigma$ is the cut-off distance for the potential. Further, for dimer particles the two connected lobes are maintained at a constant separation of 1.07σ (to approximately match the experimental system in ref. 8-10) by using additional holonomic constraints[17]. The equivalent surface area fractions for spherical particles and dimer particles are estimated using additional coexistence simulations, where the pure dimer and monomer crystals are in mechanical and thermal equilibrium at different osmotic pressure[9]. Out of these different conditions, an area fraction of 0.808 for dimers and 0.729 for spheres is used for this study, as at these values both pure crystals are sufficiently above their melting densities. The reduced temperature of all non-equilibrium NvT simulations is maintained at T^* ($=kT/\epsilon$) value of 0.1 to better approximate hard core interactions.

For all simulations $N=10000$ spherical lobes were used to prepare the initial configuration for crystals of each composition (hence mixtures with 0 to 5000 dimer particles and 0 to 10000 spherical particles were simulated). The starting configurations for the pure dimer crystals are various conformations of a degenerate crystal lattice[18], in which both lobes of the particles are regularly positioned such that they occupy triangular lattice sites while the orientations of the particles are completely random, i.e. equally distributed along the three possible lattice directions. The crystals for mixtures of spherical and dimer particles are prepared by removing randomly selected bonds from an appropriate

number of dimers, hence changing dimer lobes into spherical particles. For each composition, ten such initial random configurations were prepared for subsequent repeated runs. The area fractions for these mixtures are further adjusted so that they satisfy the lever rule (assuming ideal mixing of the two species) with pure system densities being set to $\rho_{dimer}=0.808$ and $\rho_{sphere}=0.729$.

The yield stress of these systems is estimated using a novel approach that is very similar to the widely used experimental technique of creep test[19]. In this method crystals are simulated in a constant stress ensemble using the technique described in ref. 20 along with a recently developed configurational thermostat for atomic and molecular systems[22],[23]. The configurational thermostat is preferred over the profile-biased and other dissipative thermostats as it preserves flow heterogeneities and hence doesn't introduce artifacts in mechanical properties and shear induced melting behavior of these crystals. The crystals are subjected to increasing values of constant applied stresses and the instantaneous value of the shear rate ($\dot{\gamma}$) is monitored. As shown in the inset of Fig. 4.1a, the $\dot{\gamma}$ values keep fluctuating around zero up to a certain value of applied stress, above which a transition occurs to a steady non-zero value of $\dot{\gamma}$. The minimum stress value at which this transition occurs is hence defined as the yield stress of that particular configuration. Around 8-10 simulations are started at broadly distributed stress values around the best guess value of yield stress to obtain an envelope for the yielding point. Thereafter, 4-5 new simulations spanning this envelope are carried out with finely separated intermediate stress values to better pinpoint the yield point. On average, 20-25 simulations are needed for each initial configuration of a crystal. It is observed that the yield stress value depends strongly on the topological order of dimer particles in the lattice, hence we repeated each yield stress calculation for 10 different initial configurations,

obtaining a better average value and approximate error bars for each composition.

For exploring the steady shear rheology and shear induced melting behavior, we carried out constant shear simulations using the SLLOD equations of motion with atomic (for monomers) and molecular (for dimers) configurational thermostat. The equations were integrated using a fourth order Runge-Kutta scheme with a time step of 0.01. The same SLLOD equations of motion were also used to perform the yield stress simulations (discussed above) along with an additional feedback control equation for shear rate[20], which maintains constant stress in the simulation. The complete set of equation obtained by modifying the equation 4 in ref. 13 is given by:

$$\begin{aligned}
 \dot{r}_i &= \frac{P_i}{m} + \dot{\gamma} y_i e_x + \eta F_i \\
 \dot{p}_i &= F_i - \dot{\gamma} p_{y_i} e_x \\
 \dot{\gamma} &= \frac{1}{\tau^2} \left(1 - \frac{P_{xy}(t)}{S_{xy}} \right) \\
 \dot{\eta} &= \frac{1}{Q_\eta} \left(\sum_{i=1}^N \left(\frac{\partial U}{\partial r_i} \right)^2 - k_b T \sum_{i=1}^N \frac{\partial^2 U}{\partial r_i^2} \right)
 \end{aligned} \tag{4.2}$$

We performed constant shear simulations at multiple shear rates for exploring different dynamic regimes for varying compositions of mixed crystals. Relaxation is performed using 10^7 timesteps and the averages for stress values and other structural properties (using uniformly spaced configurations) were calculated over a production cycle of additional 10^7 steps.

4.4 Results

The average yield stress values (with error bars) for 15 different dimer compositions (defined as number of dimer lobes/total number of lobes and ranging from 0 to 1) are plotted in Fig. 4.1a (error bars and averages are estimated by repeating calculations over 10 random configurations for each composition). It is observed that the yield stress values decrease with dimer fraction for low concentrations; followed by a monotonic increase for higher concentrations, with a minimum yield stress of 1.74 around a dimer fraction of 0.08. This non-monotonic behavior of yield stress indicates that dimer particles impart two competing actions affecting the mechanical strength. First, the dimers disturb the lattice structure via entropic penalties associated with their rearrangement and the mismatch with vibration modes of the spherical particles, causing more dislocation and vacancy nucleation events in mixed crystals. Moreover, the caging of dislocations and the reduced diffusion of vacancies[9, 10] preclude their fast annihilation. Hence, the number of both dislocations and vacancies show an increasing trend with dimer fraction, as plotted in Fig. 4.2 for a low constant shear rate of 0.005 for different mixed crystal compositions (averages obtained from 1000 configurations).

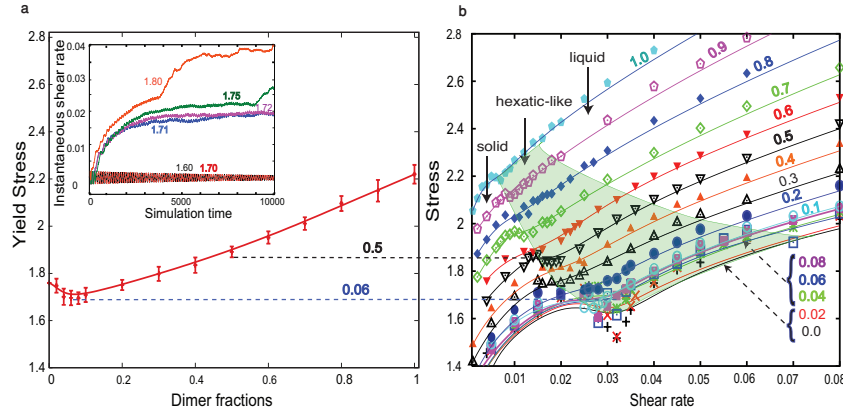


Figure 4.1: a) Average yield stress values (with error bars) for different dimer compositions of the mixed crystals. The inset shows the instantaneous shear rate values for simulations at different constant stresses in the system with dimer fraction = 0.08. The minimum stress value which leads to a non-zero average shear rate is marked as the yield stress of the crystal (1.71 in the inset). b) Stress vs. strain rate for different dimer composition mixed crystals. The agreement between the yield stress values and the plateau of each stress-strain rate curve obtained from independent simulations is shown for two different compositions (horizontal dashed lines across frames 'a' and 'b').

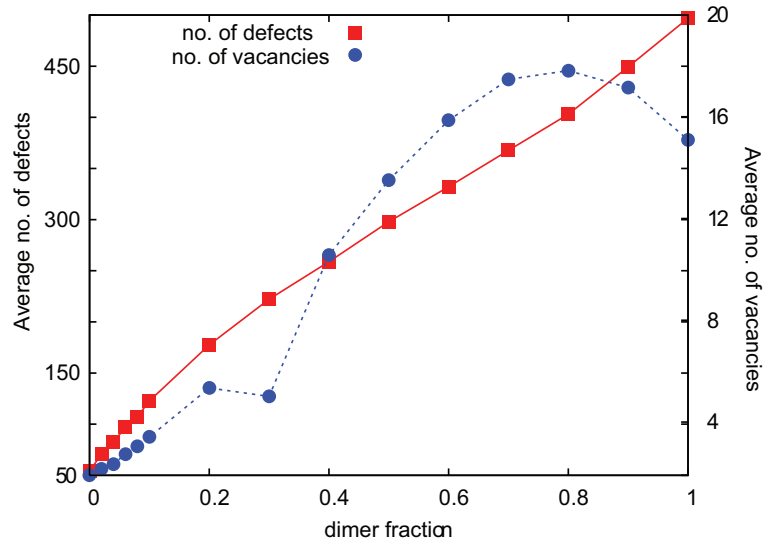


Figure 4.2: The average number of dislocation/disclination sites and vacancies in the sheared crystals at a constant shear rate of 0.005 for different dimer compositions. The average was obtained from 1000 independent configurations for each composition.

Secondly, a competing force imparted by dimers is similar to the Hall-Petch or grain boundary strengthening affect observed in metals[24]. Numerical simulations of mixed crystals revealed a continuous reduction in dislocation cage sizes with increase in dimer fractions[9]. These dislocation cages restrict dislocation glide and hence act as grain boundaries for these colloidal assemblies. The caged dislocations create a repulsive stress field that facilitates the yielding of the crystal. Since this repulsive stress component increases with number of dislocations that pile-up at the grain boundaries[25], reduced grain sizes or cage sizes (as in our system) lowers the number of piled-up dislocations per grain and in turn reduce the net repulsive stress field. Hence, smaller cage sizes with increasing dimer fractions result in larger yield stress. The non-monotonic trend in Fig. 4.1a shows the net result of these two competing effects; the monotonic behavior after the minimum at the dimer fraction of 0.08 indicates that the grain boundary strengthening effect overtakes the weakening effect described first. Constant shear simulations performed at various shear rates for each composition of the mixed crystals indicate the presence of three distinct regimes with respect to their structural and dynamical behavior. The average stress values obtained by averaging over long production cycles are plotted against strain rate for different compositions in Fig. 4.1b. The stress values show a plateau region over a range of shear rates and a monotonic increase thereafter, with a nearly linear dependence after a certain point. Analysis of the structure and dynamics of systems under shear rates belonging to these distinct regimes suggest the existence of solid, hexatic-like, and liquid phases. While marking the exact boundaries of these transitions is highly non-trivial due to dynamic ordering-disordering of the crystal at various time instants, we estimated these phase envelopes (as marked in Fig. 4.1b) by calculating for each shear rate value the

decay behavior of the six-fold bond orientational correlation function $g_6(r) = \langle \psi_6(r) \psi_6^*(0) \rangle$, and the variance $\sigma_{|\psi_6|}^2$ of the global six-fold bond orientational order parameter $\psi_6 = 1/N \sum_{i=1}^N (1/N_i) \sum_{k=1}^{N_i} \exp(6i\theta_{ik})$, where, N is the number of particles, N_i the number of neighbors of particle i and θ_{ik} the bond angle between particle i and k with respect to an arbitrary axis (both evaluated over 1000 regularly spaced configurations). The resulting plots, shown in Figs. 4.3a and 4.3b, help mark out the boundaries for the hexatic-like region and provide important clues of the structural behavior of the system under these particular strain rates. As can be seen in Fig. 4.3a, the $\sigma_{|\psi_6|}^2$ values for various compositions show an extended peak over a certain range of strain rates, indicating a substantial increase in the frequency of reordering of the crystal structure. The $g_6(r)$ curves at different strain rates for a mixed crystal with a dimer fraction of 0.7 are shown in Fig. 4.3b. These plots indicate a power law decay behavior (quasi-long ranged bond orientational order) for the same intermediate shear-rate regime that contrasts with the constant non-decaying behavior (associated with solid-like structures) and exponential decay behavior (associated with liquid-like structures) for shear rates below and above this particular regime. While the power law decay has been typically associated with the existence of a hexatic phase in 2D melting simulations and experiments[26], we observed large fluctuations in the structural and dynamical characteristics for our putative hexatic-like phase that precludes its clear characterization.

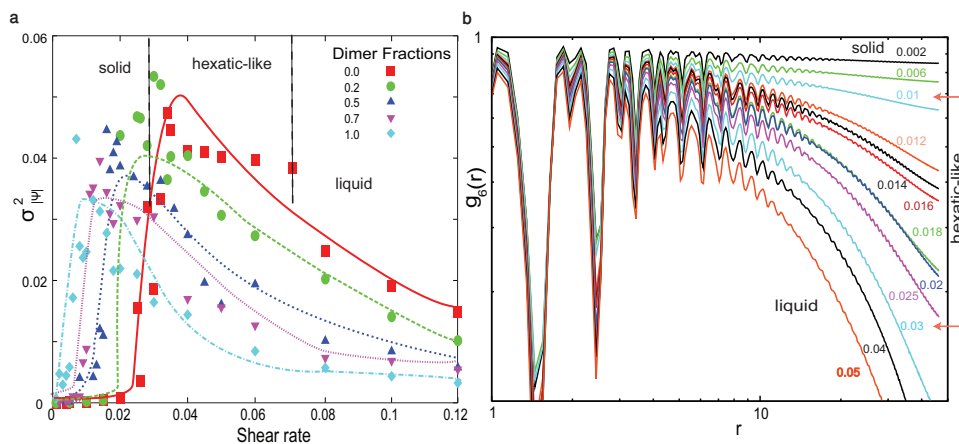


Figure 4.3: a) Variance of the global bond-orientational ψ_6 order parameters obtained from 1000 configurations against shear rate for 5 different mixed crystal compositions (lines are drawn to guide the eye). b) The bond-orientational pair correlation functions $g_6(r)$ for different shear rates for a mixed crystal with dimer fraction of 0.7. The plots also mark the different shear rate regimes for solid, hexatic-like, and liquid phases (which exhibit qualitative differences in variance values and decay behavior of $g_6(r)$).

We used detailed simulation movies, ψ_6 color maps[26] and static structure factors to gain further insights into the structural and dynamical differences among the three different phases. Simulation snapshots obtained over regular intervals of 1 time unit (10^3 time steps) were combined into short movies that are provided as supplementary information files S1-S6. The dynamical characteristics of the sheared crystals were also captured by plotting the ψ_6 color maps for independent configurations obtained over fixed intervals in the production runs, while average structural characteristics were monitored using static structure factor patterns. The ψ_6 color maps are a color-coded representation of the local bond orientation vector $\psi_{6,i} = 1/N_i \sum_{k=1}^N \exp(6i\theta_{ik})$, of each particle lobe i and hence clearly illustrate the spatial distribution of various grains and grain boundaries resulting from the shearing motion of the crystals. The plots on the left of Fig. 4.4 show the ψ_6 local orientations for each particle using the specified coloring scheme; each color map shows the spatial rearrangement and structure of the configurations for each phase at regular time interval of 1000 time units (10^6 time steps) of the mixed crystal with a dimer fraction of 0.7, which is solid at $\dot{\gamma} = 0.002$ (Fig. 4.4a), hexatic-like at $\dot{\gamma} = 0.016$ (Fig. 4.4b), and liquid at $\dot{\gamma} = 0.04$ (Fig. 4.4c). The plots on the right of Fig. 4.4 show the static structure factor patterns for the same shear rates, obtained using 200×200 ($=4 \times 10^6$) wave vectors.

The three phases show significant qualitative differences with respect to the spatial distribution and relaxation of dislocation pairs and vacancies. The solid phase, stable at the low shear rate of ≈ 0.002 , undergoes slow continuous rearrangement as a single crystal grain with the dislocation pairs zipping across the monomer particle region while being restricted by the blocking dimers (as shown in movies S1 and S4). For high dimer fractions (movie S4) the strain

relaxation occurs over long time scales by a few vacancy mediated long-range dislocation-hopping events. It is also clearly seen that the number of dislocations and vacancies increase significantly as the dimer fraction goes from 0.02 (movies S1, S2, and S3) to 0.7 (movies S4, S5 and S6) at all shear rates. For the solid phase, the ψ_6 color maps (left frame of Fig. 4.4a show a single color distribution across the whole crystal, with slight spatters representing small local orientation perturbations. The color changes from one end of the spectrum to the other as the crystal rotates over time, while the structure factor pattern (right frame of Fig. 4.4a shows distinct triangular lattice peaks for all representative snapshots.

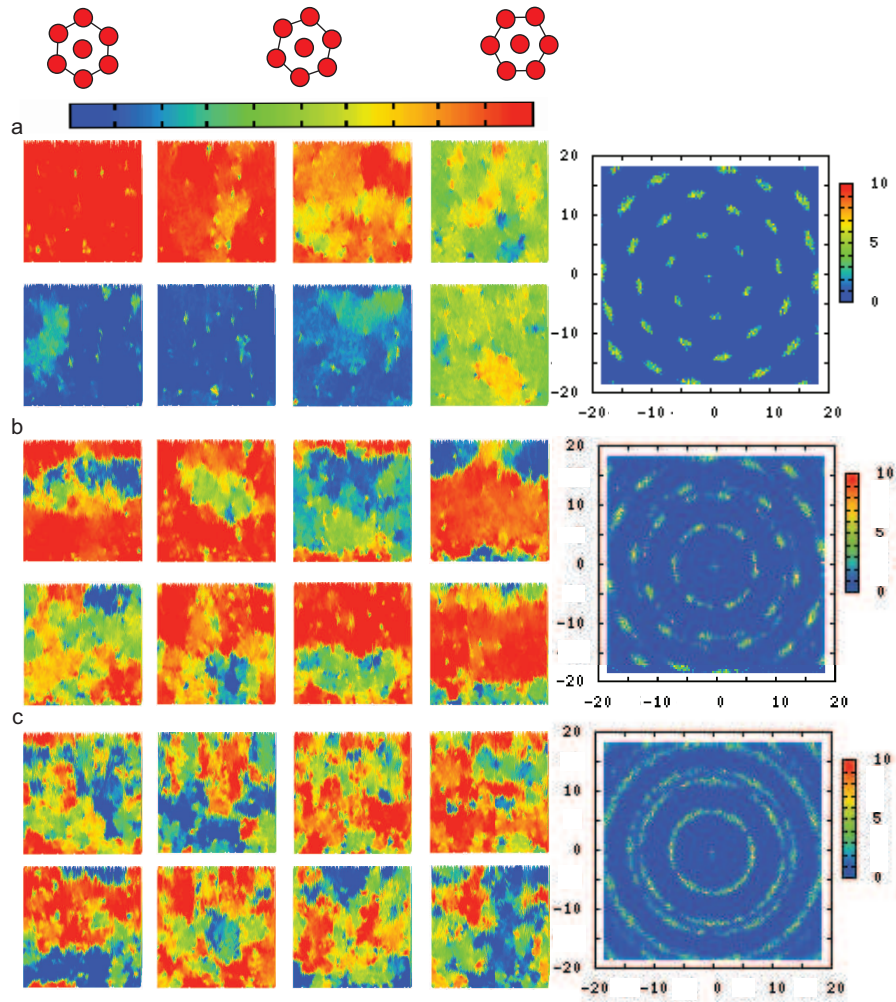


Figure 4.4: ψ_6 color maps (left) and static structure factor plots (right) for the three distinct phases of a mixed crystal with a dimer fraction of 0.7. a) Solid phase at $\dot{\gamma} = 0.002$, b) hexatic-like phase at $\dot{\gamma} = 0.016$, and c) liquid phase at $\dot{\gamma} = 0.04$. The legend on top indicates the color ascribed to the limiting local bond orientational vectors; color maps are obtained for configurations obtained at a regular interval of 103 time units ($= 10^6$ time steps).

For the hexatic-like phase that emerges at shear rates around 0.016 for mixed crystal with dimer fraction 0.7, the simulation movies (S2 and S5) show free dislocation pair unbinding and formation of crystal-wide grain boundaries. The crystal shows yielding behavior around the strain rates corresponding to the plateau region in the stress vs. strain rate curve and exhibit shear banding behavior; i.e., there are two or more grains slipping past each other across the dislocation grain boundary and undergoing shear with different local strain rates. Moreover, the local bond orientational order of these slipping grains remains independent of each other as can be seen in the ψ_6 color maps (left frame of Fig. 4.4b). The representative static structure factor pattern shown in Fig. 4.4b shows dispersion in the peaks, indicative of quasi-long range bond orientational order, characteristic of the hexatic phase[12]. The dislocation grain boundaries keep fluctuating across the crystal and appear dynamically at various positions in the crystal. Moreover, while in equilibrium 2D melting studies (of monomers) the hexatic phase shows free dislocations and nonpercolating grain boundaries which only arise for the liquid phase,[27] in the current shear induced 2D melting we see localized grain boundary formation throughout the entire putative hexatic-like phase. This suggests that the hexatic-like phase observed here could be a stationary coexistence state between the strained crystal and shearing liquid, similar to the one observed in shear induced melting studies of 3D hard spheres[15]. Such a coexistence state would be explained by the dynamic balance between the rate of crystal growth (driven by thermodynamics) and the rate of melting (driven by shear). The grain boundaries separate the system into liquid-like regions exhibiting high shear rates, and solid-like ordered regions undergoing slower shearing motion. Moreover, for mixed crystals with higher dimer content the dislocation grain boundaries are highly jagged with

the grain sizes shrinking (and the number of grains increasing) progressively with shear rate.

The liquid phase observed at shear-rates around 0.04 for the mixed crystal with dimer fraction 0.7 shows a homogeneous shearing behavior with no long-range structural order (movies S3 and S6). The dislocations and vacancies move much more freely through the whole system and have a uniform spatial distribution across configurations. As observed in the left frame of Fig. 4.4c, the ψ_6 color maps for the local bond orientational vectors show much more heterogeneity; locally independent domains can be detected by the widely different colors which indicate uncorrelated or exponentially decaying bond orientational order. The structure factor patterns in the right frame of Fig. 4.4c show uniform rings, further corroborating the absence of any long-range order in the system. For higher dimer fractions, as discussed above and observed in Fig. 4.4c, the crystal is divided into many small independent grains (with their boundaries changing at a high frequency) percolating the whole system and resulting in homogeneous shearing motion. Another interesting signature of the change in the dynamical and structural behavior between solid and hexatic-like phases is that the latter exhibits a period phase shift between the transient stress fluctuations and the bond orientational structure of the configurations. Figure 4.5 shows the time evolution of the instantaneous stress values and $\sigma_{|\psi_{6,i}|}^2$ the variance of the magnitude of the per-particle local bond orientational order parameters $|\psi_{6,i}| = |1/N_i \sum_{k=1}^{N_i} \exp(6i\theta_{ik})|$, for configurations of a mixed crystal with 0.5 dimer fraction. The plots in left frame are for the solid phase at a strain rate of 0.004 and show a close synchronization of the stress values and $\sigma_{|\psi_{6,i}|}^2$. The ψ_6 color maps for configurations at the maximum and minimum stress values indicate that the bond orientation vectors are pointed along the shear direction

for minimum stress while are rotated by $\pi/6$ with respect to the shear direction for the maximum stress value. Moreover, the amount of fluctuations in the local orientations oscillates in phase with the stress values and show maxima at the stress maxima. This suggests that both the stress values and variance peak at the point where the bond orientation or lattice vectors become maximally misaligned with the shear direction as indicated in Fig. 4.5. In contrast, for the hexatic-like phase the stress maxima occurs when the majority of the particles bond orientation vectors are aligned with the shear direction and hence also have minimal variance $\sigma_{|\psi_{6,i}|}^2$ values (right frame of Fig. 4.5). This phase lag in the magnitude of the stress with respect to the bond orientational order signals the changing balance of dynamic forces between the solid and hexaticlike phases. It is conjectured that the phase lag in the hexatic-like phase arises from the slippage occurring at the grain boundaries which serves to partially decouple the dynamics of stress and structural order relaxation. It should also be noted that the $\sigma_{|\psi_{6,i}|}^2$ values for the hexatic-like phase are an order of magnitude larger than those of the crystal phase.

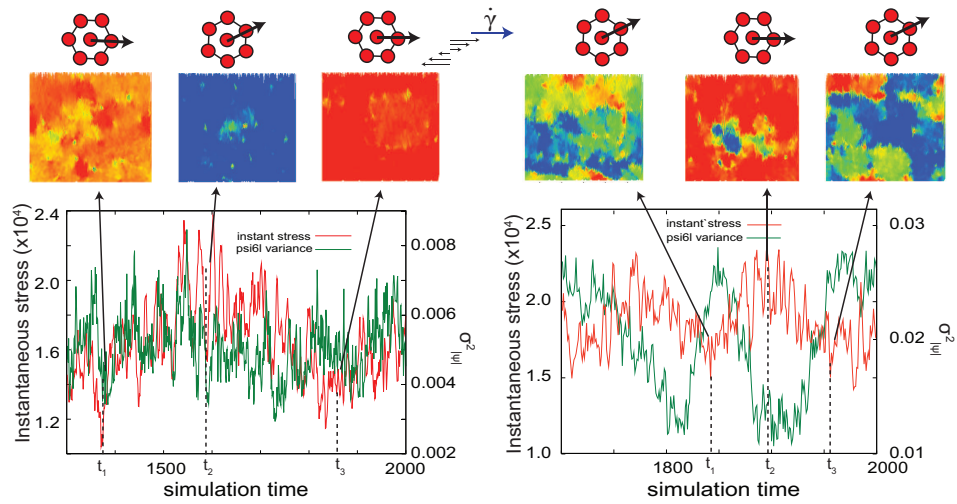


Figure 4.5: Instantaneous stress and variance in the local bond orientational order parameter plotted against time for the solid phase (left) at a shear rate of 0.004 and the hexatic-like phase (right) at a shear rate of 0.02, for a mixed crystal system with dimer fraction of 0.5. The ψ_6 color maps for the configurations at the crest and troughs of the stress profile are shown on top, along with their orientation vectors relative to the strain direction.

4.5 Conclusions

The yielding and shear induced melting behavior of the monomer-dimer mixed crystals show many intriguing differences compared to previous 2D melting and shear induced melting studies for hard spheres[12],[13]. The increase in dimer composition affects the yield stress values of mixed crystals via two competing mechanisms, one that weakens the crystal by introduction of more defects and the other that strengthens the crystal by reduction of cage sizes formed by blocking dimer orientations. Shear induced melting simulations reveal that, as dimer fraction increases, the transitions to hexatic-like phase and liquid phase occur at higher stresses but lower strain rates.. This reflects that higher dimer-content crystals, by virtue of their smaller dislocation cages, can locally yield with smaller but costlier deformations. Moreover, the slipping motion of these crystalline sub-grains (formed by nucleation of dislocation grain boundaries) past each other is highly restricted by any grain-crossing dimer, thus rendering the hexatic-like phase less stable for higher dimer content (i.e., a diminishing presence of the hexatic-like phase). The observation of a phase lag between the stress relaxation and orientational reordering (or microscopic yielding of the local particle crystallite) provides a novel indicator to characterize shear-induced melting behavior. More detailed analysis of the phase lag response in the hexatic-like seems warranted in future studies, since any such correlation between the microstructure and macroscopic responses could help uncover the coupling between mechanical and transport properties of these complex system. While the introduction of dimers into the monomer crystal was anticipated to 'glassify' the system dynamics, it produces a richer and non-trivial behavior under shear. Leading to highly coupled, jagged grain boundaries which exhibit

shear banding at the microscopic level to a novel transitional state that behaves as a non-homogeneous hexatic-like phase at the macroscopic level.

Acknowledgement

This work was supported by the U.S. Department of Energy, Office of Basic Energy Sciences, Division of Materials Sciences and Engineering under award Grant No. ER46517. We gratefully thank C. Liddell Watson, S. Gerbode, and I. Cohen for helpful discussions.

BIBLIOGRAPHY

- [1] R. C. Kramb, R. Zhang, K. S. Schweizer, and C. F. Zukoski (2010) *Phys. Rev. Lett.* 105, 005702.
- [2] R.C. Kramb, and C.F. Zukoski (2011) *J. Rheol.* 55(5), 1069-1084.
- [3] V.V. Ganesh and N. Chawla (2004) *Mat. Sci. and Engg. A* 391, 342-353.
- [4] M.K. Petersen, M.D. Lane, and G.S. Grest (2010) *Phys. Rev. E* 82, 010201.
- [5] G. Taylor (1934) *Proc. R. Soc. A* 145, 362.
- [6] S. Herrera-Velarde, and H.H. von Grnberg (2009) *Soft Matter* 5, 391.
- [7] A. H. Cottrell and B. A. Bilby (1949) *Proc. Phys. Soc. London Sect. A* 62, 49.
- [8] S.J. Gerbode , S.H. Lee, C.M. Liddell, and I. Cohen (2008) *Phys. Rev. Lett.* 101, 058302.
- [9] S. J. Gerbode, U. Agarwal, D. C. Ong, C. M. Liddell, F. A. Escobedo, and I. Cohen (2010) *Phys. Rev. Lett.* 105, 078301.
- [10] S.J. Gerbode, D.C. Ong, C.M. Liddell, and I. Cohen (2010) *Phys. Rev. E* 82, 041404.
- [11] K. Strandburg (1992) *Bond-Orientational Order in Condensed Matter Systems. Springer Verlag, New York.*
- [12] T. Weider, M. A. Glaser, H. J. M. Hanley, and N. A. Clark (1993) *J Phys Rev B* 47, 5662.
- [13] J. Delhommelle (2004) *J Phys Rev B* 69, 144117.
- [14] D. Derks, Y.L. Wu, A. van Blaaderen, and A. Imhof (2009) *Soft Matter* 5, 1060.
- [15] S. Butler and P. Harrowell (2002) *Nature* 415, 1008.
- [16] J.D. Weeks, D. Chandler and H.C. Andersen (1971) *J. Chem. Phys* 54, 5237.

- [17] D. J. Evans and G. P. Morriss (1990) *Statistical Mechanics of Nonequilibrium Liquids*. *Academic, New York*.
- [18] K.W. Wojciechowski (1992) *Phy Rev B* 46, 26.
- [19] Ch. W. Macosko (1994) *Rheology: Principles, Measurements, and Applications*. *Wiley-VCH, New York*.
- [20] L.M. Hood, D.J. Evans, and G.P. Morriss (1987) *Mol. Phys.* 62, 419.
- [21] Haji-Akbari et al. (2009) *Nature* 462:773-776.
- [22] C. Braga and K. P. Travis (2005) *J. Chem. Phys.* 123, 134101.
- [23] K.P. Travis and C. Braga (2008) *J. Chem. Phys.* 128, 014111.
- [24] J. Schitz, and K.W. Jacobsen (2003) *Science* 301, 1357.
- [25] W.D. Callister (2006) *Fundamentals of Materials Science and Engineering*. *Wiley & Sons., New York*.
- [26] E.P. Bernard, and W. Krauth (2011) *Phys. Rev. Lett.* 107, 155704.
- [27] F.L. Somer, Jr., G. S. Canright, T. Kaplan, K. Chen, and M. Mostoller (1997) *Phys. Rev. Lett.* 79, 3431.